

# Searching for Magnetar Binaries Disrupted by Core-Collapse Supernovae

Myles B. Sherman,<sup>1</sup>★ Vikram Ravi,<sup>1</sup> Kareem El-Badry,<sup>1</sup> Kritti Sharma,<sup>1</sup> Stella Koch Ocker,<sup>1,2</sup>  
Nikita Kosogorov,<sup>1</sup> Liam Connor,<sup>1</sup> Jakob T. Faber<sup>1</sup>

<sup>1</sup>*Cahill Center for Astronomy and Astrophysics, MC 249-17 California Institute of Technology, Pasadena CA 91125, USA.*

<sup>2</sup>*The Observatories of the Carnegie Institution of Washington, Pasadena, CA 91101, USA.*

Accepted XXX. Received YYY; in original form ZZZ

## ABSTRACT

Core-collapse Supernovae (CCSNe) are considered to be the primary magnetar formation channel, with 15 magnetars associated with supernova remnants (SNRs). A large fraction of these should occur in massive stellar binaries that are disrupted by the explosion, meaning that  $\sim 45\%$  of magnetars should be nearby high-velocity stars. Here we conduct a multi-wavelength search for unbound stars, magnetar binaries, and SNR shells using public optical (*uvgrizy*-bands), infrared (*J*-, *H*-, *K*-, and *K<sub>s</sub>*-bands), and radio (888 MHz, 1.4 GHz, and 3 GHz) catalogs. We use Monte Carlo analyses of candidates to estimate the probability of association with a given magnetar based on their proximity, distance, proper motion, and magnitude. In addition to recovering a proposed magnetar binary, a proposed unbound binary, and 13 of 15 magnetar SNRs, we identify two new candidate unbound systems: an OB star from the *Gaia* catalog we associate with SGR J1822.3-1606, and an X-ray pulsar we associate with 3XMM J185246.6+003317. Using a Markov-Chain Monte Carlo simulation that assumes all magnetars descend from CCSNe, we constrain the fraction of magnetars with unbound companions to  $5 \lesssim f_u \lesssim 24\%$ , which disagrees with population synthesis results. Alternate formation channels are unlikely to wholly account for the lack of unbound binaries as this would require  $31 \lesssim f_{nc} \lesssim 66\%$  of magnetars to descend from such channels. Our results support a high fraction ( $48 \lesssim f_m \lesssim 86\%$ ) of pre-CCSN mergers, which can amplify fossil magnetic fields to preferentially form magnetars.

**Key words:** stars: magnetars, stars: neutron, binaries: general, stars: massive, ISM: supernova remnants, proper motions

## 1 INTRODUCTION

Magnetars are dense, highly magnetized ( $B \gtrsim 10^{14}$  G) neutron stars which emit pulsed X-ray, gamma ray, or radio emission driven by their magnetic fields (Kaspi & Beloborodov 2017). At the time of submission, there are 24 confirmed magnetars and 7 magnetar candidates identified based on their high-energy X-ray and gamma ray bursts (Richardson et al. 2023; Cline et al. 2000; Lamb et al. 2003; Mereghetti et al. 2012; Torii et al. 1998a; Sakamoto et al. 2011a; Leahy & Tian 2007)<sup>1</sup>. With burst events initially categorized as either Anomalous X-ray Pulsars (AXPs) or Soft Gamma Repeaters (SGRs), magnetars were later identified as the common source of their emission (Gavriil et al. 2002).

Magnetars, like pulsars, are believed to be formed when massive stars undergo Core-collapse Supernovae (CCSNe, formed from Type-II, Type-Ib, and Type-Ic supernovae), with 15 magnetars or candidates having confirmed or potential associations with Supernova Remnants (SNRs) (e.g., Baade & Zwicky 1934; Wheeler 1966; Olausen & Kaspi 2014; Nomoto et al. 1995; Thielemann et al. 1996;

Barker et al. 2023; Truelove & McKee 1999). However, what factors determine whether a CCSN leaves behind a magnetar or a normal neutron star remain unclear (e.g., Giacomazzo & Perna 2013; Giacomazzo et al. 2015; Fuller & Lu 2022; Revnivtsev & Mereghetti 2016; Popov 2020). Furthermore, the CCSN model may be inconsistent with trends in the growing neutron star population. Keane & Kramer (2008) discuss the birth rates of various species of galactic neutron star, including radio and X-ray pulsars, Rotating Radio Transients (RRATs), X-ray Dim Isolated Neutron Stars (XDINs), and magnetars. They find that while the total neutron star birth rate is between  $5 - 10$  century<sup>-1</sup>, the CCSN rate is only  $1.9 \pm 1.1$  century<sup>-1</sup>, suggesting either the CCSN model or birth rate estimate are incomplete. CCSNe are also unlikely to account for the population of young pulsars in Galactic globular clusters (e.g. Kremer et al. 2023).

Magnetar birth rates  $\beta \approx N_{\text{mag}} \mathcal{T}^{-1} \sim 0.3$  century<sup>-1</sup>, are difficult to constrain due to less confident age  $\mathcal{T}$  and population size  $N_{\text{mag}}$  estimates. Most notably, the characteristic spindown age  $\mathcal{T}_{\text{rot}} \propto P(2\dot{P})^{-1} \sim 10$  kyr–10 Myr used for radio pulsars (where  $P$  is the pulse period and  $\dot{P}$  is the spindown rate) does not incorporate the magnetic field decay on  $\sim 10$  kyr timescales thought to drive magnetar emission<sup>2</sup>. Therefore,  $\mathcal{T}_{\text{rot}}$  can significantly overestimate the true

★ E-mail: msherman@caltech.edu

<sup>1</sup> While a number of Gamma Ray Bursts (GRBs) in nearby galaxies have been proposed as magnetar Giant Flares, we focus this work on magnetars and candidates within the Galaxy and Magellanic Clouds (e.g. Trigg et al. 2023; Burns et al. 2021; Svinkin et al. 2021; Mazets et al. 2008; Frederiks et al. 2007; Minaev et al. 2024; Mereghetti et al. 2024).

<sup>2</sup> In this work, we adopt the notation  $\mathcal{T}_{\text{rot}}$  for the characteristic age as opposed to the more widely used  $\tau_c$  to distinguish it from estimates of the angular travel time used in Section 3 and Appendix B4.

age (e.g. Nakano et al. 2015; Ferrario & Wickramasinghe 2008; Pons & Geppert 2007). This overestimation is compounded by frequent ‘glitches’, or abrupt increases in rotation period  $P$ , observed in many magnetars (e.g. Tong & Huang 2020; Younes et al. 2023). However, anti-glitches and glitch recovery in which  $P$  decreases have also been observed, further complicating  $\mathcal{T}_{\text{rot}}$  (e.g. Scholz et al. 2014; Archibald et al. 2013; Olausen & Kaspi 2014). For this reason, magnetic field decay ages  $\mathcal{T}_{\text{decay}} \sim 1 - 100$  kyr derived from X-ray luminosity and magnetic field strength may be preferred, although these are model-dependent, and may not account for rapid initial spindown models (see Appendix D1 in this work, and e.g. Ferrario & Wickramasinghe 2008; Mondal 2021; Arras et al. 2004, for examples of decay models). The ages of associated SNRs  $\mathcal{T}_{\text{SNR}} \sim 1 \text{ kyr} - 100 \text{ kyr}$  are more accurate, but can cover a wide range and are only known for a small fraction of magnetars (Suzuki et al. 2021; Borkowski & Reynolds 2017; Lyman et al. 2022; Gaensler et al. 1999a).

$N_{\text{mag}}$  is also not well constrained. First, it is unclear how magnetar beaming affects the observed population, particularly due to the small sample size (e.g. Keane & Kramer 2008). Furthermore, the detection of a globular cluster (M81) Fast Radio Burst (FRB), thought to originate in a magnetar’s magnetosphere, challenges our assumption that  $N_{\text{mag}}$  scales with star formation (Kirsten et al. 2022; Lu et al. 2022; Petroff et al. 2022). The evolutionary connections among magnetars, pulsars, XDINs, RRATs, and isolated neutron stars are also unclear, leading to potential double-counting errors in the Keane & Kramer (2008) birthrates. Thus, the continued search for and recovery of CCSNe and SNRs will help inform our models and improve age estimates.

SNR radio emission surrounding a magnetar is the most direct indicator of a CCSN progenitor (e.g., Kaspi 1996). Supernova shells are detectable in radio and X-rays expanding from a young (1–10 kyr) magnetar’s birth site at its center; most of the known magnetar-SNR associations were identified by their remnant shell radio emission (e.g. Gelfand & Gaensler 2007; Anderson et al. 2012a). The significant increase in data from radio all-sky surveys will boost the sensitivity considerably. The Rapid ASKAP Continuum Survey (RACS), for example, uses the 36-antenna Australian Square Kilometre Array Pathfinder (ASKAP) telescope to survey the southern sky (declination range  $-80^\circ < \delta < +30^\circ$ ) from 700–1800 MHz (McConnell et al. 2020). The Karl G. Jansky Very Large Array (VLA) Sky Survey (VLASS) and National Radio Astronomy Observatory (NRAO) VLA Sky Survey (NVSS) similarly cover the northern sky above  $\delta > -40^\circ$  at 1.4 and 3 GHz (Gordon et al. 2020, 2021, 2023a; Condon et al. 1998), while the Low Frequency Array (LOFAR) covers lower frequencies near 135 MHz (Shimwell et al. 2022; Shimwell 2016; Condon et al. 1998; Gordon et al. 2020, 2021, 2023a). Identifying supernova shells through radio emission relies on the magnetar being young enough that the shell has not yet dissipated; for expansion rates up to  $\sim 1000 \text{ km s}^{-1}$ , SNRs with ages  $\lesssim 100$  kyr may be detected (e.g., Anderson et al. 2012a; Truelove & McKee 1999; Sedov 2018).

In recent years, the presence (or absence) of binary magnetar systems has become a powerful probe of CCSN formation channels for the broader neutron star population. Chrimes et al. (2022b), Renzo et al. (2019), Kochanek et al. (2019), and Moe & Di Stefano (2017) conducted population synthesis simulations with massive stellar binaries to estimate what fraction of primary stars would remain bound to their secondaries as neutron stars following their CCSN. Moe & Di Stefano (2017) estimate that  $F_0 \sim 84\%$  of massive stars should initially be in binaries, while Kochanek et al. (2019) predicts

that  $f_m \sim 48\%$  of these merge prior to core-collapse<sup>3</sup>; the other  $1 - f_m \sim 52\%$  undergo CCSNe as non-merged binaries. Renzo et al. (2019) suggest a lower merger rate  $f_m \sim 22_{-9}^{+26}\%$ . They also find that  $\sim 14_{-10}^{+22}\%$  of the binaries that do not merge remain bound following the CCSN. Thus only  $f_b \sim 6 - 9\%$  of all neutron stars should have massive binary companions. Chrimes et al. (2022b) affirm these results, obtaining a bound neutron star fraction  $f_b \sim 5\%$ .

Taking a census of neutron star-massive star binaries, 7 pulsars with bound OB star companions have been reported in the Australia Telescope National Facility<sup>4</sup> (ATNF) catalog, while  $\sim 164$  High-Mass X-ray binaries (HMXBs) with neutron star accretors, which accrete from OB star companions, are included in the XRBcat<sup>5</sup> catalog, including the tentatively confirmed SGR-0755-2933 (van der Wateren et al. 2023; Neumann et al. 2023; Fortin et al. 2023; Manchester et al. 2005; Chrimes et al. 2022b; Richardson et al. 2023; Doroshenko et al. 2021). A candidate stellar companion was also proposed for magnetar CXOU J171405.7-381031 using Infrared (IR) Hubble Space Telescope (HST) images, though the IR counterpart’s stellar nature is unconfirmed (Chrimes et al. 2022b). The two proposed binaries out of 31 magnetars are marginally consistent with the  $f_b \sim 5 - 9\%$  expected to be in bound systems, as are the 171 total neutron stars with massive companions out of the total catalog of  $\sim 4200$  neutron stars<sup>6</sup>.

However, one expects a much larger fraction ( $f_u \sim 38 - 56\%$ ) of ‘unbound’ neutron star binaries disrupted by the CCSN, motivating a search for ‘walkaway’ or ‘runaway’ stellar companions (Renzo et al. 2019). Considering a physical scenario, a massive companion ejected at  $\sim 30 \text{ km s}^{-1}$  (Renzo et al. 2019) could travel  $\sim 0.03 \text{ pc}$  over  $\sim 1 \text{ kyr}$ . At a distance of  $5 - 10 \text{ kpc}$ , this should appear only  $\sim 1.2 - 2.5''$  away from its previously bound magnetar. Kochanek et al. (2019) and Kochanek (2018, 2021, 2023) have used the *Gaia* optical catalog to search for both runaway and bound stars nearby 43 SNRs with compact objects, including central pulsars, HMXBs, LMXBs, radio sources, and gamma ray sources. Only the pulsar PSR J0538+2817 was confidently associated with a runaway companion star (Dinçel et al. 2015; Kochanek 2021). Clark et al. (2014) note that the Wolf-Rayet star WR 77F (Wd1-5) may be a runaway unbound companion of magnetar CXOU 164710.2-455216, but the absence of a magnetar proper motion measurement make this difficult to confirm. More general searches for runaway stars with high velocities relative to field stars have also been carried out, but haven’t identified magnetar or pulsar companions (e.g. Carretero-Castrillo et al. 2023). With

<sup>3</sup> Note this fraction includes only mergers where both stars are massive OB stars. For a discussion of CCSNe from mergers of intermediate mass stars, see Zapartas et al. (2017).

<sup>4</sup> <https://www.atnf.csiro.au/research/pulsar/psrcat/>

<sup>5</sup> <http://astro.uni-tuebingen.de/~xrbcat/>; We exclude the 6 HMXBs with confirmed or candidate stellar mass Black Hole accretors.

<sup>6</sup> Our neutron star census includes 3740 pulsars from the ATNF catalog, 164 HMXBs and 271 Low-Mass X-ray binaries (LMXBs) with neutron star accretors from XRBcat,  $\sim 10$  thermally discovered isolated neutron stars including the *Magnificent Seven* ROSAT sample (Pires et al. 2009; Schwöpe et al. 1998; Haberl 2007; Turolla 2009; Tetzlaff et al. 2011; Avakyan et al. 2023), and 31 magnetars and magnetar candidates from the McGill magnetar catalog. We acknowledge this may be incomplete; for example, not all pulsars have sufficient timing solutions to rule out binary companions, and some may be old enough that their companions have undergone supernovae, as well. However, this provides a reasonable estimate of the number of known neutron stars to date.

~ 4200 neutron stars and 31 magnetars, one expects ~ 1600 – 2200 and ~ 11 – 18 unbound companions, respectively<sup>7</sup>.

A comprehensive search of archived data can leverage catalogs like *Gaia*, the Two Micron All Sky Survey (2MASS), and Panoramic Survey Telescope and Rapid Response System (Pan-STARRS or PS1), as well as surveys such as the SkyMapper Southern Survey (SMSS), UKIRT Infrared Deep Sky Survey (UKIDSS) and the Visible and Infrared Survey Telescope for Astronomy (VISTA) Variables in the Vía Láctea (VVV) to find stellar companions (Flewelling et al. 2020; Skrutskie et al. 2006; Chambers et al. 2019; Brown et al. 2021; Lawrence et al. 2007a; Kaiser et al. 2002; Nikzat et al. 2022; Wolf et al. 2018; Onken et al. 2024). For example, Chrimes et al. (2023) predict the ability of *Gaia* Data Release 3 (DR3), as well as future releases from HST, the James Webb Space Telescope (JWST), *Euclid*, and the Nancy Grace Roman Space Telescope (NGRST) to detect unbound stellar objects. They find that while *Gaia* is limited by extinction ( $A_V \lesssim 10$ ), its absolute reference capability and proper motion measurements could increase the number of unbound companion discoveries by ~ 8× when combined with next generation IR telescope data. *Gaia* data have also been used effectively to search for unbound companions of White Dwarfs and neutron stars (Kochanek et al. 2019; El-Badry et al. 2023; Shen et al. 2018).

In this paper, we conduct a search for unbound binary companions of magnetars using the *Gaia* catalog, supplemented by a search for bound companions and CCSN remnants. In Section 2 we describe the magnetar sample used for the search. Section 3 describes the search and trajectory analysis of sources in the *Gaia* archive for unbound magnetar companions and results. In Section 4 we describe the methods and results of the optical and IR search for bound magnetar companions. In Section 5 we summarize the radio image search using the RACS, VLASS, and NVSS catalogs. Section 6 discusses the sensitivity, completeness, and implications of our search. Section 7 concludes with a summary and outlook on next steps for analyzing magnetar formation. Section 8 provides information regarding data availability. Details on the statistical analysis are included in the Appendices.

## 2 MAGNETAR SAMPLE

In Table 1, we present the sample of 24 magnetars listed in the McGill magnetar catalog<sup>8</sup>, as well as 7 unconfirmed magnetar candidates (Olausen & Kaspi 2014). For each we list the Right Ascension ( $\alpha$ ), declination ( $\delta$ ), distance ( $d$ ), and proper motion ( $\mu$ ) from the available literature. We also provide the  $V$ -band dust extinction estimates along each magnetar’s line-of-sight, which we derive using the *Bayestar19*<sup>9</sup> dust map for magnetars above declination  $\delta \gtrsim -30^\circ$  (Green et al. 2015; Schlafly et al. 2015; Green et al. 2018; Green et al. 2019). For magnetars outside this range we use the Predehl & Schmitt (1995) relation between the X-ray column density,  $N_H$ , and  $A_V$  if an  $N_H$  measurement is available. If not, the average photometric extinction from *Gaia* Data Release 3 (DR3) sources within  $1^\circ$  is given (Gaia Collaboration et al. 2016; Collaboration et al. 2022). This will likely underestimate the true extinction, since most *Gaia* sources are in the foreground. 12 magnetars and 3 magnetar candidates have secure or proposed SNR associations.

<sup>7</sup> See Table 4 for definitions of  $f_b$ ,  $f_m$ ,  $f_u$ , and other relevant fractions. These will be discussed in detail in Section 6.2.

<sup>8</sup> <http://www.physics.mcgill.ca/~pulsar/magnetar/main.html>

<sup>9</sup> <https://dustmaps.readthedocs.io/en/latest/modules.html>

## 3 GAIA CATALOG SEARCH FOR UNBOUND COMPANIONS

### 3.1 Gaia Data

The *Gaia* DR3 catalog was queried to search for unbound magnetar companions ejected by the CCSN (Gaia Collaboration et al. 2016; Collaboration et al. 2022). As is highlighted in Chrimes et al. (2023), the *Gaia* catalog is a unique tool given its absolute reference frame which allows for comparison of proper motion data. We build upon previous magnitude-based searches (e.g. Chrimes et al. 2022b) by analyzing the trajectories for each GDR3 source in reference to the magnetars’. Chrimes et al. (2023) note the *Gaia* survey depth  $m_{G,\min} = 20.7$  and proper motion uncertainty ranging from  $9.6 \leq \mu_{\min} \leq 801.6 \mu\text{as yr}^{-1}$  for  $13 \leq m_G \leq 20.7$  limit the survey’s detection of walkaway or runaway stars to those with low extinction ( $A_V \lesssim 10$ ; Lindegren et al. 2021)<sup>10</sup>. Despite this, our combination of magnitude analysis with proper motion data will still make a marked improvement over previous searches, seen for example in El-Badry et al. (2023) and inferred through simulations by Chrimes et al. (2023, Figure 8 row 1).

The *Gaia* query is limited to potential O and B type stars, as we expect many of the companions of magnetars to be massive stars, and removing dim stars significantly reduces contamination by false positives. To do this we impose an upper limit on the absolute  $V$ -band magnitude  $M_V < -2.5 \log_{10}(L_{OB}/L_\odot) + 4.68 = 1.185$ , where we use  $L_{OB} \approx 25L_\odot$ , and color  $G_{BP} - G_{RP} < 2$ . Appendix A contains the Astronomical Data Query Language (ADQL) query used to compile the initial *Gaia* sample.

Following the initial query, extinction corrections and cutoffs were re-applied using the *Bayestar19*<sup>11</sup> dust map (Green et al. 2018; Green et al. 2019) for any *Gaia* sources above declination  $\delta \gtrsim -30^\circ$ . From *Bayestar19* we obtain the  $B - V$  color excess<sup>12</sup>,  $E_{B-V}$ , which is converted to  $V$ -band extinction with  $A_V \approx 3.2E_{B-V}$  and the  $G - V$  excess using the Johnson-Cousins Relations<sup>13</sup>. These are used along with the parallax distance  $d$  from the Bailer-Jones (2023) catalog (see also Bailer-Jones et al. 2021) to obtain the absolute  $G$ - and  $V$ -band magnitudes,  $M_G$  and  $M_V$ . Details on conversions between photometric systems are in Appendix A.

For sources with  $\delta \lesssim -30^\circ$ ,  $M_V$  is computed with Equations A5-A8 using  $A_G$  and  $E_{G_{BP}-G_{RP}}$  reported in *Gaia*, which are derived from  $G_{BP} - G_{RP}$  spectra in the GSP-Aeneas library (Vallenari et al. 2022). However, we proceed cautiously with the GSP extinction estimates, which are known to be unreliable within the Galactic Plane where the effective temperature is overestimated (see Andrae et al. 2022; Fouesneau et al. 2022, Section 3.4, and the *Gaia* DR3 Documentation Section 11.3.3 for details).

Sources were constrained to have parallax  $0.008 < \omega \pm \sigma_\omega < 1.25$  mas based on the distances of the farthest (CXOU J010043.1-721134,  $62.4 \pm 1.6$  kpc) and nearest (Swift J1822.3-16.06,  $1.6 \pm 3$  kpc) magnetars in the McGill catalog, placing an upper limit ~ 125 kpc on the sample. The query was further constrained to Galactic longitudes

<sup>10</sup> <https://www.cosmos.esa.int/web/gaia/science-performance> Section 1

<sup>11</sup> <https://dustmaps.readthedocs.io/en/latest/modules.html>

<sup>12</sup> Note that *Bayestar19* reports reddening in arbitrary units and is converted to  $E_{B-V}$  by multiplying by 0.995 as described at <http://argonaut.skymaps.info/usage> (Schlafly & Finkbeiner 2011). We proceed assuming this factor is approximately 1, which is accurate to the first decimal place.

<sup>13</sup> See the *Gaia* DR3 Documentation at <https://gea.esac.esa.int/archive/documentation/GDR3/> Section 5.5.1 Table 5.9 for details.

**Table 1.** Magnetars and Magnetar Candidates from the McGill Catalog

Magnetar	$\alpha$	$\sigma_\alpha$ (")	$\delta$	$\sigma_\delta$ (")	Distance (kpc)	$\mu_\alpha \cos(\delta)$ (mas yr <sup>-1</sup> )	$\mu_\delta$ (mas yr <sup>-1</sup> )	$A_V$	Refs.
CXOU J010(043.1-721134)	01 <sup>h</sup> 00 <sup>m</sup> 43 <sup>s</sup> .14	0.60	-72° 11' 33" 80	0.60	62.4 ± 1.6	–	–	0.35 <sup>+0.11</sup> <sub>-0.09</sub> <sup>‡</sup>	1,2
4U 0142(+61)	01 <sup>h</sup> 46 <sup>m</sup> 22 <sup>s</sup> .407	0.50	+61° 45' 03" 19	0.50	3.6 ± 0.4	-4.1 ± 1.0	1.9 ± 1	3.81 <sup>+0.51</sup> <sub>-0.16</sub>	3,4,5
SGR 0418(+5729)	04 <sup>h</sup> 18 <sup>m</sup> 33 <sup>s</sup> .867	0.35	+57° 32' 22" 91	0.35	~ 2	–	–	1.60	6
<b>SGR 0501(+4516)*</b>	05 <sup>h</sup> 01 <sup>m</sup> 08 <sup>s</sup> .00	0.11	+45° 16' 31" 00	0.11	2.0 ± 0.3	–	–	2.82 <sup>+0.10</sup> <sub>-0.42</sub>	7,8,9,73
<b>SGR 0526(-66)*</b>	05 <sup>h</sup> 26 <sup>m</sup> 00 <sup>s</sup> .89	0.60	-66° 04' 36" 30	0.60	53.6 ± 1.2	–	–	3.37 <sup>+0.32</sup> <sub>-0.33</sub> <sup>‡</sup>	1,10,11
1E 1048.1(-5937)	10 <sup>h</sup> 50 <sup>m</sup> 07 <sup>s</sup> .14	0.60	-59° 53' 21" 40	0.60	9.0 ± 1.7	–	–	5.42 ± 0.06 <sup>‡</sup>	3,12,13,76,77,78,79
<b>1E 1547.0(-5408)</b>	15 <sup>h</sup> 50 <sup>m</sup> 54 <sup>s</sup> .12	2.30	-54° 18' 24" 11	7.20	3.91 ± 0.07	4.8 ± 0.5	-7.9 ± 0.3	17.88 ± 1.12 <sup>‡</sup>	14,15,16
<b>PSR J1622(-4950)</b>	16 <sup>h</sup> 22 <sup>m</sup> 44 <sup>s</sup> .89	0.80	-49° 50' 52" 70	0.80	9.00 ± 1.35	–	–	30.17 <sup>+8.94</sup> <sub>-7.82</sub> <sup>‡</sup>	17,18
<b>SGR 1627(-41)</b>	16 <sup>h</sup> 35 <sup>m</sup> 51 <sup>s</sup> .84	0.60	-47° 35' 23" 91	0.60	11.0 ± 0.3	–	–	55.87 ± 11.17 <sup>‡</sup>	19,20
CXOU J1647(10.2-455216)	16 <sup>h</sup> 47 <sup>m</sup> 10 <sup>s</sup> .20	0.30	-45° 52' 16" 90	0.30	3.9 ± 0.7	–	–	13.35 ± 0.28 <sup>‡</sup>	21,22
1RXS J1708(49.0-400910)	17 <sup>h</sup> 08 <sup>m</sup> 46 <sup>s</sup> .87	0.80	-40° 08' 52" 44	0.80	3.8 ± 0.5	–	–	7.60 ± 0.22 <sup>‡</sup>	3,23
<b>CXOU J1714(05.7-381031)</b>	17 <sup>h</sup> 28 <sup>m</sup> 27 <sup>s</sup> .49	0.60	-38° 10' 30" 90	0.60	9.8 ± 1.5	–	–	22.07 <sup>+0.84</sup> <sub>-0.78</sub> <sup>‡</sup>	24,25,26,69
<b>SGR J1745(-2900)*</b>	17 <sup>h</sup> 45 <sup>m</sup> 40 <sup>s</sup> .16	0.02	-29° 00' 29" 82	0.09	8.3 ± 0.3	2.44 ± 0.33	5.89 ± 0.11	3.01	27,28,29,30,74,75
SGR 1806(-20)	18 <sup>h</sup> 08 <sup>m</sup> 39 <sup>s</sup> .34	0.04	-20° 24' 39" 85	0.04	8.7 <sup>+1.8</sup> <sub>-1.5</sub>	-4.5 ± 1.4	-6.9 ± 2.0	6.66 ± 0.06	31,32,33
XTE J1810(-197)	18 <sup>h</sup> 09 <sup>m</sup> 51 <sup>s</sup> .07	0.1	-19° 43' 51" 93	0.1	3.5 <sup>+0.5</sup> <sub>-0.4</sub>	-6.60 ± 0.06	-11.72 ± 1.03	3.76 ± 0.03	34,35,70
Swift 1818(0-1607)	18 <sup>h</sup> 18 <sup>m</sup> 03 <sup>s</sup> .70	2.70	-16° 07' 31" 80	2.70	~ 4.8	-3.54 ± 0.05	-7.65 ± 0.09	~ 3.78	36,37,38
Swift J1822(3-1606)	18 <sup>h</sup> 22 <sup>m</sup> 18 <sup>s</sup> .00	1.80	-16° 04' 26" 80	1.80	1.6 ± 0.3	–	–	2.02 <sup>+1.47</sup> <sub>-1.09</sub>	39,40
SGR 1833(-0832)	18 <sup>h</sup> 33 <sup>m</sup> 44 <sup>s</sup> .37	0.30	-08° 31' 07" 50	0.30	–	–	–	~ 3.16 <sup>†</sup>	41
<b>Swift J1834(-9-0846)</b>	18 <sup>h</sup> 34 <sup>m</sup> 52 <sup>s</sup> .12	0.60	-08° 45' 56" 02	0.60	4.2 ± 0.3	–	–	4.03 ± 0.06	42,43
<b>1E 1841(-045)</b>	18 <sup>h</sup> 41 <sup>m</sup> 19 <sup>s</sup> .34	0.30	-04° 56' 00" 69	0.30	8.5 ± 1.3	–	–	3.76 ± 0.06	44,45,46,80,81
<b>3XMM J1852(46.6+003317)</b>	18 <sup>h</sup> 52 <sup>m</sup> 46 <sup>s</sup> .67	2.4	+00° 33' 17" 80	2.4	~ 7.1	–	–	~ 6.30	47
SGR 1900(+14)	19 <sup>h</sup> 07 <sup>m</sup> 14 <sup>s</sup> .33	0.15	+09° 19' 20" 1	0.15	12.5 ± 1.7	-2.1 ± 0.4	-0.6 ± 0.5	10.94 <sup>+0.06</sup> <sub>-0.03</sub>	48,49,33
<b>SGR 1935(+2154)</b>	19 <sup>h</sup> 34 <sup>m</sup> 55 <sup>s</sup> .60	0.70	+21° 53' 47" 79	0.70	9.0 ± 2.5	–	–	8.58 <sup>+0.16</sup> <sub>-1.98</sub>	50,51,52,82,83
<b>1E 2259(+586)</b>	23 <sup>h</sup> 01 <sup>m</sup> 08 <sup>s</sup> .30	0.70	+58° 52' 44" 45	0.70	3.2 ± 2.0	-6.4 ± 0.6	-2.3 ± 0.6	2.59 <sup>+0.38</sup> <sub>-1.79</sub>	53,54,55,5,84
<i>SGR 0755(-2933)</i>	07 <sup>h</sup> 55 <sup>m</sup> 42 <sup>s</sup> .48	180	-29° 33' 53" 46	180	3.5 ± 2.0	–	–	1.82 <sup>+0.32</sup> <sub>-1.18</sub>	56,57,58,72
<b>SGR 1801(-23)*</b>	18 <sup>h</sup> 00 <sup>m</sup> 59 <sup>s</sup>	13680	-22° 56' 48" 00	13680	–	–	–	~ 1.95 <sup>†</sup>	59
<i>SGR 1808(-20)</i>	18 <sup>h</sup> 08 <sup>m</sup> 11 <sup>s</sup> .20	414	-20° 38' 49" 00	414	–	–	–	~ 2.82 <sup>†</sup>	60
<i>AX J1818(.8-1559)</i>	18 <sup>h</sup> 18 <sup>m</sup> 51 <sup>s</sup> .38	0.90	-15° 59' 22" 62	0.05	–	–	–	20.11 ± 2.79 <sup>‡</sup>	61
<i>AX J1845(-0258)</i>	18 <sup>h</sup> 44 <sup>m</sup> 54 <sup>s</sup> .70	0.60	-02° 56' 53" 10	0.60	8.5	–	–	~ 5.15	62,63,64
<i>SGR 2013(+34)</i>	20 <sup>h</sup> 13 <sup>m</sup> 56 <sup>s</sup> .90	2.7	+34° 19' 48" 00	2.7	8.5 ± 1.32	–	–	~ 4.38	65,71
<b>PSR J1846(-0258)</b>	18 <sup>h</sup> 46 <sup>m</sup> 24 <sup>s</sup> .94	0.15	-02° 58' 30" 10	0.20	6.0 <sup>+1.5</sup> <sub>-0.9</sub>	–	–	5.00 <sup>+0.13</sup> <sub>-0.06</sub>	66,67,68,85,86

Abbreviated magnetar names are given with full names in parentheses, which are used throughout this work. RA ( $\alpha$ ), declination ( $\delta$ ), and distance are taken from the McGill Magnetar Catalog (Olausen & Kaspi 2014), while proper motions ( $\mu_\alpha \cos(\delta)$  and  $\mu_\delta$ ) were found in the available literature. Italicized entries are unconfirmed magnetar candidates and boldfaced entries have confirmed or proposed supernova remnant associations. Proposed associations are indicated by a \*.  $A_V$  extinction estimates are from the *Bayestar19* map for magnetars with  $\delta \gtrsim -30^\circ$ . Magnetars outside this range have  $A_V$  from the X-ray column density  $N_H$  (indicated by a ‡) using the Predehl & Schmitt (1995) relation:  $A_V \approx (5.59 \times 10^{-22} \text{ cm}^2) N_H$ . If no  $N_H$  measurement is available, we list the median  $A_V$  from *Gaia* GSP photometry for massive sources within  $1^\circ$  (indicated by a †; see Section 3 for details).

Relevant citations referenced in the rightmost column are below: (1) Haschke et al. (2012) (2) Lamb et al. (2002) (3) Durant & van Kerkwijk (2006) (4) Hulleman et al. (2004) (5) Tendulkar et al. (2013) (6) van der Horst et al. (2010) (7) Lin et al. (2011) (8) Göğüş et al. (2010b) (9) Gaensler & Chatterjee (2008) (10) Kulkarni et al. (2003) (11) Klose et al. (2004) (12) Wang & Chakrabarty (2002) (13) Gaensler et al. (2005) (14) Tiengo et al. (2010) (15) Deller et al. (2012) (16) Gelfand & Gaensler (2007) (17) Levin et al. (2010) (18) Anderson et al. (2012a) (19) Corbel et al. (1999) (20) Wachter et al. (2004) (21) Kothes & Dougherty (2008) (22) Muno et al. (2006) (23) Israel et al. (2003) (24) Tian & Leahy (2012) (25) Halpern & Gotthelf (2010a) (26) Halpern & Gotthelf (2010b) (27) Bower et al. (2014) (28) Mori et al. (2013a) (29) Shannon & Johnston (2013) (30) Bower et al. (2015) (31) Bibby et al. (2008) (32) Israel et al. (2005) (33) Tendulkar et al. (2012) (34) Minter et al. (2008) (35) Helfand et al. (2007) (36) Karuppusamy et al. (2020) (37) Stamatikos et al. (2020) (38) Ding et al. (2020) (39) Scholz et al. (2012) (40) Pagani et al. (2011) (41) Göğüş et al. (2010a) (42) Leahy & Tian (2008a) (43) Kargaltsev et al. (2012) (44) Tian & Leahy (2008) (45) Wachter et al. (2004) (46) Vasisht & Gotthelf (1997) (47) Zhou et al. (2014) (48) Davies et al. (2009) (49) Frail et al. (1999) (50) Gaensler (2014) (51) Israel et al. (2016) (52) Zhong et al. (2020) (53) Kothes & Foster (2012) (54) Fahlman & Gregory (1981) (55) Hulleman et al. (2001) (56) Barthelmy et al. (2016) (57) Doroshenko et al. (2021) (58) Richardson et al. (2023) (59) Cline et al. (2000) (60) Lamb et al. (2003) (61) Mereghetti et al. (2012) (62) Torii et al. (1998b) (63) Gaensler et al. (1999b) (64) Tam et al. (2006) (65) Sakamoto et al. (2011b) (66) Leahy & Tian (2007) (67) Gotthelf et al. (2000) (68) Helfand et al. (2003) (69) Blumer et al. (2019) (70) Lin et al. (2012) (71) Roming et al. (2008) (72) Barthelmy et al. (2016) (73) Jing et al. (2023) (74) Ponti et al. (2015) (75) Yalinewich et al. (2017) (76) Cline et al. (1982) (77) Park et al. (2012) (78) Park et al. (2020) (79) Sano et al. (2023) (80) Borkowski & Reynolds (2017) (81) Zhou et al. (2019) (82) Kothes et al. (2018) (83) Zhou et al. (2020) (84) Nakano et al. (2017) (85) Leahy & Tian (2008b) (86) Straal et al. (2023)

$-80^\circ \leq b \leq 20^\circ$  based on magnetar locations. Figure 1 shows the resulting *Gaia* sample of 156572 potential OB star sources.

We use a Monte Carlo simulation to estimate p-values for the *Gaia* search. The criteria for association for a given sampled trajectory are below:

(i) When the magnetar and source are extrapolated back in time over a sampled travel time (between 1 – 10 kyr), their initial angular separation  $\Theta \approx 0^\circ$ .

(ii) The absolute V–band magnitude of the *Gaia* source is consistent with that of an OB (possibly A) star ( $-10 \leq M_V \leq 3$ )<sup>14</sup>.

(iii) The difference in 2D travel time for the magnetar and source to travel from their past intersection point to their present positions is  $\Delta\tau_{2D} \approx 0$ .

<sup>14</sup> While we expect most OB stars to have  $M_V \lesssim 0$ , we use a wider range that also includes A stars to avoid missing dim companions.

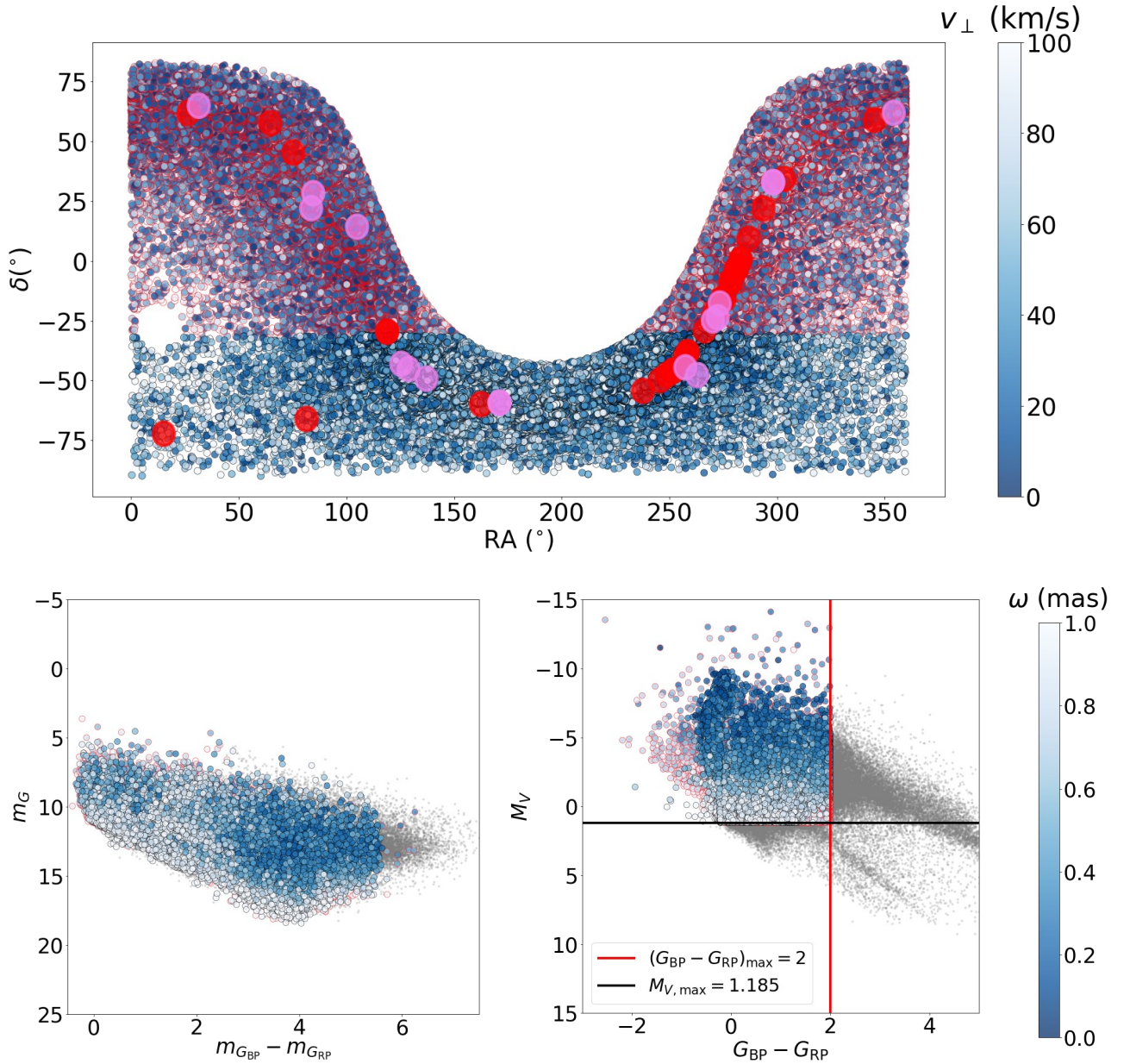


**Figure 1.** (Top) Locations of *Gaia* search sample in Celestial coordinates. The tangential velocity magnitude in  $\text{km s}^{-1}$  is indicated by the colorbar. The *Bayestar19* Dust Map is used for sources at  $\delta > -30^\circ$  (red outline), and the *Gaia* photometric extinction is used for  $\delta < -30^\circ$  (black outline; Vallenari et al. 2022; Green 2019). The  $5^\circ$  radius cones queried around each magnetar are shown in red, and those around each pulsar used for the test sample (see Section 3.2) are shown in violet. Lower transverse velocities are found in the Galactic Plane (GP), meaning that the unbound companions of GP magnetars can be found at smaller angular separations. (Bottom) Color-Magnitude Diagrams for the *Gaia* search sample. The left plot shows the apparent  $G$ -band magnitude  $m_G$  plotted against the apparent  $m_{G_{BP}} - m_{G_{RP}}$  color. The right plot shows absolute  $V$ -band magnitude  $M_V$  for each source against the absolute color  $G_{BP} - G_{RP}$ .  $M_V$  is derived using the Johnson-Cousins relationships in Equations A1-A8 (see Appendix A). Sources with  $\delta > -30^\circ$  are again outlined in black while those with  $\delta \geq -30^\circ$  are outlined in red. The parallax of each source is indicated by the colorbar in milliarcseconds (mas). Sources from the initial query (see Appendix A) which were cut by the magnitude (black) and color (red) limits are shown in grey. GSP-Aeneas extinction estimates may be unreliable in the Galactic plane according to the *Gaia* DR3 Documentation (Section 11.3.3), resulting in a rough color cutoff near  $G_{BP} - G_{RP} \approx -0.5$  (Vallenari et al. 2022; Andrae et al. 2022; Fouesneau et al. 2022).

(iv) The magnetar’s physical travel time  $\bar{\mathcal{T}}_{3D, \text{mag}}$  is consistent with its age  $\mathcal{T}$ .

(v) The source’s parallax distance is consistent with magnetar’s distance, such that  $\Delta d \approx 0$ .

which are used to define p-values  $p_1, p_2, p_3$ , and  $p_4$  respectively (the first two criteria are combined to define  $p_1$ ). Appendix B4 de-

scribes the definition of  $p_1, p_2, p_3$ , and  $p_4$  in more detail, which are combined as shown below:

$$p = 1 - (1 - p_1)(1 - p_2)(1 - p_3)(1 - p_4) \quad (1)$$

We choose this definition (as opposed to e.g. the Fisher statistic,

**Table 2.** Magnetar Age Upper Limits Used for the *Gaia* Search

Magnetar	Age Method	$\mathcal{T}_{\text{decay/rot/SNR}}$	Reference
CXOU J010	Decay	7.7 kyr	This work
4U 0142	Decay	3.8 kyr	This work
SGR 0418	Decay	8.3 Myr	This work
SGR 0501	Decay	59.4 kyr	This work
SGR 0526	Decay	2.9 kyr	This work
1E 1048.1	Decay	8.9 kyr	This work
1E 1547.0	Decay	30.4 kyr	This work
PSR J1622	Decay	44.2 kyr	This work
SGR 1627	Decay	37.0 kyr	This work
CXOU J1647	Decay	2.1 Myr	This work
1RXS J1708	Decay	8.1 kyr	This work
CXOU J1714	SNR	6.2 kyr	Blumer et al. (2019)
SGR J1745	Decay	64.9 kyr	This work
SGR 1806	Decay	1.3 kyr	This work
XTE J1810	Decay	81.1 kyr	This work
Swift J1818	Spindown	0.24 kyr	Esposito et al. (2020)
Swift J1822	Decay	0.2 Myr	This work
SGR 1833	Spindown	34 kyr	Esposito et al. (2011)
Swift J1834	Decay	0.2 Myr	This work
1E 1841	SNR	1.8 kyr	Borkowski & Reynolds (2017)
3XMM J1852	Decay	0.7 Myr	This work
SGR 1900	Decay	4.1 kyr	This work
SGR 1935	SNR	16.0 kyr	Lyman et al. (2022)
1E 2259	Decay	62.0 kyr	This work
<hr/>			
SGR 0755	–	–	–
SGR 1801	–	–	–
SGR 1808	–	–	–
AX J1818	–	–	–
AX J1845	SNR	1.4 kyr	Gaensler et al. (1999a)
SGR 2013	–	–	–
PSR J1846	Spindown	0.73 kyr	Livingstone et al. (2011)

$\mathcal{T}_{\text{decay}}$  is estimated in this work (see Appendix D1 in this work and Ferrario & Wickramasinghe 2008) using the magnetic field  $B_d$  and X-ray luminosity  $L_X$  reported in the McGill Magnetar Catalog (Olausen & Kaspi 2014, and references therein). Spindown ages are those from the McGill catalog, and are approximated as the characteristic age  $\mathcal{T}_{\text{rot}} = P(2\dot{P})^{-1}$ . SNR ages  $\mathcal{T}_{\text{SNR}}$  are used only for magnetars with confident SNR associations. References for the spindown and SNR ages are in the rightmost column.

Lancaster statistic, or a direct average) for its intuitive application to this search, as all four criteria must be met with  $p_i \ll 5\%$  to obtain  $p < 5\%$ . This also makes it straightforward to interpret p-values by tracing back each  $p_i$  to its criterion.

Each magnetar’s age is estimated as the age of its associated SNR  $\mathcal{T}_{\text{SNR}}$  (Suzuki et al. 2021). If no SNR is associated, its X-ray luminosity decay age  $\mathcal{T}_{\text{decay}}$  is used, which adopts the Ferrario & Wickramasinghe (2008) field model and is derived in Appendix D1. For magnetars with no persistent X-ray emission or magnetic field estimates, the characteristic spin-down age  $\mathcal{T}_{\text{rot}}$  is used (Olausen & Kaspi 2014). In Table 2 we provide the derived or reported timescales for each magnetar.

### 3.2 *Gaia* Search Test with Pulsar Supernova Remnants

In order to test the search pipeline, we applied the Monte Carlo simulation to a sample of 15 pulsars with known SNR associations and proper motion measurements compiled from the ATNF catalog (van der Wateren et al. 2023; Andersen et al. 2023; Lyne et al. 2015; Stairs et al. 2001; Dinçel et al. 2015; Kochanek 2021). Within this sample, only PSR J0538+2817 is known to have a runaway companion B0.5V-type star, as discovered by Dinçel et al. (2015) and confirmed by Kochanek (2021). The upper limit on the travel time  $\tau$  is set to 1 Myr given that pulsars tend to be older than magnetars (e.g. Kaspi & Beloborodov 2017). The initial Monte Carlo simulation (criteria 1 and 2) identifies between 2 and 800 poten-

tial candidates with  $p_1 < 5\%$  for each of the 15 pulsars. Following the trajectory analysis, only 1 pulsar, PSR B1951+32 remains with  $p < 5\%$  and a sufficient fraction valid trajectories<sup>15</sup>. The companion of PSR J0538+2817 is not initially recovered. In this section we discuss the likelihood of PSR B1951+32’s candidate companions, and the reasons for PSR J0538+2817’s omission. Figure 2 shows the trajectory plots for both pulsars.

#### 3.2.1 PSR J0538+2817

For PSR J0538+2817, we initially do not recover the runaway companion star, HD 37424, which was identified by Dinçel et al. (2015) and Kochanek (2021). The corresponding *Gaia* source, *Gaia* DR3 3441732292729818752, was assigned a p-value  $p = 16\%$  and therefore was not identified as a candidate. Upon further inspection, we find the high p-value is the result of a high false positive rate; among the simulated sources used to estimate the  $H\theta$  distribution, 32% are found with  $p_1 < 1\%$ <sup>16</sup>. We attribute this to the large association region in  $\{\Theta, M_V\}$  space which extends to nearly  $10^\circ$  (see Figure 2). While pulsars have larger confidence regions in  $\{\Theta, M_V\}$  space than magnetars due to the higher age limit and lower distances, the high proper motions of PSR J0538+2817 and PSR B2334+61 further extend the region, resulting in unusually high false positive rates  $\sim 42\%$  and  $\sim 6\%$ , respectively.

We therefore increase the p-value thresholds for these two sources to match their false positive rates. For PSR B2334+61, no additional sources are identified with the new threshold, whereas HD 37424 and 5 other sources are identified as candidates for PSR J0538+2817 after increasing the threshold. This scenario also justifies our use of the search statistic  $\hat{f} < \hat{f}_c$  to identify candidates initially, as it implicitly accounts for this false-positive rate bias. Our conditional recovery of PSR J0538+2817’s runaway star demonstrates the accuracy and sensitivity of our search method, but indicates we must be wary of false positives and sources along unique sightlines. We address completeness of the magnetar search in detail in Section 6.

#### 3.2.2 PSR B1951+32

One *Gaia* companion candidate is identified for PSR B1951+32 with  $p < 1\%$ , *Gaia* DR3 2035109887486067456 (catalogued as TYC 2673-414-1 Høg et al. 2000a). The parallax distance  $1.13 \pm 0.02$  kpc is only marginally consistent with the pulsar’s  $\sim 3$  kpc distance, which has an uncertainty that is not well defined (Kulkarni et al. 1988). The pulsar’s dispersion measure (DM) and more recent estimates of the associated SNR CTB 80 suggest a closer  $\sim 2$  kpc distance, which would be more consistent with TYC 2673-414-1 (Kramer et al. 2000; Migliazzo et al. 2002; Yao et al. 2017). From the 2MASS counterpart, 2MASS J19544429+3327472, we estimate absolute  $H$ -band magnitude  $M_H \approx -4.5$  and  $J-H$  color  $J-H \approx -0.1$  when placed at the pulsar distance 3 kpc. While these are reasonable, they do fall outside of the expected ranges of IR magnitude and color from Chrimes et al. (2022b)’s simulations. From the valid trajectory samples, TYC 2673-414-1 is required to have velocity

<sup>15</sup> Three other pulsars had candidates with  $p < 5\%$ , but used only one valid trajectory, for which the source and pulsar paths intersect, out of 100 trials, and they are considered false positives.

<sup>16</sup> The minimum p-value is set by the number of trials, which varies for each magnetar depending on what constraints on its position, distance, and proper motion are available. 100 trials were used for PSR B1951+32 and PSR J0538+2817.

$|\vec{v}| \approx 74_{-4}^{+16} \text{ km s}^{-1}$ , which would be consistent with a more rare runaway star if ejected from the pulsar's CCSN (Renzo et al. 2019). While pulsar companions are not the focus of this search, we encourage follow-up of TYC 2673-414-1 as a possible unbound companion of PSR B1951+32.

### 3.3 Gaia Search Results

Through the *Gaia* Monte Carlo search, we identify potential candidates with  $p < 5\%$  for 2 magnetars. In Figure 2, we show the trajectory plots and contour plots of the Monte Carlo samples for these, along with CXOU J164710.2-455216, whose proposed companion WR 77F we recover with  $p = 0.6\%$  (Clark et al. 2014). We rule out one of the two candidates, 3XMM J185246.6+003317, as a false positive based on detailed analysis of its candidates' velocities and distances, which we discuss in Appendix C1. Having not recovered the proposed binaries SGR 0755-2933 and CXOU J171405.7-38131, we find this search method is relatively insensitive to bound stellar companions due to their position within magnetars' error ellipses (Chrimes et al. 2022b; Richardson et al. 2023; Doroshenko et al. 2021). However, it is a useful tool to identify which candidates are likely to be bound companions (see Section 4.3). In the following sections, we focus on the unbound companion candidates for SGR J1822.3-1606 and CXOU J164710.2-455216.

#### 3.3.1 SGR J1822.3-1606

The primary candidate for an unbound system is SGR J1822.3-1606 and *Gaia* DR3 4097832458955594880, which is assigned a p-value  $p < 0.1\%$ . Its distance,  $d = 1.00_{-0.02}^{+0.03} \text{ kpc}$ , is consistent with that of the magnetar,  $1.6 \pm 0.3 \text{ kpc}$ , at the  $2\sigma$  level, and from the IR counterpart, 2MASS 18230515-1600296, we estimate absolute magnitudes  $M_J = -3.9 \pm 0.5$  and  $M_H = -4.6_{-0.4}^{+0.5}$ , and color  $J - H = 0.7 \pm 0.1^{17}$ , which are both reasonable for a low-mass B-type star. SGR J1822.3-1606 does not have a measured proper motion, and our simulation suggests  $\mu_\alpha \cos(\delta) = -29_{-24}^{+15} \text{ mas yr}^{-1}$ ,  $\mu_\delta = -25_{-19}^{+13} \text{ mas yr}^{-1}$  are required for the magnetar to have a valid trajectory<sup>18</sup>. A wide range of magnetar velocities are permitted for this association, with  $|\vec{v}_{\text{mag}}| = 413_{-175}^{+184} \text{ km s}^{-1}$ . Notably, the permitted stellar velocity  $|\vec{v}| = 60_{-5}^{+7} \text{ km s}^{-1}$  would classify this as a rare 'runaway' companion star (Renzo et al. 2019). This is roughly consistent with the source's high transverse velocity,  $\sim 55 \text{ km s}^{-1}$ , making the association achievable without a significant radial component. While it is unlikely that such velocities can be reached from CCSN disruption alone, other mechanisms may contribute to the source's and magnetar's space motion, such as dynamical ejection from an OB association (e.g. Poveda et al. 1967; Tetzlaff et al. 2011). Therefore, we identify this as a promising candidate, and further characterization from follow-up observations would be of great interest.

<sup>17</sup> Uncertainties are estimated from the 16<sup>th</sup> and 84<sup>th</sup> percentiles of the magnitude and color samples, which take into account distance and apparent magnitude errors.

<sup>18</sup> Estimates of the proper motion and velocity are derived from Monte Carlo samples found to produce 'valid' trajectories which are found to intersect through our iterative analysis. Uncertainties are from the 16<sup>th</sup> and 84<sup>th</sup> percentiles of these 'valid' samples.

#### 3.3.2 CXOU J164710.2-455216

Next, we consider the Wolf-Rayet star WR 77F (or Wd1-5), which Clark et al. (2014) suggest as an unbound companion of CXOU 164710.2-455216 based on the position, radial velocity and chemical content of the star. WR 77F is associated with *Gaia* DR3 5940106797374726784 which was not included in the initial *Gaia* query, possibly due to an underestimated *Gaia* extinction from GSP photometry. We add this candidate to the sample and run the simulation with an increased 1000 trials after finding a low fraction of valid trajectories with 100 samples. Given that the candidate is an evolved Wolf-Rayet star rather than a main-sequence OB star, and that magnetar CXOU J164710.2-455216 lies along a high extinction sightline with  $A_V = 13.35 \pm 0.28$ , we omit  $p_1$  from this analysis (which initially was  $p_1 > 99.9\%$ ). With this adjustment, we recover a p-value  $p_{2,3,4} = 0.6\%$ . The magnetar's derived physical travel time  $\mathcal{T}_{3D, \text{mag}} \approx 16.0_{-10.0}^{+25.6} \text{ kyr}$ , is consistent with its decay age  $\mathcal{T}_{\text{decay}} \approx 0.2 \text{ Myr}$  within  $\sim 1\sigma$ . Finally, the valid trajectories require velocities  $|\vec{v}_{\text{mag}}| \approx 390 \pm 170 \text{ km s}^{-1}$  and  $|\vec{v}| \approx 80_{-13}^{+20} \text{ km s}^{-1}$  for CXOU 164710.2-455216 and WR 77F, respectively. The former is consistent with Hobbs et al. (2005) while the latter suggests that WR 77F is a runaway star ( $|\vec{v}| \gtrsim 30 \text{ km s}^{-1}$  Renzo et al. 2019). However, the localization of CXOU J164710.2-455216 and WR 77F to the Westerlund-1 massive star cluster implies that dynamical ejection may have contributed to the large observed velocities, as well. We conclude it is likely that CXOU J164710.2-455216 are WR 77F are an unbound magnetar binary disrupted by the former's CCSN, potentially supplemented by dynamical ejection, supporting the results of Clark et al. (2014).

## 4 OPTICAL AND IR SEARCH FOR BOUND COMPANIONS

In this section, we search for bound OB star-magnetar binaries using optical and near-IR images. As discussed in Section 1, bound companions should have negligible ( $\lesssim 1'$ ) separation from the magnetar in high resolution ( $\sim 0.25'' - 0.4''$ ) images. Chrimes et al. (2022a) conducted a similar search using HST Wide Field Camera 3<sup>19</sup> images with  $\sim 27$  magnitude depth and  $0.1265''$  resolution. They place tight constraints with milliarcsecond precision on  $\sim 15$  magnetar NIR counterpart candidates using  $H$ -band HST data, laying the foundation for the Chrimes et al. (2022b) search.

While Chrimes et al. (2022b) discuss that searching in NIR is more effective than optical due to the  $\sim 7\times$  lower extinction, searching optical data is still beneficial. The massive, un-evolved OB star companions we expect are intrinsically fainter in the NIR than optical wavelengths. The magnitude depth of the PS1 ( $\sim 24$ ) and SkyMapper ( $\sim 18$ ) catalogs therefore makes them powerful resources for this search (Maund et al. 2016; Kaiser 2004; Wolf et al. 2018; Onken et al. 2024). We also note that since the resolution ( $0.4''$ ,  $0.34''$ , and  $3''$ , respectively) and depth ( $\sim 18$ ,  $\sim 15$ , and  $\sim 19.3$ , respectively) of the UKIDSS, VVV, and 2MASS images are far exceeded by HST, any additional data to supplement the breadth of the search is valuable.

<sup>19</sup> See the WFC3 Instrument Handbook for details: <https://hst-docs.stsci.edu/wfc3ihb/chapter-7-ir-imaging-with-wfc3/7-8-ir-sensitivity>

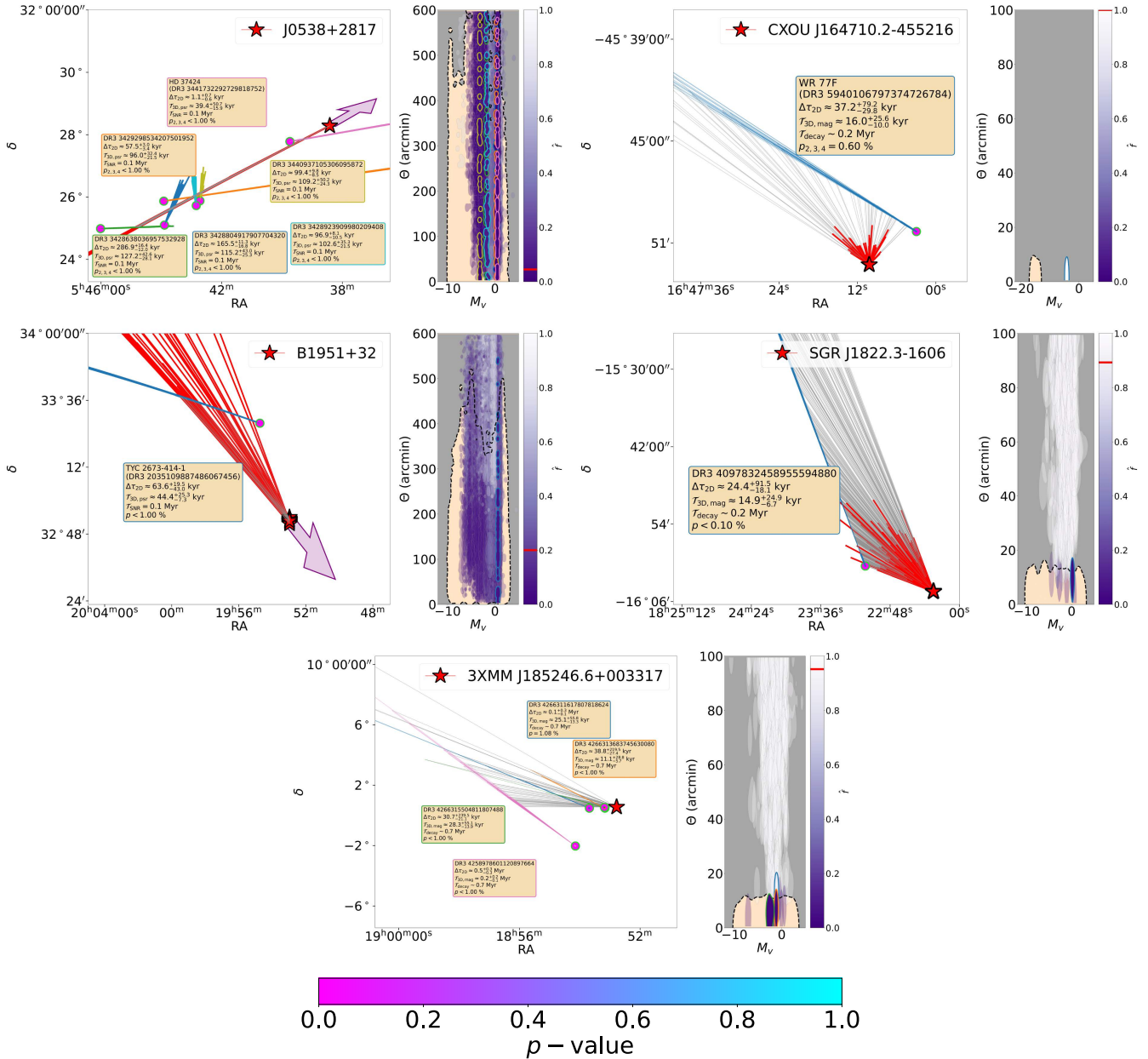


**Figure 2.** (Left) Monte Carlo sampled trajectories for candidate *Gaia* DR3 sources with p-values  $p < 5\%$  possibly associated with 3 magnetars (right, bottom), PSR J0538+2817 (top left), and PSR B1951+32 (middle left). Each figure includes only *Gaia* OB star candidates with association p-value  $p < 5\%$ , including the unbound companion of CXOU J164710.2-455216 proposed by Clark et al. (2014), WR 77F (top right). Present-day magnetar/pulsar and GDR3 source locations are shown as red stars and circular markers, respectively; the latter has colorbar corresponding to the total p-value  $p$ , except for PSR 0538+2817 and CXOU J164710.2-455216, for which we exclude  $p_1$  (see Section 3). Red lines show the initial magnetar/pulsar trajectory samples while thin lines extrapolate the magnetar/pulsar and source trajectories to their past intersection. Note for these initial trajectories extend farther for pulsars (top left, middle left) than for magnetars (right, bottom) since travel time samples were drawn from a uniform distribution up to 1 Myr for pulsars in contrast to 10 kyr for magnetars. If proper motion measurements are available, the proper motion direction is indicated by a purple arrow. Each GDR3 source is shown with its source ID, 2D travel time difference  $\Delta\tau_{2D}$ , the magnetar’s/pulsar’s 3D travel time  $\mathcal{T}_{3D, \text{mag/psr}}$ , an upper limit age estimate  $\mathcal{T}_{\text{SNR/decay/rot}}$ , and the relevant p-value. (Right) Contour plot of Monte Carlo samples in  $\{\Theta - M_V\}$  space. The 95% contour region is in beige, and candidates with search statistic  $\hat{f}$  less than the critical threshold,  $\hat{f}_c$ , have colorbar corresponding to  $\hat{f}$  (see Appendix B4).  $\hat{f}_c$  is indicated by a red horizontal line on each colorbar. We recover the proposed companions of CXOU J164710.2-455216 (WR 77F; upper right) and PSR J0538+2817 (HD 37424; top left) with  $p < 5\%$ . We also identify potential runaway companions of SGR 1822.3-1606 and PSR B1951+32 (middle row) with  $p < 5\%$ . The companions shown for 3XMM J185246.6+003317 (bottom) are most likely false positives as discussed in Appendix C1.



#### 4.1 Pan-STARRS and SkyMapper Data and Optical Search Method

The Pan-STARRS Data Release 2 (PS1 DR2) catalog contains optical images of the northern sky (above  $\delta > -30^\circ$ ) in 5 passbands ( $g$ -,  $r$ -,  $i$ -,  $z$ -, and  $y$ -bands, or ‘grizy’) with  $0.25''$  pixels (Flewelling et al. 2020; Chambers et al. 2019).  $1' \times 1'$  image cutouts were obtained from the PS1 Image Server<sup>20</sup> at the position of each magnetar and candidate. 17 magnetars and all 7 magnetar candidates fall within the PS1 survey range. For the remaining 7 with  $\delta \leq -30^\circ$ , we use images from the SkyMapper Southern Survey Data Release 4 (SkyMapper DR4<sup>21</sup>), which records in  $u$ -,  $v$ -,  $g$ -,  $r$ -,  $i$ -, and  $z$ -bands (‘uvgriz’) with  $0.5''$  pixels (Wolf et al. 2018; Onken et al. 2024). Note the point source detection limit is  $\sim 18.0$  in comparison to  $\sim 21.5$  for PS1.

In addition to image cutouts, the PS1 and SkyMapper point source catalogs were queried to obtain known sources within a  $30''$  search cone of each magnetar. We also include any bright sources identified ‘by-eye’ within the image that do not appear to coincide with catalogued point sources (see Appendix B3.1). We then use the catalogued magnitudes and position of each source to conduct a Monte Carlo simulation. Similarly to the *Gaia* search we define the association p-value using three criteria:

- (i) The PS1 source and magnetar are located at the same RA and declination.
- (ii) If we assume the source absolute magnitude is that of an OB star ( $-10 \lesssim M_V \lesssim 3$ ), the distance is equal to the magnetar’s distance.
- (iii) The difference of the Kron and point source (PSF) magnitude ( $M_{x,\text{Kron}} - M_{x,\text{PSF}}$ ) exceeds the Farrow et al. (2014) point source cutoff for  $x = \text{‘uvgrizy’}$  bands as available (Kron 1980):

$$\Delta M_{\min}(M_{x,\text{Kron}}) = -0.319 + 0.129(M_{x,\text{Kron}} - 21) + 0.007(M_{x,\text{Kron}} - 21)^2 \quad (2)$$

for which we define p-values  $p_1$ ,  $p_2$ , and  $p_3$ , respectively. The three p-values are combined to get the total association p-value:

$$p = 1 - (1 - p_1)(1 - p_2)(1 - p_3) \quad (3)$$

An explicit derivation of  $p_1$ ,  $p_2$ , and  $p_3$  is provided in Appendix B1.

The method above was applied only for magnetars with errors defined for the RA, declination and distance, and only for point sources with at least  $g$ - and  $r$ - band PSF and Kron magnitudes<sup>22</sup>, and errors defined for RA and declination. Note that our evaluation of  $p_2$  contrasts with the Chrimes et al. (2022b) search, which uses the magnetar distance to estimate extinction values for nearby candidate stars. However, magnetar distances are not well-constrained, with errors of order  $\sim \text{kpc}$ . In this work, we invert this process to obtain a distance estimate whose uncertainty is driven by the expected absolute magnitude range. Through this, we avoid making assumptions about the source distance beyond the requirement that it be an OB star.

<sup>20</sup> <https://ps1images.stsci.edu/ps1image.html>

<sup>21</sup> <https://skymapper.anu.edu.au/>, [doi.org/10.25914/5M47-S621](https://doi.org/10.25914/5M47-S621)

<sup>22</sup> This unfortunately means that p-values are not estimated for ‘by-eye’ sources in the optical and IR searches. However, most lie at a large angular separation relative to the magnetars’  $\sim 1''$  position errors making them unlikely candidates.

#### 4.2 UKIDSS, VVV, and 2MASS Data and IR Search Method

Infrared images were obtained from the UKIDSS survey catalog, which is a superset of the Large Area Survey (LAS), Galactic Plane Survey (GPS), Galactic Clusters Survey (GCS), Deep Extragalactic Survey (DES), and Ultra Deep Survey (UDS) catalogs (Dye et al. 2006). Collectively, this covers the declination range from  $-60^\circ < \delta < +40^\circ$ , including sightlines for 12 magnetars and 6 magnetar candidates from this sample. We obtained  $1' \times 1'$  image cutouts with  $0.2''$  pixels in the  $J$ -,  $H$ -, and  $K$ -bands (390 – 1220 nm) for each magnetar to search for binary companions. For 8 magnetars in the southern portion of the Galactic disk, the VISTA Variables in the Via Lactea (VVV) survey was queried for  $J$ -,  $H$ -, and  $K_S$ -band images with  $0.2''$  pixels (Nikzat et al. 2022). Images for the five remaining magnetars were obtained from the Two-Micron All-Sky Survey (2MASS)<sup>23</sup>, which surveys the full sky in the  $J$ -,  $H$ -, and  $K_S$ -bands at much lower  $\sim 3''$  resolution ( $\sim 2''$  pixels; Skrutskie et al. 2006). The UKIDSS Galactic Plane Survey (UGPS)<sup>24</sup> catalog, 2MASS point source catalog, and VVV Infrared Astrometric Catalogue (VIRAC)<sup>25</sup> were queried in a cone search for discrete objects within  $0.5'$  of each magnetar (Skrutskie et al. 2006; Nikzat et al. 2022; Lucas et al. 2008; Lawrence et al. 2012, 2013; Smith et al. 2018). Additional sources were identified ‘by-eye’ in each image to include in the search.

The criteria used for the IR search are below:

- (i) The source and magnetar are located at the same RA and declination.
- (ii) If we assume the source’s absolute  $H$ -band magnitude and  $J - H$  color are stellar in nature and resemble that of a bound OB star ( $-2.76 \lesssim M_H \lesssim 3.34$ ,  $-0.14 \lesssim J - H \lesssim 0.31$  are 95% confidence ranges from Chrimes et al. (2022b) population synthesis), the distance is equal to the magnetar’s distance.

for which we define p-values  $p_1$  and  $p_2$ , respectively. Kron magnitudes are not available from the included IR catalogs. The p-values are combined using:

$$p = 1 - (1 - p_1)(1 - p_2) \quad (4)$$

An explicit derivation of these p-values is provided in Appendix B2. Note the p-value is only evaluated for magnetars and sources with position errors, and only for 2MASS and VVV sources with at least  $H$ - and  $J$ - band magnitudes. Chrimes et al. (2022b) revealed that magnetar surface IR emission can be easily mistaken for a companion star, with IR magnitudes  $M_H \gtrsim 2.5$  (see Chrimes et al. 2022b, Figure 5). Although interacting binaries such as SGR 0755-2933 can be far brighter (its companion CPD-29 2076 has  $M_H \sim -4$ ), passive binaries like PSR J0210+5845 are much fainter in the absence of mass transfer (its companion B0V star has  $M_H \sim 0.5$ ; Tan et al. 2020). Both magnitude and color must be considered to distinguish massive stellar companions from surface emission, which we account for in  $p_2$ .

<sup>23</sup> <https://irsa.ipac.caltech.edu/Missions/2mass.html>

<sup>24</sup> <https://vizier.cfa.harvard.edu/viz-bin/VizieR?-source=II/316>

<sup>25</sup> <https://vizier.cfa.harvard.edu/viz-bin/VizieR?-source=II/364>

### 4.3 Optical and IR Search Results

Using a 95% confidence level, we recover the proposed Be star bound companion of magnetar candidate SGR 0755-2933, CPD-29 2176, through the optical (PS1) and IR (UKIDSS) searches with  $p < 0.1\%$ <sup>26</sup> (Chrimes et al. 2022b; Richardson et al. 2023). In the following sections, we discuss the association of a PS1 source with the companion of SGR 0755-2933's error circle and the non-recovery of the proposed counterpart of CXOU J171405.7-38131. Figure 3 shows optical and IR images for these three magnetars. Candidate companions were identified with  $p < 5\%$  for PSR J1622-4950 and SGR J1822.3-1606, but are most likely false positives as discussed in Appendix C3.

#### 4.3.1 PS1 Counterpart of SGR 0755-2933's Be Star Companion

Five IR candidates and three optical candidates were recovered with  $p < 5\%$  as potential companions of SGR 0755-2933. The abundance of sources is due to its large  $3'$  position error (Barthelmy et al. 2016). This sample includes the known 2MASS counterpart to the proposed companion star CPD-29 2176, 2MASS J07554248-2933535. We also recover a PS1 source within the 2MASS source's 60 mas error circle, PSO J118.9270-29.5649, and therefore conclude this is the optical counterpart of CPD-29 2176.

However, we note that the association of SGR 0755-2933 with CPD-29 2176 is tenuous due to the former's lack of activity; only one burst localized to a  $3'$  region by the *Swift* telescope has been detected (Barthelmy et al. 2016). While a revised position uncertainty  $0.4''$  was derived by Richardson et al. (2023) by assuming its association with CPD-29 2176, Doroshenko et al. (2021) identify 8 persistent X-ray sources within the  $3'$  error circle. This prevents a confident association of the burst with any persistent source, including CPD-29 2176. Although Richardson et al. (2023)'s spectral analysis confirms the presence of an HMXB containing CPD-29 2176 (formally 2SXPS J075542.5-293353), a second burst localized to the binary is required to confirm that it contains SGR 0755-2933.

#### 4.3.2 CXOU J171405.7-38131

We do not recover the infrared source, VIRAC 384090103, proposed by Chrimes et al. (2022b) as a potential stellar companion to CXOU J171405.7-38131 (Smith et al. 2018; Nikzat et al. 2022). If placed at the distance of the magnetar,  $3.8 \pm 0.5$  kpc, the source has an  $H$ -band magnitude  $M_H \approx -0.9 \pm 0.1$  consistent with an OB star and its color  $J - H \approx -0.5 \pm 0.3$  differs only marginally. We note that the magnetar lies along a highly extincted sightline outside of the *Bayestar19* range, making its  $A_V \approx 22.1 \pm 0.8$  from the  $N_H - A_V$  relation an upper limit (Predehl & Schmitt 1995). This biases the Monte Carlo p-value test since the extinction cannot be estimated as a function of distance. Therefore, the location of the magnetar and source make this analysis inconclusive, and we cannot rule out VIRACS 384090103 as a potential companion of CXOU J171405.7-38131.

<sup>26</sup> For the optical and IR searches we use 1000 trials, setting lower an upper limits of  $0.1 < p < 99.9\%$  on the p-value.

## 5 RADIO SEARCH FOR SNR SHELLS

### 5.1 RACS, VLASS, and NVSS Data and Search Method

While numerous continuum radio searches for SN shells have been conducted (see e.g. Green 2019; Lorimer et al. 1998; Dubner & Giacani 2015, for comprehensive reviews) as have searches for compact objects near SNRs (e.g. Kochanek et al. 2019; Kochanek 2018, 2021, 2023), few targeted searches for SNRs near compact objects have been carried out beyond individual sources. Leveraging the young ages ( $\lesssim 1$  Myr, e.g. Suzuki et al. 2021) we search for evidence of SNRs among the magnetar sample.

The RACS-low Data Release 1 (DR1) contains images with  $15''$  resolution at 888 MHz, with a limiting sensitivity of  $0.25$  mJy beam<sup>-1</sup> (McConnell et al. 2020; Hale et al. 2021). Public images are smoothed to a common pixel scale  $25''$ . 20 magnetars and 6 magnetar candidates without confirmed SNRs fall within the survey region  $-80^\circ < \delta < +30^\circ$ . We obtained  $1^\circ \times 1^\circ$  radio image cutouts via the RACS Data Access Portal<sup>27</sup>. For two magnetars (SGR 0501+4516 and 1E 2259+586) with  $\delta > +30^\circ$ , images from the Karl G. Jansky Very Large Array Sky Survey (VLASS), which covers  $\delta > -40^\circ$  with  $0.12$  mJy sensitivity, were obtained using the Canadian Initiative for Radio Astronomy Data Analysis (CIRADA<sup>28</sup>) cutout service (Gordon et al. 2020, 2021, 2023a). VLASS Quick-Look images<sup>29</sup> are taken at 3 GHz with  $1''$  pixel scale, which we bin to  $25''$  to search for extended emission. For three magnetars covered by neither VLASS nor RACS (4U 0142+61, SGR 0418+5729, and SGR 2013+34), we obtain cutouts from the 1.4 GHz National Radio Astronomy and VLA Sky Survey (NVSS)<sup>30</sup>, a precursor to VLASS (Condon et al. 1998). This catalog contains images with  $15''$  pixels and RMS noise  $0.5$  mJy beam<sup>-1</sup>, or  $\sim 0.8$  mJy beam<sup>-1</sup> for  $25''$  pixels<sup>31</sup>. One magnetar, SGR 1627-41, is not covered by any of the radio surveys discussed<sup>32</sup>.

The Set of Identifications, Measurements and Bibliography for Astronomical Data (SIMBAD<sup>33</sup>) database was queried for known SNRs, SNR candidates, and unidentified radio sources with 'ISM' object-types<sup>34</sup> within the same  $1^\circ \times 1^\circ$  region for each magnetar (Egret et al. 1991). If a previously proposed SNR candidate was not found in the initial SIMBAD query, it was added manually to the sample for the association test (for example, SNR HBH 9 is associated with SGR 0501+4516, but falls more than  $1.3^\circ$  away and was missed in the query). Additional sources which may be SNRs are identified 'by eye' to include in the search (see Appendix B3.1). Sources identified as known radio galaxies or AGN were removed from the sample. While a radio image is not available for SGR 1627-41, we proceed with the association test using SIMBAD radio sources within

<sup>27</sup> <https://data.csiro.au/>

<sup>28</sup> <https://cirada.ca/vlasscatalogueql0>

<sup>29</sup> Epochs 3.1 and 2.2 are used for magnetars SGR 0501+4516 and 1E 2259+586, respectively.

<sup>30</sup> <https://www.cv.nrao.edu/nvss/postage.shtml>

<sup>31</sup> VLASS data is taken in the B configuration which is sensitive to angular scales between  $2.1 - 58''$ . NVSS data is taken in the D and DnC configurations which are sensitive to angular scales between  $14 - 970''$  and  $46 - 970''$ , respectively. See <https://science.nrao.edu/facilities/vla/docs/manuals/oss/performance/resolution> for details.

<sup>32</sup> While this magnetar does fall in the survey range of RACS-DR1, no continuum images are available that contain SGR 1627-41 in its field-of-view.

<sup>33</sup> <https://simbad.u-strasbg.fr/simbad/sim-fbasic>

<sup>34</sup> See <https://simbad.cds.unistra.fr/guide/otypes.htx> for details on SIMBAD object-types.

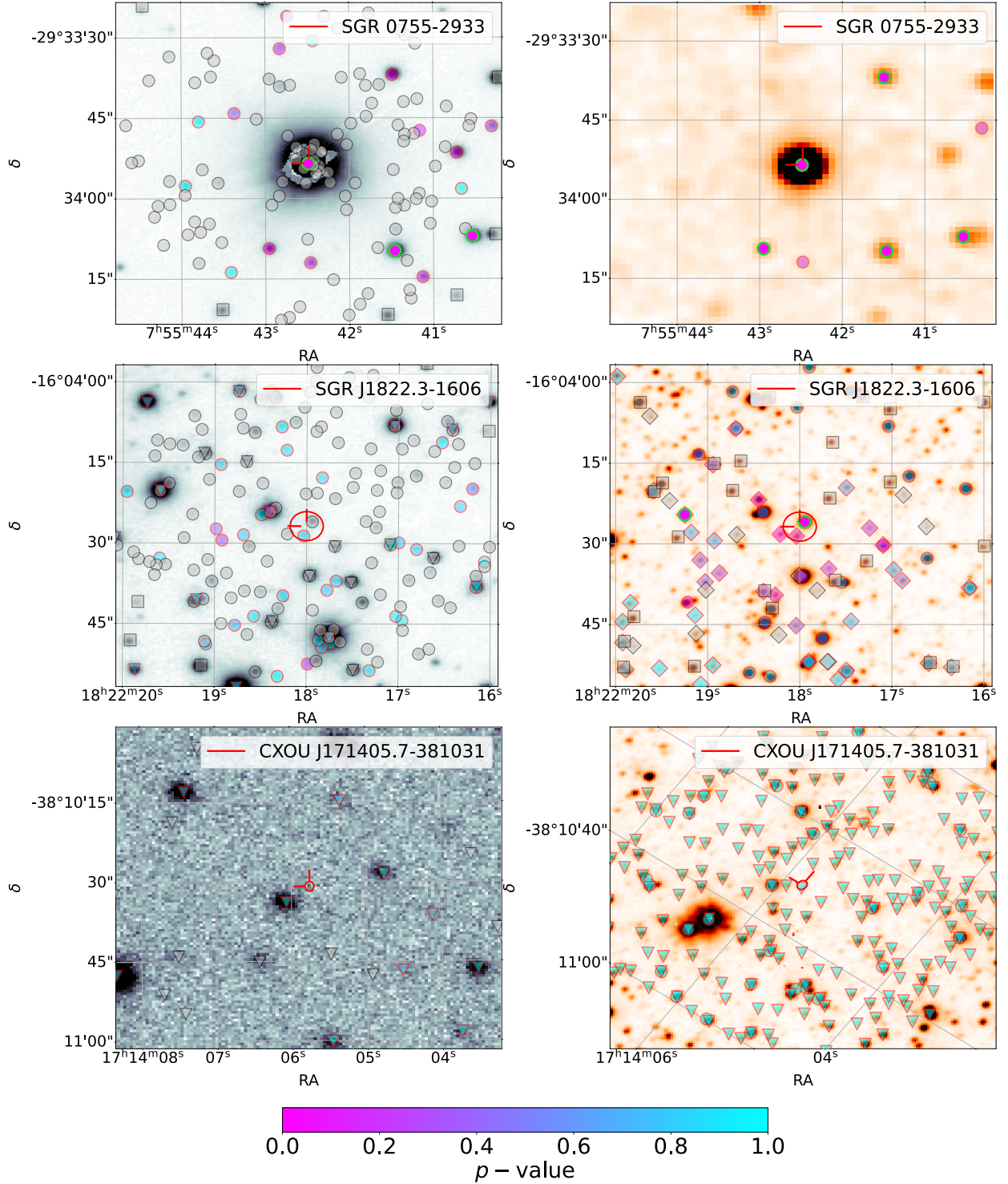


**Figure 3.** Optical (*Left*) and Infrared (*Right*)  $1' \times 1'$  image cutouts for 2 magnetars and 1 magnetar candidate. Each image is in grayscale where RGB channels are combined using  $0.2989R + 0.5870G + 0.1140B$ . Optical images use the  $g$ -,  $i$ -, and  $y$ -band filters for PS1 images (CXOU J1714) and the  $g$ -,  $r$ -, and  $i$ -band filters for SkyMapper images (SGR 0755 and SGR J1822). Infrared images use the  $J$ -,  $H$ -, and  $K$ -band filters for UKIDSS images (SGR 1822) and the  $J$ -,  $H$ -, and  $K$ -band filters for VVV (CXOU J1714) and 2MASS (SGR 0755) images. The magnetar location is indicated by red cursors and the  $3\sigma$  error ellipse is shown in red. Note the error ellipse is much larger than the image for SGR 0755-2933. Each marker indicates a point source from the optical or infrared catalogs with colorbar corresponding to the association  $p$ -value,  $p$ . Sources with insufficient data to determine a  $p$ -value are grey. Sources with  $p < 5\%$  are outlined in green, while those with  $p > 5\%$  are outlined in red. (*Left*) PS1 sources are shown as circles, SkyMapper sources are shown as triangles, and sources identified ‘by-eye’ are shown as squares. (*Right*) 2MASS sources are shown as circles, VVV sources are shown as triangles, UKIDSS sources are shown as diamonds, and sources identified ‘by-eye’ are shown as squares. Sources with no corresponding marker were not identified in the catalogs considered, and could not be well-fit with an ellipse. The Be-star companion of SGR 0755 is recovered in the optical and infrared searches, and candidates are identified for SGR 1822. The proposed companion of CXOU J1714 is not recovered, but cannot be ruled out as a bound companion due to uncertainty in the extinction estimate. Note that the axes for CXOU J1714 differ between optical and infrared due to the use of different World Coordinate System (WCS) projections (ZPN) for VVV data (e.g. Greisen & Calabretta 2002).

1°. Through a Monte Carlo search, p-values are estimated with the criteria below:

- (i) The SNR and magnetar are located at the same RA and declination.
- (ii) The magnetar’s proper motion direction is consistent with the direction required to intersect the SNR.
- (iii) The magnetar’s proper motion and age are consistent with the observed angular separation of the magnetar and SNR.
- (iv) The SNR’s dynamical age is consistent with an SNR shell rather than a point source.

for which we define p-values  $p_1, p_2, p_3$ , and  $p_4$ , respectively. Appendix B3 contains a derivation of these p-values explicitly. Unlike in the binary companion searches, criteria (i)-(iii) relate to two independent cases: first that the magnetar is located within the SNR shell (i), and then that the magnetar has travelled some distance away from the SNR during its lifetime (ii and iii). Therefore, unless  $p_1 < 0.1\%$  or  $1 - (1 - p_2)(1 - p_3) < 0.1\%$ <sup>35</sup>, we combine  $p_1, p_2$ , and  $p_3$  using the Fisher statistic<sup>36</sup>:

$$\hat{\chi}^2_4 = -2(\ln(p_1) + \ln(1 - (1 - p_2)(1 - p_3))) \quad (5)$$

This follows a  $\chi^2$  distribution with 4 degrees of freedom, from which we compute the p-value  $p_\chi$  using the inverse survival function. We then combine this with  $p_4$  using:

$$p = 1 - (1 - p_\chi)(1 - p_4) \quad (6)$$

Note that  $p_1$  requires definition of the RA and declination errors for the magnetar and either the RA and declination errors or angular size and position angle for the SNR.  $p_2$  and  $p_3$  additionally require definition of the magnetar proper motion errors and the X-ray decay or characteristic age.  $p_4$  requires the angular size or position error to be defined.

## 5.2 Radio SNR Search Test with Known Magnetar-SNR Associations

8 magnetars and 2 magnetar candidates with confirmed SNR associations are used to test the radio image search method. With the analysis above, we accurately recover the associated SNRs with  $p < 5\%$  for 7 magnetars and both magnetar candidates. SGR 1627-41 is the only confirmed SNR association that we fail to recover in the radio search (SNR G337.0-00.1; Corbel et al. 1999), which is likely due to the large angular offset  $\sim 15.5'$ . No proper motion is known for SGR 1627-41, but a velocity  $\sim 1275 \text{ km s}^{-1}$  would be required given its  $\mathcal{T}_{\text{decay}} \approx 37.0 \text{ kyr}$ , which is in marginal agreement with the Hobbs et al. (2005) distribution. Given that 9 of the 10 trials were successful in recovering the associated SNRs, we proceed with confidence that the image-plane and Monte Carlo search methods are effective. Radio images for five magnetars with proposed SNR associations are shown in Figure 5.

## 5.3 Radio SNR Search Results

Among the 14 magnetars and magnetar candidates with no previous SNR associations, we identify two candidates which have  $p < 5\%$ . One of these, associated with SGR 0755-2933 is most likely

a false positive which we discuss in Appendix C2. For SGR 1808-20, we find two viable SNR association candidates which require proper motion and distance measurements to properly assess. Of the seven magnetars and magnetar candidates with proposed but unconfirmed or rejected SNRs we recover five (and marginally recover a sixth with  $p = 5.6\%$ ), one of which is nearby the Galactic Center magnetar SGR J1745-2900 and another of which would suggest 3XMM J185246.6+003317 has an ejected pulsar companion. In this section, we discuss the SNR candidates for SGR 1808-20 and the recovered unconfirmed SNR candidates in detail.

### 5.3.1 SGR 1808-20

For SGR 1808-20, we find multiple candidate radio sources (29) with  $p < 0.1\%$ , 10 of which were selected for analysis ‘by-eye’ rather than through the SIMBAD query. The large number of sources comes from the loose position ( $\sim 7'$  error) and distance (no measurement) constraints, as only one burst has been detected from the magnetar since its discovery (Lamb et al. 2003).  $2' \times 2'$  VLASS cutouts at  $1''$  scales were obtained for each candidate, revealing that 6 of the 29 sources were resolved and unlikely to be SNRs. One source is a known Young Stellar Object (YSO) while another is an unidentified sub-millimetric source, both of which are unlikely to be SNRs (Eden et al. 2017). 14 are labelled as ‘dense cores’, or InfraRed Dark Clouds (IRDCs) which are pre-star forming regions that may be the birthplaces of massive stars (Jiao et al. 2023). IRDCs are distinguished from SNRs based on their high masses ( $\sim 100M_\odot$ ) and hydrogen column densities ( $N_H \sim 10^{23} \text{ cm}^{-2}$ ), essentially ruling out these candidates (e.g. Güver & Özel 2009).

Six of the seven remaining sources are ‘by-eye’ candidates; we query the SIMBAD database within  $1'$  of each source to identify potentially missed sources of radio emission. One is nearby PSR J1808-2057 which has a radio flux 2.3 mJy and is likely responsible for the observed emission (Hobbs et al. 2004). Another is coincident with a  $\sim 532M_\odot$  molecular cloud discovered through sub-millimeter ( $\sim 0.1 - 1 \text{ THz}$ ) emission, making it a plausible radio source (Duarte-Cabral et al. 2021). One is coincident with an infrared-bright ‘bubble’; these are star-forming sites in HII regions and are therefore also plausible radio sources (Simpson et al. 2012). Two others are coincident with stars, one an AGB star and the other an eclipsing binary system, both of which are potentially radio bright, though no radio flux has yet been catalogued (Heinze et al. 2018; Spangler et al. 1977; Cutri et al. 2003). While these five sources cannot be confidently ruled out, we will assume they are not associated given the possible contamination by nearby objects. This leaves two sources as candidates for association: SNR G009.7-00.0 and an unidentified radio source, which we formally label S24-RACS J180842-202849, with no SIMBAD objects within  $1'$ . For the remaining discussion, we will refer to the latter source as ‘Source 1’.

Source 1 was identified by eye at  $18^{\text{h}}08^{\text{m}}42^{\text{s}} - 20^{\circ}28'45''$  and fit with an ellipse of approximate major and minor axes  $a \sim b \sim 18''$ . This lies very near the position of another magnetar, SGR 1806-20, and the W31 HII region (e.g. Frail & Clifton 1989; Corbel & Eikenberry 2004; Moisés et al. 2011). The distance to W31 has been disputed in the literature; if we adopt the distance of SGR 1806-20,  $8.7^{+1.8}_{-1.5} \text{ kpc}$ , Source 1 would have a radius  $\sim 0.8 \text{ pc}$ . At this size the SNR would be in the free-expansion phase, and assuming  $n_0 \sim 1 \text{ cm}^{-3}$ , we estimate the age of the remnant to be between 0.3–1.2 kyr (Sedov 2018). This is roughly consistent with  $\mathcal{T}_{\text{rot}}$  and  $\mathcal{T}_{\text{decay}}$  for magnetars, but the lack of data for SGR 1808-20 prevents a direct comparison. A detailed composition analysis is required to confirm

<sup>35</sup> The minimum p-value is set by the 1000 trials used for the SNR search.

<sup>36</sup> [https://en.wikipedia.org/wiki/Fisher%27s\\_method](https://en.wikipedia.org/wiki/Fisher%27s_method)

Source 1 as a supernova remnant, though its morphological similarity to other false positives implies it is unlikely to be an SNR.

SNR G009.7-00.0, on the contrary, was detected by [Frail et al. \(1994\)](#) and confirmed through its OH maser by [Hewitt & Yusef-Zadeh \(2009\)](#), which constrained its distance to  $\sim 4.7$  kpc. [Yeung et al. \(2016\)](#) find its distance is inconsistent with W31 and SGR 1806-20. At  $\sim 4.7$  kpc, the  $\sim 11 - 15'$  angular size corresponds to a radius  $\sim 8 - 10$  pc, suggesting a free-expansion age of  $\sim 10$  kyr. Both Source 1 and SNR G009.7-00.0 appear to be viable candidates for association with SGR 1808-20, but a magnetar distance measure and more tightly constrained position are necessary to investigate further. The radio image is shown in Figure 5.

### 5.3.2 3XMM J185246.6+003317 and CXOU J185238.6+004020 as an Unbound Double Neutron Star Binary

For 3XMM J185246.6+003317 we recover the Kes 79 SNR (SNR G033.6+00.1) with  $p < 0.1\%$ , which is associated with a central X-ray pulsar CXOU J185238.6+004020 (PSR J1852+0040; e.g. [Gotthelf et al. 2005](#); [Malofeev et al. 2005](#); [Bogdanov 2014](#)). [Bogdanov \(2014\)](#) derive a Sedov-Taylor expansion age of  $\sim 5$  kyr for the SNR which contrasts with both the decay age  $\mathcal{T}_{\text{decay}} \approx 0.7$  Myr<sup>37</sup> and spindown age  $\mathcal{T}_{\text{rot}} \gtrsim 1.3$  Myr of 3XMM J185246.6+003317.<sup>38</sup> Magnetars are typically expected to be unobservable beyond  $\sim 10^4$  years; however, the spindown age  $\mathcal{T}_{\text{rot}}$  is a well-constrained lower limit derived by [Rea et al. \(2014\)](#) from an X-ray timing solution. They find a pulse period  $P = 11.55871346(6)$  s with no discernible spindown, leading to upper limits of  $\dot{P} < 1.4 \times 10^{-13}$  s s<sup>-1</sup> and  $B_{\text{dip}} \lesssim 10^{13}$  G. on the spindown rate and magnetic field. While these parameters are reminiscent of typical radio pulsars, [Zhou et al. \(2014\)](#) noted in their initial discovery that the X-ray luminosity ( $\sim 10^{33-34}$  erg s<sup>-1</sup>) far exceeds its spindown luminosity ( $\sim 10^{30}$  erg s<sup>-1</sup>) making its magnetar nature robust. Therefore we take both the spindown age and the decay age to be reasonable age estimates. This suggests that Kes 79 is associated with CXOU J185238.6+004020, but allows a scenario wherein the pulsar and magnetar were gravitationally bound in the past ([Zhou et al. 2014](#)).

Considering this case, let the initially bound massive star progenitors of 3XMM J185246.6+003317 and CXOU J185238.6+004020 be called stars 1 and 2, respectively. When the CCSN of star 1 disrupts the binary<sup>39</sup>, the remnant magnetar (3XMM J185246.6+003317) and star 2 are ejected at  $\sim 300$  km s<sup>-1</sup> and  $\sim 6$  km s<sup>-1</sup>, respectively ([Hobbs et al. 2005](#); [Renzo et al. 2019](#)). After travelling for  $\sim 0.7$  Myr based on the magnetar's age, the CCSN of star 2 would then kick the remnant pulsar (CXOU J185238.6+004020) at  $\sim 300$  km s<sup>-1</sup>, leaving behind the remnant shell Kes 79. This sequence of events is shown in Figure 4. We investigate this scenario by applying a modified *Gaia* unbound companion search pipeline to the magnetar and CXOU J185238.6+004020's *Gaia* counterpart,

<sup>37</sup> More recent constraints on the magnetic field from ray-tracing simulations by [de Lima et al. \(2024\)](#) suggest  $\mathcal{T}_{\text{decay}} \gtrsim 1.2$  Myr, though they caution not to over-interpret their initial estimates.

<sup>38</sup> While the spindown age of CXOU J185238.6+004020 is  $\sim 192$  Myr, 'anti-magnetars' or 'compact central objects' (CCO) like this are known to have overestimated spindown ages due to the complex relation of their low magnetic fields to a dynamo process ([Gotthelf & Halpern 2008](#); [Halpern et al. 2007](#); [Gotthelf et al. 2013](#)).

<sup>39</sup> The alternate case in which star 2 undergoes the first CCSN is equally likely, but we focus the discussion on this scenario which is more consistent with the age estimate for 3XMM J185246.6+003317.

*Gaia* DR3 4266508881354196736. We split the companion's trajectory into two parts with different velocities to account for the two CCSN events, assume the absolute magnitude of the companion is  $M_V > 0$ , and neglect  $p_2$  since the magnetar's and pulsar's travel times no longer coincide directly. 10000 trials (rather than 100) are used since the magnetar has no proper motion measurement.

The resulting trajectory plot is shown in Figure 4; we find a  $p$ -value  $p_{1,3} = 0.02\%$ , suggesting that this scenario is likely. From the 497 valid samples out of 10000, the scenario requires the magnetar to have velocity  $|\vec{v}_{\text{mag}}| \approx 398^{+208}_{-165}$  km s<sup>-1</sup> (proper motion  $\mu_{\alpha} \cos(\delta) \approx -2.1^{+1.2}_{-5.8}$  mas yr<sup>-1</sup>,  $\mu_{\delta} \approx -9.8^{+4.9}_{-20.8}$  mas yr<sup>-1</sup>) and a travel time  $\mathcal{T}_{3\text{D},\text{mag}} \approx 40.1^{+56.1}_{-21.8}$  kyr, which is consistent with expected magnetar ages, but disagrees with [Rea et al. \(2014\)](#), [Zhou et al. \(2014\)](#), and  $\mathcal{T}_{\text{decay}}$ . Despite the robustness of the X-ray timing solution, magnetars are known to glitch, anti-glitch, and slowly recover from glitches during outbursts such as the one used for timing analysis (e.g. [Tong & Huang 2020](#); [Younes et al. 2023](#); [Scholz et al. 2014](#); [Archibald et al. 2013](#)). Coupled with [Rea et al. \(2014\)](#) observing the outburst at a late time, this implies that 3XMM J185245.6+003317 may have experienced a glitch event leading to its undetectable spindown. If we impose  $\mathcal{T}_{3\text{D},\text{mag}}$  as an age constraint, then using the period  $P = 11.55871346(6)$  s we derive a revised spindown rate of  $\dot{P} \approx 4.6^{+5.4}_{-2.7} \times 10^{-12}$  s s<sup>-1</sup>, and dipolar magnetic field  $B_{\text{dip}} \approx 2.3^{+1.1}_{-0.2} \times 10^{14}$  G, both of which are more consistent with the magnetar sample.

The pulsar requires a velocity  $|\vec{v}_{\text{psr},1}| \approx 8^{+11}_{-4}$  km s<sup>-1</sup> following the first CCSN, and  $|\vec{v}_{\text{psr},2}| \approx 422^{+192}_{-172}$  km s<sup>-1</sup> following the second. The most supportive evidence for this scenario is the position of the pulsar's CCSN, estimated from valid samples as 18<sup>h</sup>52<sup>m</sup>38<sup>s</sup>.60 + 00°40'20".09 with a  $1\sigma$  errors of 0.2' and 0.4' in RA and declination respectively. This is roughly  $8\sigma$  away from the centroid of Kes 79, 18<sup>h</sup>52<sup>m</sup>48<sup>s</sup>.00 + 00°41'00", but is well within its  $\sim 5'$  radius. We obtain an estimate of 18<sup>h</sup>52<sup>m</sup>56<sup>s</sup>.5 + 00°43'57".5 with errors  $\sigma_{\alpha} \sim 3'$  and  $\sigma_{\delta} \sim 6'$  for the position of the first CCSN. This also lies within the extent of Kes 79, and suggests that its unique multi-shell structure may result from interactions between the magnetar and pulsar SNR shock fronts. Other single-SNR scenarios have been presented to explain this structure as, for example, the interaction of the SNR with a molecular cloud or the progenitor's stellar wind ([Velusamy et al. 1991](#); [Giacani et al. 2009](#); [Sun et al. 2004](#); [Sato et al. 2016](#); [Zhou et al. 2016](#)). We conclude that it is likely that the progenitors of 3XMM J185246.6+003317 and CXOU J185238.6+004020 began in a bound system prior to the former's CCSN, and a proper motion measurement for 3XMM J185246.6+003317 would further constrain their formation history.

### 5.3.3 SGR J1745-2900, the Galactic Center Magnetar

SGR J1745-2900 is a unique magnetar at the Galactic Center (GC) of the Milky Way ([Mori et al. 2013b](#)). The radio emission from the supermassive black hole Sag A\* and high density of radio sources in this region make it difficult to identify any associations with confidence. The black hole would also distort an SNR shell from SGR J1745-2900 (e.g. [Yalinewich et al. 2017](#)). However, [Ponti et al. \(2015\)](#) used high resolution X-ray observations to catalog extended regions near the GC, identifying the GC X-ray/radio lobes as a warped and mirrored SNR. SGR J1745-2900 lies near the intersection of the two lobes, and [Yalinewich et al. \(2017\)](#) use numerical simulations to demonstrate that an 'engulfing' SNR explosion at this location could produce the observed SNR structure.

Given this analysis, the radio lobes were added to the simulation

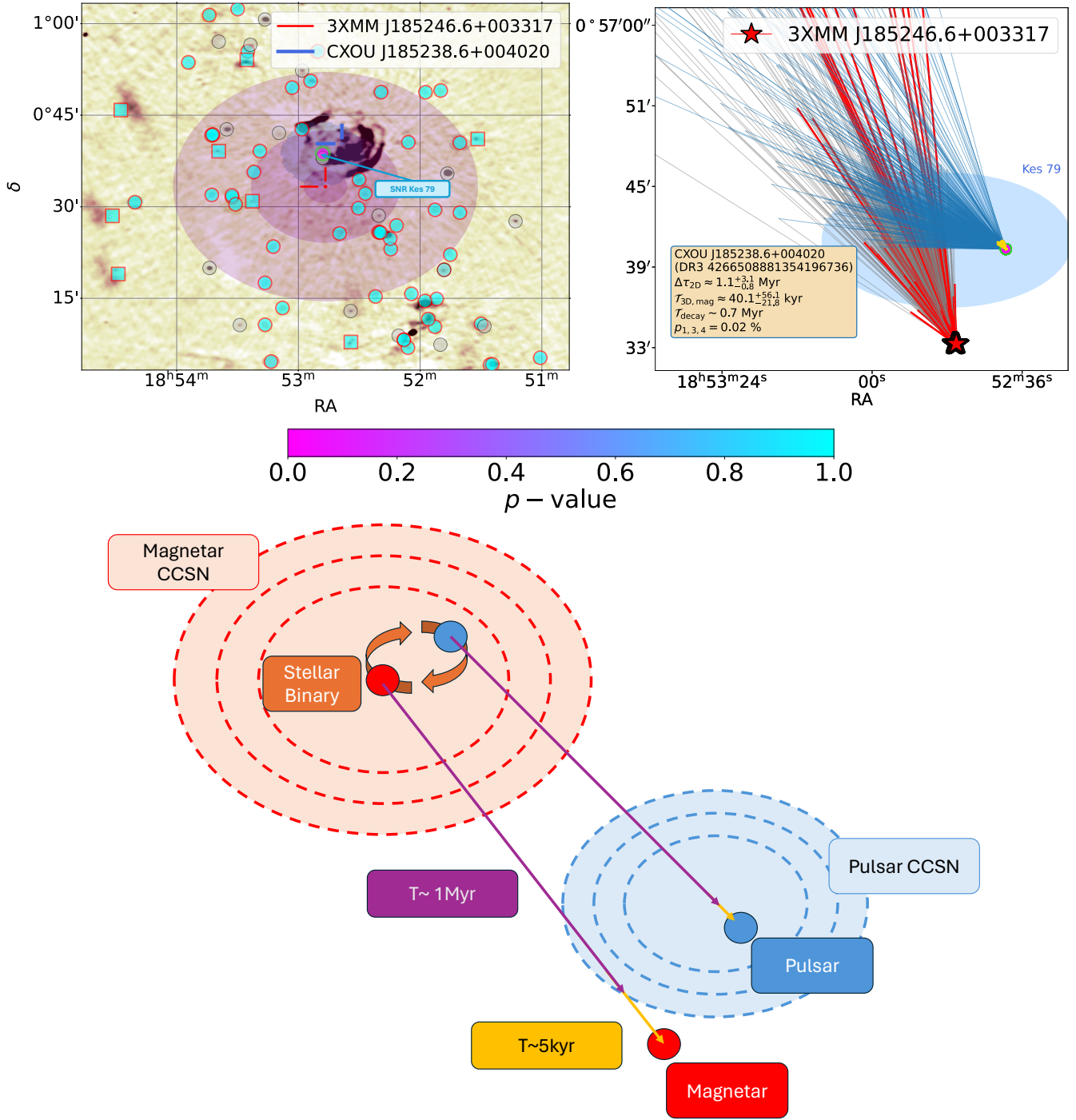


**Figure 4.** Radio Image and Trajectory Analysis of 3XMM J185246.6+003317. (Top left) A RACS DR1 888 MHz continuum  $1^\circ \times 1^\circ$  image cutout is shown for 3XMM J185246.6+003317 with  $25'' \times 25''$  pixels. The magnetar and pulsar locations are indicated by red and blue pointers, while circular and square markers show known and ‘by-eye’ identified radio sources, respectively. Note that no markers are shown for catalogued Active Galactic Nuclei or radio galaxies, as they were not included in this search. Other extended sources without markers were not identified in SIMBAD and could not be well-fit with an ellipse. The colorbar corresponds to the association p-value. The purple shaded region indicates the 1, 2, and  $3\sigma$  past travel distances based on the [Hobbs et al. \(2005\)](#) velocity distribution. The angular extent of Kes 79 (labelled) is shown as a blue circle. (Bottom) The cartoon demonstrates how a bound massive stellar binary (orange) may evolve into an unbound magnetar (red) and pulsar (blue) following two CCSNe. (Top right) The trajectory plot for 3XMM J185246.6+003317 and the X-ray pulsar CXOU J185238.6+004020 is shown with 468 valid trajectories (out of 10000 trials). Blue traces show the pulsar’s trajectory prior to the second CCSN, and yellow traces show its trajectory after the CCSN. The blue circle indicates the location and extent of Kes 79.

using the centroid position ( $17^{\text{h}}45^{\text{m}}32^{\text{s}}.3 - 29^{\circ}2'32''.5$ ) and angular diameter  $\sim 5.8'$  from [Ponti et al. \(2015\)](#). Through the Monte Carlo simulation, we recover the radio lobes, as well as a gamma-ray source 0FGL J1746.0-2900 found not to be an SNR ([Acero et al. 2016](#)) and an HII region ([Nguyen et al. 2015](#)), with  $p < 0.1\%$ . In our simplified model of the lobes, we do not account for the irregular structure of the SNR, but instead assume the SNR is centered at the lobes' centroid with angular size equal to a single lobe. This simplification should not greatly impact the results since only a lower limit is imposed on the SNR's dynamical age based on the angular size. The position of the radio lobes' centroid is marginally consistent with the trajectory of SGR J1745+1900 (see Figure 5). With a proper motion magnitude  $\sim 6.4 \text{ mas yr}^{-1}$ , the  $\sim 2.7'$  separation suggests an SNR age  $\sim 25$  kyr, which is slightly lower than the decay age estimate  $\mathcal{T}_{\text{decay}} \approx 64.9$  kyr. Further interpretation requires a more detailed analysis of the GC lobe geometry, but our results support a scenario where the bipolar radio lobes are the SNR of SGR J1745+1900.

### 5.3.4 Other Magnetars with Unconfirmed SNRs

Five other magnetars in the sample were identified in previous searches as potential associations of nearby supernovae, but have not yet been confirmed: SGR 1900+14, SGR 1806-20, SGR 0526-66, SGR 0501+4516, and SGR 1801-23. SGR 1900+14's association with SNR G042.8+00.6 (for which we find  $p = 5.6\%$ ) was rejected by [Vrba et al. \(2000\)](#) given the former's more likely association with a star cluster. We identify one additional by-eye source, S24-RACS J190707+091737, as an SNR candidate with  $p < 0.1\%$ , but rule it a false positive as it disagrees with the proper motion direction of SGR 1900+14. SGR 1806-20's association with AX J1808.6-2024 (SNR G10.0-0.3) was also rejected by [Hurley et al. \(1999\)](#), suggesting it is not an SNR but a radio nebula powered by its central LBV star. While there is insufficient position data to estimate a p-value for the nebula, we do recover it when using the angular size of its potentially associated gamma ray emission, Fermi J1808.2-2029 ([H. E. S. S. Collaboration et al. 2018](#)).

SGR 0526-66 is located within the Large Magellanic Cloud (LMC) near SNR N49 (SNR J052559-660453; [Klose et al. 2004](#)). However, its association with SNR N49 could not be confirmed as the magnetar's proper motion is unknown, which is necessary to localize its birth place to SNR N49's host star cluster, SL 463. With our pipeline, we obtain a p-value  $p < 0.1\%$  for this association. Notably, five other 'by-eye' radio sources were recovered with  $p < 5\%$ ; however, each of these fall within  $1'$  of possible known radio sources that are not within the LMC. While SGR 0526-66 does not have a proper motion measurement, its position error of  $0.6''$  compared to the  $1.4'$  angular size result in a highly confident association. The large distance  $53.6 \pm 1.2$  kpc suggests N49 has a transverse size of roughly 22 pc, while the  $0.6''$  position error for the magnetar corresponds to  $\sim 0.1$  pc. Therefore it is likely that N49 contains SGR 0526-66, supporting [Klose et al. \(2004\)](#)'s claim of association.

For SGR 0501+4516, [Gaensler & Chatterjee \(2008\)](#) localized the magnetar to the outer rim of SNR HBH 9 (HB9 or SNR G160.9+2.6) at a position  $\sim 15'$  from the next nearest SNR. The large angular separation  $\sim 1.3^{\circ}$ , however, initially excluded SNR HBH 9 from the test sample. After adding this as a by-eye radio source, we obtain a p-value  $p = 7.0\%$ , providing insufficient evidence to confirm the association. This is most likely due to the large angular separation  $\sim 1.3^{\circ}$ ; at the magnetar's distance  $2 \pm 0.3$  kpc, this corresponds to a transverse separation of  $\sim 45$  pc. For the magnetar's decay age  $\mathcal{T}_{\text{decay}} \approx 59.4$  kyr, this would require a velocity  $\sim 730 \text{ km s}^{-1}$  for the magnetar, which agrees well with the [Hobbs et al. \(2005\)](#) distribution

expected for neutron stars. Therefore, given the marginal p-value recovered and the achievable kick velocity, we find this association remains possible, and a proper motion measurement is required to confirm or reject it.

## 6 DISCUSSION

Through this multiwavelength search of 31 magnetars and magnetar candidates, we identify one magnetar with a potential unbound OB star companion, SGR J1822.3-1606, but require proper motion data to explore further. We note that magnetar 3XMM J185246.6+003317 may be an unbound system whose progenitor was bound to that of an X-ray pulsar, CXOU J185238.6+004020. While we recover the Be star companion of SGR 0755-2933 proposed by [Richardson et al. \(2023\)](#) and the unbound Wolf-Rayet star companion of CXOU J164710.2-455216 proposed by [Clark et al. \(2014\)](#), we are unable to confidently associate the IR counterpart of CXOU J171405.7-381031 proposed as a bound companion by [Chrimmes et al. \(2022b\)](#). Through the radio search, we recover nine of ten confirmed SNR associations, propose scenarios supporting four of five unconfirmed SNR associations, and identify a new candidate SNR associated with SGR 1808-20 which requires a proper motion and distance measurement for confirmation.

Table 3 summarizes our results, which prompt a discussion of the CCSN model for magnetar formation. The recovery of only two unbound binary candidates is inconsistent with [Chrimmes et al. \(2022b\)](#) and [Renzo et al. \(2019\)](#) simulations predicting that  $f_u \sim 38 - 56\%$  of magnetars should be nearby unbound companion stars. We begin this section by analyzing our search's sensitivity before exploring the implications of the search on magnetars' massive star progenitors. We then consider potential limitations in our work and investigate the possibility of more exotic magnetar formation channels.

### 6.1 Completeness and Sensitivity Considerations

For each search, we estimate the expected ranges of intrinsic parameters and derive the ranges of their corresponding observables in order to compare to our sensitivity thresholds. For the bound companion search, we search for OB stars with intrinsic magnitudes in the following ranges:

- (i)  $-2.76 \lesssim M_H \lesssim 4.34$  ([Chrimmes et al. 2022b](#))
- (ii)  $-2.61 \lesssim M_i \lesssim 5.55$  (derived by converting the [Chrimmes et al. 2022b](#), constraints on  $M_H$  and  $J - H$  using the 2MASS relationships<sup>40</sup>)

Similarly in the *Gaia* search for unbound companions we expect:

- (i)  $-10 \lesssim M_V \lesssim 1.185$
- (ii)  $v_{\text{mag}}$  following the [Hobbs et al. \(2005\)](#) distribution
- (iii)  $v_{\text{src}}$  following the [Renzo et al. \(2019\)](#) distribution

and for the SNR search:

- (i) Radio luminosity  $L \approx 10^{42} \text{ erg s}^{-1}$  in the Rayleigh-Jeans limit ([Barker et al. 2022, 2023; Hamuy 2003](#))
- (ii) Angular size  $25'' \lesssim \Delta\theta \lesssim 1^{\circ}$  (from observed SNR sizes in the [Green \(1987\)](#) catalog and considerations of free- and Sedov-Taylor-expansion in [Truelove & McKee \(1999\)](#))

<sup>40</sup> See Section 5.5 of *Gaia* DR3 Documentation (<https://gea.esac.esa.int/archive/documentation/GDR3/>).

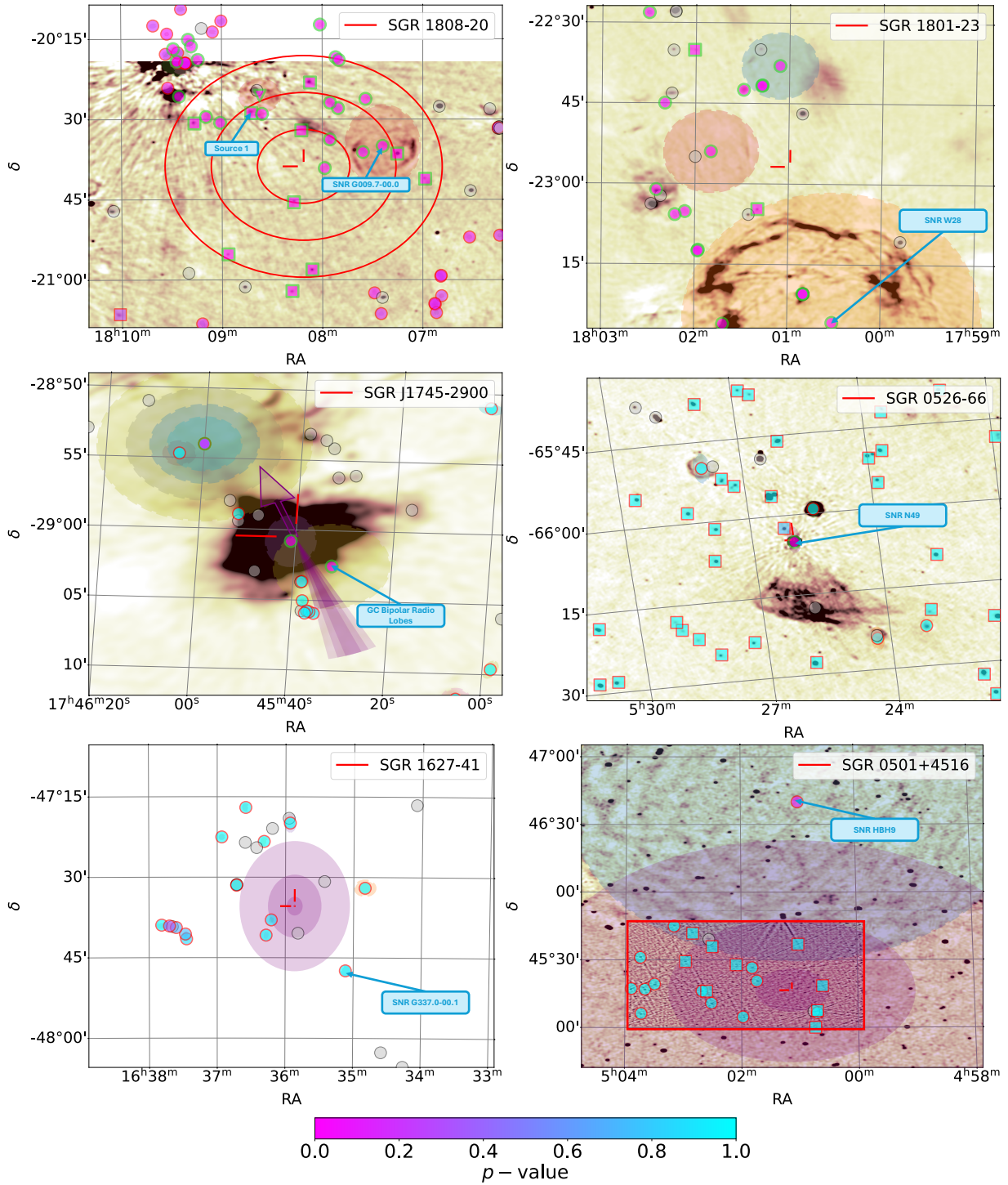


**Figure 5.** Radio continuum image cutouts for four magnetars (*middle, bottom*), and two magnetar candidates (*top*) with possible SNR associations. Red pointers indicate each magnetar’s location and the  $1\sigma$ ,  $2\sigma$ , and  $3\sigma$  magnetar error ellipses are shown in red (although they are too small to be visible except for SGR 1808-20 and SGR 1801-23. For the latter, the  $3.8^\circ$  error ellipse is too large to be effectively shown.). Note the difference in axis extents for each image. RACS 888 MHz continuum images with  $25'' \times 25''$  pixels are shown for SGR 1808-20, SGR 1801-23, SGR J1745-2900, and SGR 0526-66 (*top, middle*). For SGR 0501+4516, a 3 GHz  $1' \times 1'$  VLASS image with  $1'' \times 1''$  pixels (smoothed to  $25'' \times 25''$  with a boxcar kernel) is shown enclosed in a red box indicating the queried region, while the remainder of the image is from the 1.4 GHz NVSS survey to show SNR HBH 9 (e.g. Gögüş et al. 2010b). However, NVSS is only sensitive to angular sizes  $< 970''$  ( $\lesssim 16.7'$ ), making SNR HBH9 ( $120 - 140'$ ) unobservable in the image shown. No radio images from RACS, VLASS, or NVSS were available at SGR 1627-41’s position (*bottom left*). Circular markers indicate the locations of known radio sources while square markers indicate unknown sources identified by-eye. Note that no markers are shown for catalogued Active Galactic Nuclei or radio galaxies, as they were not included in this search. Other extended sources without markers were not identified in SIMBAD and could not be well-fit with an ellipse. The colorbar corresponds to the association p-value; sources outlined in red (green) have  $p > 5\%$  ( $p \leq 5\%$ ). The most likely or previously proposed SNRs (see Section 5.3) are labelled. ‘Source 1’ (*top left*) is S24-RACS J180842-202849. The angular extents of SNRs, if available, are shown as ellipses. For SGR 1745-2900 (*middle left*), the proper motion direction is marked by a purple arrow, and the purple shaded region indicates the  $1\sigma$ ,  $2\sigma$ , and  $3\sigma$  past travel direction and extent; for SGR 1627-41, SGR 0501+4516, and SGR 0526-66 (*bottom, middle right*), the Hobbs et al. (2005) velocity distribution is used to show possible past travel direction and extent.



By combining these constraints with the distance, extinction, and proper motion of each magnetar (see Table 1), we estimate the expected range of apparent magnitudes ( $V$ -,  $i$ -, and  $H$ -band), SNR flux at 1 GHz, and relative proper motion  $\Delta\mu$  between the magnetar and an unbound companion. Figure 6 and Table 3 summarize the results. Four magnetars have no distance measurements and are not included in this analysis.

For the *Gaia* search we observe that the relative proper motion of each magnetar and a walk/runaway companion should be detectable down to  $M_G \sim 21$  given the proper motion uncertainty  $\sigma_\mu \approx 1.4 \text{ mas yr}^{-1}$  (Collaboration et al. 2022). Only the SMC magnetar CXOU J010043.1-721134 is partially incomplete for faint stars due to its large distance. However, four magnetars lie along high-extinction sightlines with  $A_V \gtrsim 17$  (CXOU J171405.7-381031, IE 1547.0-5408, PSR J1622-4950, SGR 1627-41) making unbound companions undetectable at *Gaia*'s  $M_V < 20.7$  sensitivity. 19 magnetars are partially complete, meaning that our search may miss fainter B-star companions. These results are more promising than indicated by the simulations of Chrimes et al. (2023), which determined that without the aid of next generation deep-field surveys, *Gaia* may recover only a small fraction of unbound neutron star companions. This demonstrates that incorporating a trajectory search into our Monte Carlo analysis can make significant improvements to our search sensitivity.

The bound search is complete or partially complete for most magnetars covered by the IR survey; only SGR 1627-41, which has a large extinction  $A_V \approx 55.87 \pm 11.17$ , and the two magnetars in Magellanic Clouds, CXOU J010043.1-721134 and SGR 0526-66 are incomplete. The optical search, on the other hand, is incomplete for six magnetars due to their high extinction. This is in agreement with Chrimes et al. (2022b), which concluded that IR searches are more effective for OB stars due to the  $\sim 4\times$  lower extinction in  $H$ -band compared to  $i$ -band (e.g. Green 2019). Finally, the SNR search is complete in all cases, although this may be altered when incorporating dynamics beyond the free-expansion phase (e.g. Truelove & McKee 1999; Salpeter 1955). Table 3 indicates whether each magnetar's search is considered 'partially or fully complete' ( $\checkmark$ ) or 'incomplete' ( $\times$ ) in the above analysis. We conclude that our search for companion stars and SNRs is reasonably sensitive along sightlines with typical extinction and distances  $< 10 \text{ pc}$ .

## 6.2 The Magnetar Binary and Massive Star Merger Fractions

### 6.2.1 Markov-Chain Monte Carlo Analysis of Magnetar Binary Fractions

With more well defined estimates of our search completeness, we next determine the implications of our results on the CCSN model. We adapt the method of Kochanek (2023) to constrain the binary parameters of the magnetar progenitor population using a Markov-Chain Monte Carlo (MCMC) simulation. Uniform priors are chosen to estimate the fraction of systems which were not binaries at death,  $f_n$ ; the fraction that were unbound at death,  $f_u$ ; and the fraction of interacting binaries remaining bound after the CCSN,  $f_b$ , and the fraction of non-interacting binaries remaining bound after the CCSN,  $f_p$ , by  $f_n = 1 - f_u - f_b$  and  $f_b = f_i + f_p$ .

The likelihood is the joint multinomial probability of the observed samples; we define the sample for this analysis incorporating the completeness ratios in Table 3. Of the 31 magnetars and candidates, three systems, CXOU J164710.2-455216, 3XMM J185246.6+003317, and SGR J1822.3-1606, were proposed as unbound binary systems. The

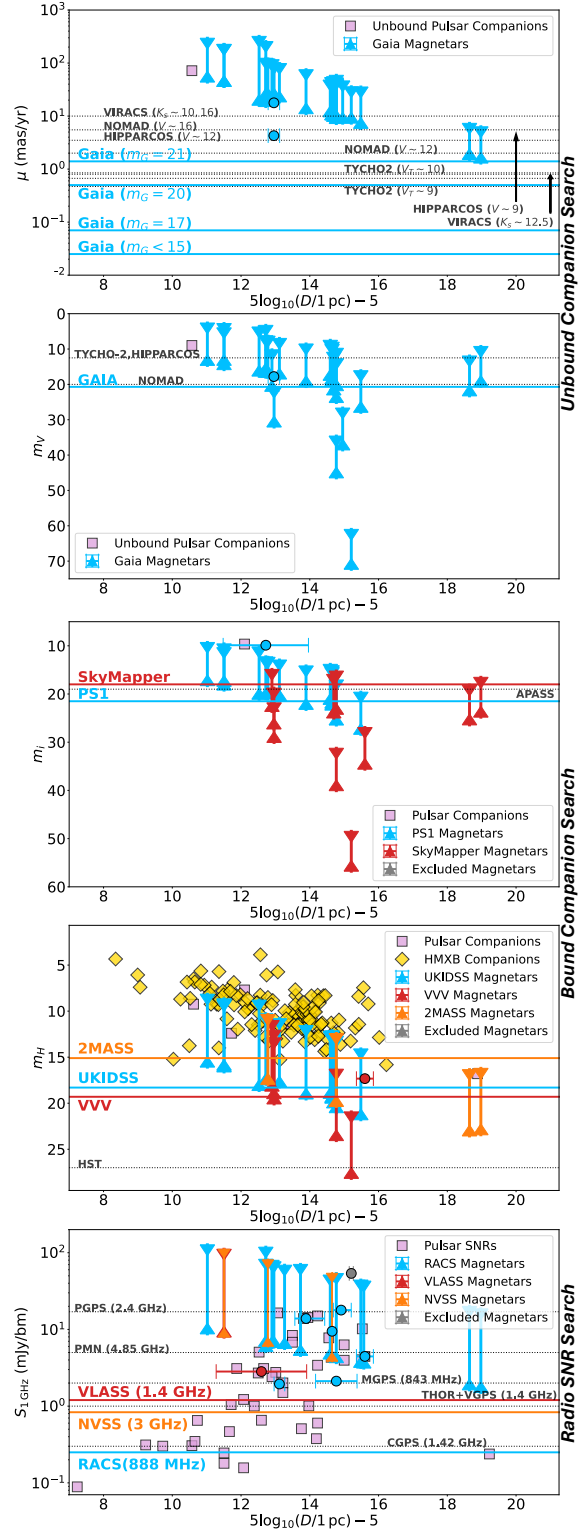


**Figure 6.** Completeness plots versus distance modulus for (rows 1 and 2) the *Gaia* search, (row 3) the optical and (row 4) IR searches, and (row 5) the radio search. Circular, square, and diamond markers with errorbars indicate known companions or remnants of magnetars, pulsars, and HMXBs, respectively. Proper motion, apparent magnitude, and 1 GHz flux ranges, are shown as vertical lines, with color relating to the survey used for the search. The sensitivity limits of each survey are indicated by horizontal lines. We expect most magnetars with SNR shells or stellar companions would have been detected if present. Sensitivity limits for past searches are shown as black dotted lines for comparison (see Appendix E for references).

**Table 3.** Search Results and Completeness Ratios

Magnetar	SNR Candidate	Radio SNR Complete?	Bound Companion Candidate	Optical/IR Bound Complete?	Unbound Companion Candidate	<i>Gaia</i> Unbound Complete?	Prior Association Candidate(s)
CXOU J0100	<i>None</i>	✓(R)	<i>None</i>	✓(S,T)	–	✓	–
4U 0142	<i>None</i>	✓(N)	<i>None</i>	✓(P,T)	<i>None</i>	✓	–
SGR 0418	<i>None</i>	✓(N)	<i>None</i>	✓(P,U)	<i>None</i>	✓	–
SGR 0501	<i>None</i>	✓(V)	<i>None</i>	✓(P,U)	<i>None</i>	✓	HBH 9 (1)
SGR 0526	N49 [ $p < 0.1\%$ ]	✓(R)	<i>None</i>	✗(S,U)	<i>None</i>	✓	N49 (2)
1E 1048	<i>None</i>	✓(R)	<i>None</i>	✓(S,T)	<i>None</i>	✓	–
1E 1547	G327.2-00.1 [ $p < 0.1\%$ ]	✓(R)	<i>None</i>	✓(S,V)	–	✗	G327.2-00.1 (3)
PSR J1622	G333.9+00.0 [ $p < 0.1\%$ ]	✓(R)	<i>SMSS J162244.99-495055.7</i> [ $p < 0.1\%$ ]	✓(S,V)	–	✗	G333.9+00.0 (4)
SGR 1627	<i>None</i>	✓(R)	<i>None</i>	✗(S,V)	–	✗	G337.0-00.1 (5)
CXOU J1647	<i>None</i>	✓(R)	<i>None</i>	✓(S,V)	<i>None</i>	✓	WR 77F (6)
IRXS J1708	<i>None</i>	✓(R)	<i>None</i>	✓(S,V)	<i>None</i>	✓	–
CXOU J1714	CTB 37B [ $p < 0.1\%$ ]	✓(R)	<i>None</i>	✓(S,V)	<i>None</i>	✗	[CTB 37B, VIRAC 384090103 (7,8)]
SGR J1745	{ <i>0FGL J1746.0-2900</i> [ $p < 0.1\%$ ] <i>GC Bipolar Radio Lobes</i> [ $p < 0.1\%$ ] <i>NNM2015</i> [ $p < 0.1\%$ ]}]	✓(R)	<i>None</i>	✓(P,V)	<i>None</i>	✓	GC Bipolar Radio Lobes (13,14)
SGR 1806	<i>Fermi J1808.2-2029</i> [ $p < 0.1\%$ ]	✓(R)	<i>None</i>	✓(S,V)	<i>None</i>	✓	[G10.0-0.3 (9) Fermi J1808.2-2029 (21)]
XTE J1810	<i>None</i>	✓(R)	<i>None</i>	✓(P,U)	<i>None</i>	✓	–
Swift 1818	<i>None</i>	✓(R)	<i>None</i>	✓(P,U)	<i>None</i>	✓	–
Swift J1822	<i>None</i>	✓(R)	{ <i>2MASS J18221794-1604259</i> [ $p < 0.1\%$ ] <i>2MASS J18221839-1604241</i> [ $p < 0.1\%$ ]}]	✓(P,U)	GDR3 409783245895594880 [ $p < 0.1\%$ ]	✓	–
SGR 1833	<i>None</i>	–(R)	<i>None</i>	–(P,T)	<i>None</i>	–	–
Swift J1834	W41 [ $p < 0.1\%$ ]	✓(R)	<i>None</i>	✓(P,U)	<i>None</i>	✓	W41 (10)
1E 1841-045	4C-04.71 [ $p < 0.1\%$ ]	✓(R)	<i>None</i>	✓(P,U)	<i>None</i>	✓	4C-04.71 (11)
3XMM J1852	Kes 79 [ $p < 0.1\%$ ]	✓(R)	<i>None</i>	✓(P,U)	{ <i>DR3 4266311617807818624</i> [ $p = 1.08\%$ ], <i>DR3 4266313683745630080</i> [ $p < 1.0\%$ ], <i>DR3 4266315504811807488</i> [ $p < 1.0\%$ ], <i>DR3 4258978601120897664</i> [ $p < 1.0\%$ ], <i>CXOU J185238.6+004020*</i> [ $p = 0.02\%$ ]}]	✓	Kes 79 (17)
SGR 1900	<i>S24-RACS J190707+091737</i> [ $p < 0.1\%$ ]	✓(R)	<i>None</i>	✓(P,U)	<i>None</i>	✓	G042.8+00.6 (12)
SGR 1935	G057.2+00.8 [ $p < 0.1\%$ ]	✓(R)	<i>None</i>	✓(P,U)	<i>None</i>	✓	G057.2+00.8 (13)
1E 2259	CTB 109 [ $p < 0.1\%$ ]	✓(V)	<i>None</i>	✓(P,U)	<i>None</i>	✓	G109.1-01.0 (14)
SGR 0755	{ <i>S24-RACS J075552-293709</i> [ $p < 0.1\%$ ] <i>S24-RACS J230208+585020</i> [ $p < 0.1\%$ ] <i>S24-RACS J075520-293531</i> [ $p < 0.1\%$ ] <i>S24-RACS J075523-292928</i> [ $p < 0.1\%$ ] <i>S24-RACS J075603-292541</i> [ $p < 0.1\%$ ] <i>S24-RACS J075613-293630</i> [ $p < 0.1\%$ ] <i>NVSS J075522-293937</i> [ $p < 0.1\%$ ] <i>NVSS J075529-294201</i> [ $p < 0.1\%$ ]} [W28 [ $p < 0.1\%$ ]]]	✓(R)	{ <i>PSO J118.9270-29.5649</i> [ $p < 0.1\%$ ] <i>2MASS J07554248-2933535</i> [ $p < 0.1\%$ ] <i>PSO J118.9228-29.5694</i> [ $p = 2.0\%$ ] <i>PSO J118.9189-29.5686</i> [ $p = 4.0\%$ ] <i>2MASS J07554146-2934098</i> [ $p < 0.1\%$ ] <i>2MASS J07554053-2934071</i> [ $p < 0.1\%$ ] <i>2MASS J07554295-2934093</i> [ $p = 2.0\%$ ] <i>2MASS J07554149-2933368</i> [ $p < 0.1\%$ ]}]	✓(P,T)	<i>None</i>	✓	CPD-29 2176 (8)
SGR 1801	{ <i>18 sources</i> <sup>‡</sup> [ $p < 0.1\%$ ]] [G009.7-00.0 [ $p < 0.1\%$ ]]]	–(R)	<i>None</i>	–(P,U)	<i>None</i>	–	W28 (20)
SGR 1808	<i>S24-RACS J180842-202849</i> [ $p < 0.1\%$ ] [ <i>28 sources</i> <sup>‡</sup> [ $p < 0.1\%$ ]]]	–(R)	<i>None</i>	–(P,U)	<i>None</i>	–	–
AX J1818.8-1559	<i>None</i>	–(R)	<i>None</i>	–(P,U)	<i>None</i>	–	–
AX J1845-0258	G029.6+00.1 [ $p < 0.1\%$ ]	✓(R)	<i>None</i>	✓(P,U)	<i>None</i>	✓	G029.6+00.1 (15)
SGR 2013+34	<i>None</i>	✓(N)	<i>None</i>	✓(P,U)	<i>None</i>	✓	–
PSR J1846-0258	Kes 75 [ $p < 0.1\%$ ]	✓(R)	<i>None</i>	✓(P,U)	<i>None</i>	✓	Kes 75 (16)

For each magnetar (written with its abbreviated name), the SNR candidates, bound companion candidates, and unbound companion candidates with  $p < 5\%$  are given, with  $p$ -values in brackets. Candidates suspected to be false positives are given in italics. Sources identified ‘by-eye’ which are not confidently associated with any known object are labelled using the format, ‘S24-survey-Jhhmmss±ddmmss’, where *survey* is the survey used and the italicized portion is the J2000 RA and declination of the centroid. For each search, the completeness along each magnetar’s sightline is indicated by a ✓, meaning the search is either partially or fully sensitive to stars or remnants, or by an ✗, meaning that even the brightest expected stars or remnants would not be detectable. The radio search completeness is labelled with ‘R’, ‘V’, or ‘N’ to indicate whether the RACS, VLASS, or NVSS survey is used. The optical/IR bound search is considered partially or fully complete if either the optical or IR search are complete. These are labelled with ‘P’ or ‘S’, to indicate whether the PS1 or SkyMapper survey is used, and ‘T’, ‘U’, or ‘V’ to indicate whether the 2MASS, PS1, or VVV survey is used. The *Gaia* search is considered partially or fully complete if both the  $V$ -band magnitude and expected relative proper motion are detectable. Four magnetars or candidates have no distance measures and the completeness cannot be determined; these are marked with ‘–’. Candidates for SNR, bound, or unbound companions from previous analyses are provided in the last column with references matched to the following: (1) Gaensler & Chatterjee (2008) (2) Klose et al. (2004) (3) Gelfand & Gaensler (2007) (4) Anderson et al. (2012a) (5) Corbel et al. (1999) (6) Clark et al. (2014) (7) Halpern & Gotthelf (2010a) (8) Chrimmes et al. (2022b) (9) Corbel & Eikenberry (2004) (10) Kargaltsev et al. (2012) (11) Vasishth & Gotthelf (1997) (12) Vrba et al. (2000) (13) Gaensler (2014) (14) Fahlman & Gregory (1981) (15) Gaensler et al. (1999b) (16) Gotthelf et al. (2000) (17) Zhou et al. (2014) (18) Ponti et al. (2015) (19) Yalinewich et al. (2017) (20) Cline et al. (2000) (21) H. E. S. S. Collaboration et al. (2018)

<sup>†</sup>For the *Gaia* search for unbound companions, we consider the proper motion sensitivity in four magnitude bins as described in Collaboration et al. (2022):  $m_G > 15$  ( $\mu_{\min} = 0.025 \text{ mas yr}^{-1}$ ),  $m_G = 17$  ( $\mu_{\min} = 0.07 \text{ mas yr}^{-1}$ ),  $m_G = 20$  ( $\mu_{\min} = 0.5 \text{ mas yr}^{-1}$ ), and  $m_G = 21$  ( $\mu_{\min} = 1.4 \text{ mas yr}^{-1}$ ).

<sup>‡</sup>For conciseness, we omit the names of the 17 and 28 false positives found for SGR 1801-23 and SGR 1808-20, respectively. For the former, the false positives are rejected in favor of W28 identified by Cline et al. (2000). Detailed discussion for the latter is provided in Section 5.3.

\*CXOU J185238.6+004020 is an X-ray pulsar associated with Kes 79. We explore the scenario that the progenitors of 3XMM J1852 and this pulsar were bound in Section 5.3.

candidate companion of CXOU J171405.7-381031 from Chrimmes et al. (2022b) is unconfirmed based on the optical and IR search results. For the purpose of our analysis, we will accept SGR 0755-2933 and CPD-29 2176 as a bound interacting binary system based on the results of Richardson et al. (2023). Of the remaining sample, three magnetars are constrained to be not currently bound, two are constrained not to have unbound companions, and the remaining 21 are considered not to be binaries at the time of the CCSN. With this, the likelihood can be written as:

$$\mathcal{P}_i = f_n^{21} f_u^3 f_i^1 (1 - f_u)^2 (f_n + f_u)^3 \quad (7)$$

where  $(1 - f_u)$  is the fraction that are not unbound systems and

$(f_n + f_u)$  is the fraction that are not bound systems. The sampled posteriors are used to estimate the median values and 90% confidence intervals for  $f_n$ ,  $f_u$ , and  $f_i$ .

In keeping with the notation of Kochanek (2023), we define the case above as ‘SNR incomplete’, where we assume that all magnetars in the sample originate in CCSNe. While this is likely the primary formation channel, it is possible that other processes may form magnetars at lower rates. Considering this, we define the ‘SNR complete’ case, in which magnetars without confirmed or proposed SNR associations are not formed via CCSNe, and therefore do not contribute to the binary fractions above. In this case, the likelihood becomes:

$$\mathcal{P}_c = f_n^{10} f_u^1 f_{nc}^{15} (f_n + f_u)^2 (1 - f_u)^2 (1 - f_{nc})^1 \quad (8)$$

where  $f_{nc}$  is the fraction of magnetars which do not originate in CCSNe. This modifies the definition for  $f_n$  to  $f_n = 1 - f_u - f_b - f_{nc}$ . Note this case is more restrictive, as SGR 0755+2933, SGR J1822.3-1606, and 13 other magnetars for which the radio search is  $> 75\%$  complete have no confirmed SNR in this or any other work. A final case, ‘SNR/unbound complete’ is defined if we also take unbound magnetar binaries as evidence of CCSNe; in this case, we include CXOU J164710.2-455216, SGR J1822.3-1606, and 3XMM J185246.6+003317 as unbound systems, and the likelihood becomes:

$$\mathcal{P}_{uc} = f_n^{10} f_u^3 f_{nc}^{13} (f_n + f_u)^2 (1 - f_u)^2 (1 - f_{nc})^1 \quad (9)$$

Results for the three cases are summarized in Table 4. In the ‘SNR incomplete’ case, we find a median bound binary fraction  $f_b \approx 9_{-4}^{+6}\%$ , and unbound binary fraction  $f_u \approx 12_{-5}^{+6}\%$ , where the errors are  $1\sigma$  uncertainties. While the bound fraction is marginally consistent with the predictions from [Chrimes et al. \(2022b\)](#), [Kochanek et al. \(2019\)](#), and [Renzo et al. \(2019\)](#) population synthesis results, the unbound fraction significantly disagrees with their prediction of  $f_u \sim 38 - 56\%$ . Furthermore, we find that a median of only  $1 - f_n \approx 22_{-7}^{+8}\%$  of magnetars were binaries at death, which disagrees with the estimate of  $\sim 50 - 60\%$  from population synthesis with 90% confidence.

In the ‘SNR complete’ case, we estimate a median unbound fraction  $f_u \approx 3_{-2}^{+3}\%$ , and a 90% upper limit on the bound fraction of  $f_b \lesssim 12\%$ , the former of which also disagrees with the [Chrimes et al. \(2022b\)](#), [Kochanek et al. \(2019\)](#), and [Renzo et al. \(2019\)](#) population synthesis estimates. We find a median  $1 - f_n \approx 63_{-8}^{+9}\%$  of magnetars undergo CCSNe while in binaries, which more closely agrees with population synthesis than the ‘SNR incomplete’ case. Most significantly, we constrain the fraction of magnetars formed by channels other than CCSNe to  $f_{nc} \approx 53_{-10}^{+8}\%$ , with a 90% confidence interval from 37 – 66%. This would contradict the view that CCSNe are the dominant formation pathway (e.g. [Schneider et al. 2019](#); [White et al. 2022](#); [Keane & Kramer 2008](#)). Furthermore, no magnetars have been confirmed to form from non-CCSN channels.

A similar result is obtained in the ‘SNR/unbound complete’ case; notably, the larger unbound fraction  $f_u \approx 8_{-3}^{+5}\%$  allows a lower non-CCSN fraction  $f_{nc} \approx 46 \pm 9\%$ , while the fraction of magnetars from binaries  $1 - f_n \approx 61 \pm 9\%$  still agrees with population synthesis results. While the ‘SNR/unbound complete’ and ‘SNR complete’ cases do not differ in their underlying assumptions about alternate formation channels, it demonstrates that the detection of unbound magnetar binaries allows for tighter constraints to be placed on  $f_{nc}$ . Furthermore, these cases motivate discussion of alternate formation channels, such as Accretion Induced Collapse (AIC) of magnetized White Dwarfs or binary Neutron Star mergers, to which we return in Section 6.3 ([Ruiter et al. 2019](#); [Fryer et al. 1999](#); [Giacomazzo & Perna 2013](#); [Giacomazzo et al. 2015](#)).

### 6.2.2 Implications for Massive OB Star Binary and Merger Fractions

Many models of magnetar formation attribute their strong magnetic fields to a dynamo process driven by accretion from ablated stellar companions (e.g. [Popov 2020](#); [Revnivtsev & Mereghetti 2016](#); [Fuller & Lu 2022](#), and references therein). The low  $f_b$  and  $f_u$  fractions in Table 4 may indicate that other magnetic field growth mechanisms are more common, such as the merger of massive stars. In this scenario, the magnetic field of the primary star is first amplified up to  $\lesssim 10^8$  G through accretion before further amplification through merger of the

cores, producing a highly magnetized massive star such as  $\tau$  Sco and the Wolf-Rayet star in the HD 45166 binary ([Schneider et al. 2019](#); [Shenar et al. 2023](#)). If magnetic flux is conserved during the CCSN event, a neutron star remnant with a magnetar-like surface magnetic field ( $\sim 10^{14}$  G) could be achieved (e.g. [Popov 2020](#); [Schneider et al. 2019](#); [Obergaullinger et al. 2014](#), and references therein). A high frequency of such pre-CCSN mergers could potentially explain the lack of magnetars with bound or unbound companions.

The fraction of massive stellar binaries that merge prior to CCSNe,  $f_m$ , can be inferred by assuming an initial massive star companion fraction  $F_0 \approx 84 \pm 9\%$ , derived in [Moe & Di Stefano \(2017\)](#), for early B-type stars.<sup>41</sup> While some simulations suggest that CCSNe can form from mergers of intermediate mass stars ( $5 - 8M_\odot$ ), we focus this discussion on binaries where both stars are  $> 7.5M_\odot$  (e.g. [Zapartas et al. 2017](#)). Relating the initial companion fraction to the fraction of systems in binaries at death:

$$\frac{f_u + f_b}{1 - (f_b + f_u)f_q} = F_0(1 - f_m) \quad (10)$$

where  $f_q = 0.426$  is the fraction of binaries with a secondary star less massive than the primary<sup>42</sup>.  $f_q$  effectively estimates the fraction of CCSNe from explosions of the secondary star, which are excluded from this analysis since we consider CCSN of stars with *stellar* companions<sup>43</sup> (see [Kochanek 2009](#); [Kochanek et al. 2019](#); [Kobulnicky & Fryer 2007](#), for detailed discussions). If we adopt  $f_b$  and  $f_u$  from Table 4 and use a Gaussian distribution<sup>44</sup> for  $F_0$ , we obtain median values  $f_m \approx 70_{-12}^{+10}\%$  for the ‘SNR complete’ case,  $f_m \approx 88_{-8}^{+5}\%$  for the ‘SNR incomplete’ case, and  $f_m \approx 82_{-9}^{+7}\%$  for the ‘SNR/unbound complete’ case. In all three cases,  $f_m$  is significantly higher than the merger fractions estimated for neutron star progenitors in population synthesis from [Kochanek et al. \(2019\)](#) ( $\sim 48\%$ ) and [Renzo et al. \(2019\)](#) ( $\sim 22_{-9}^{+26}\%$ ). It is also possible that magnetar progenitors have an above average merger rate compared to other neutron star species. Corner plots summarizing this analysis are shown in the left-hand plot of Figure 7.

The ‘SNR incomplete’ case does not allow for alternate formation channels, suggesting instead that a large fraction  $f_n \approx 80\%$  were formed from single stars. For a fixed binary fraction  $F_0$ , this requires an inflated merger rate  $f_m \approx 75\%$ . The ‘SNR/unbound complete’ case is one step removed, taking unbound companions as evidence of a disruption event (CCSN) but also allowing for  $f_{nc} \approx 45\%$  to form from other formation channels (e.g. AIC, neutron star merger). For this reason,  $f_n \approx 40\%$  is lowered, but the unbound fraction  $f_u \approx 10\%$  is relatively unchanged and the merger rate  $f_m \approx 80\%$  increases only

<sup>41</sup> Note that this fraction includes binary, tertiary, and higher order systems with primary early B-type stars ( $9M_\odot < M_* < 16M_\odot$ ), but we will collectively refer to them as ‘binaries’ ([Moe & Di Stefano 2017](#)). Any higher order system can lead to a compact remnant with bound or unbound companion stars, regardless of multiplicity.

<sup>42</sup> This is derived by integrating a Salpeter-like ( $\alpha = -2.35$ ) initial mass function (IMF; [Salpeter 1955](#); [Moe & Di Stefano 2017](#)); see Section 1 and Equation 1 of [Kochanek et al. \(2019\)](#), and references therein. Note that in [Kochanek et al. \(2019\)](#) Equation 1,  $f_b$  is defined as the fraction of CCSNe that occur in stellar binaries, whereas we here define  $f_b$  as the fraction of systems for which the binary remains bound following the CCSN.

<sup>43</sup> We assume that magnetar 3XMM J185246.6+003317 was formed from the first explosion, as is implied from our analysis in Section 4.

<sup>44</sup> More rigorously,  $F_0$  follows a binomial distribution, but we find this makes little difference to the results. The Gaussian method is adopted to more easily incorporate the uncertainty on  $F_0$ .

**Table 4.** Constraints on magnetar binaries from this work

Sub-Sample <sup>†</sup>	Symbol	SNR incomplete		SNR complete		SNR/unbound complete	
		Median	90% Confidence	Median	90% Confidence	Median	90% Confidence
<b>Not binary at death</b>	$f_n$	$78^{+7}_{-8}\%$	64 – 88%	$37^{+9}_{-8}\%$	24 – 52%	$39 \pm 9\%$	25 – 54%
<b>Bound binary</b>	$f_b$	$9^{+6}_{-4}\%$	3 – 20%	–	< 12%	–	< 13%
<i>Interacting binary</i>	$f_i$	$6^{+5}_{-3}\%$	1 – 15%	–	< 8%	–	< 8%
<i>Non-interacting binary</i>	$f_p$	–	< 8%	–	< 7%	–	< 7%
<b>Unbound binary</b>	$f_u$	$12^{+6}_{-5}\%$	5 – 24%	$3^{+3}_{-2}\%$	1 – 10%	$8^{+5}_{-3}\%$	3 – 16%
<b>Not CCSN Progenitor</b>	$f_{nc}$	–	–	$53^{+8}_{-10}\%$	37 – 66%	$46 \pm 9\%$	31 – 60%
Pre-CCSN Merger <sup>‡</sup>	$f_m$	$70^{+10}_{-12}\%$	48 – 86%	$88^{+5}_{-8}\%$	73 – 96%	$82^{+7}_{-9}\%$	65 – 92%

*Note:* We define two broad cases based on the completeness of the RACS SNR search: ‘SNR incomplete’ assumes that all magnetars originate in CCSNe, whether one is detected or not. ‘SNR complete’ assumes that magnetars with RACS search completeness ratios > 75% which had no SNR detected did not form through CCSNe. We also consider the ‘SNR/unbound complete’ case in which unbound magnetar binaries are evidence of the CCSN progenitor channel as well. Median values are reported with  $1\sigma$  errors.

<sup>†</sup>  $f_n$ ,  $f_b$ ,  $f_u$ , and  $f_{nc}$  are defined such that  $f_n + f_b + f_u = 1$  in the ‘SNR incomplete’ case, and  $f_n + f_b + f_u + f_{nc} = 1$  in the ‘SNR complete’ and ‘SNR/unbound complete’ cases.  $f_i$  and  $f_p$  sum to the total binary fraction  $f_p + f_i = f_b$ . The merger rate  $f_m$  is the fraction of binary stars that merge, while the other fractions are taken out of the total number of CCSNe.

<sup>‡</sup>  $f_m$  is estimated assuming the progenitor stars are early B-type stars ( $9M_\odot < M_* < 16M_\odot$ ) with binary fraction  $F_0 = 84 \pm 9\%$  (Moe & Di Stefano 2017).

marginally ( $< 1\sigma$  change). The ‘SNR complete’ case, however, excludes both SGR 1822.3-1606 and CXOU J164710.2-455216, which do not have SNR detections, from the unbound sample. SGR 0755-2933, the only proposed bound system, is excluded for the same reason. Therefore, both the merger fraction  $f_m \approx 90\%$  and the fraction from alternate channels  $f_{nc} \approx 55\%$  increase to accommodate the lowered unbound fraction  $f_u \approx 5\%$ . In all three cases, the merger fraction  $f_m$  is larger than expected, requiring us to reconsider the conditions that lead to massive OB star mergers. However, a more strict interpretation (‘complete’ cases) is consistent with  $f_{nc} \approx 31 - 66\%$  forming from alternate channels.

Alternatively, we can allow both  $F_0$  and  $f_m$  to vary, leaving the progenitor mass and stellar type unconstrained. Under this assumption, the right-hand plot of Figure 7 shows the 90% confidence regions for  $F_0$  and  $f_m$  in each case. This demonstrates that a wider range of merger rates can be tolerated if magnetars can form from the mergers of less massive stars (Moe & Di Stefano 2017). This would marginally support the analysis of Zapartas et al. (2017), which identified a population of CCSNe from the mergers of intermediate mass stars ( $5 - 7.5M_\odot$ ). However, a reliable comparison requires a broader search that targets both massive and intermediate mass stars, which we leave to future work. Figure 7 summarizes the results of this analysis in a flowchart showing the evolution of stellar progenitors to magnetar remnants.

### 6.2.3 Limitations in Comparison to Population Synthesis Results

While we compare our resulting binary, merger, and CCSN fractions to population synthesis simulations, a discussion of the limitations of such analysis is warranted. We focus this discussion on the Chrimes et al. (2022b) simulations, though similar comparisons can be made with the Kochanek et al. (2019) and Renzo et al. (2019) simulations. Chrimes et al. (2022b) utilized Binary Population and Spectral Synthesis (BPASS) models and imposed constraints on the total mass ( $> 2.0M_\odot$ ), CO core mass ( $> 1.38M_\odot$ ), and remnant mass ( $1.38 < M_{\text{rem}} < 3.0$ ) to identify stellar models that evolve into magnetars. One potential source of error is the Initial Mass Function (IMF), for which Chrimes et al. (2022b) use the two-component Kroupa et al. (1993) broken power law model with index  $\alpha = -1.30$  for masses  $0.1 - 0.5M_\odot$  and  $\alpha = -2.35$  for

masses  $0.5 - 300M_\odot$ . Alternatively, some analyses have proposed a smoothly varying IMF with a mass-dependent  $\alpha$  which is steeper for high mass stars (e.g. Kroupa 2002; Kroupa & Weidner 2003; Miller & Scalo 1979; Chabrier 2001; Weidner & Kroupa 2005). This could lead to a larger ratio of low mass to high mass stars. The relationship of the IMF to the binary fraction also has a complex dependency on the mass-ratio ( $M_2/M_1$ ) distribution. While a uniform distribution is assumed to compute  $f_q \approx 0.426$  (e.g. Kochanek 2018; Kochanek et al. 2019; Kouwenhoven et al. 2005), Renzo et al. (2019) find that a negative power law distribution results in a larger merger fraction  $f_m$ . This demonstrates that both the IMF and mass ratio distribution can have a significant impact on the massive star binary fraction, and motivates detailed consideration in future studies.

An additional caveat is that relatively loose constraints were used to gather the magnetar sample for this work in comparison to previous analyses. For example, Chrimes et al. (2022b) excludes magnetars in Magellanic Clouds, as well as those without distance estimates, imaging data, or photometric data. With the small 31-magnetar sample, we have chosen not to place arbitrary limits beyond the completeness constraints discussed in Section 6.1. The reported p-values provide quantitative measures of confidence that incorporate large distances, errors, and accuracy of imaging data. Furthermore, the irregularity of transient magnetar outbursts could have marginal effects on our analysis; for example, both SGR 1935+2154 and PSR J1846-0258 have recently entered X-ray outburst phases which may tighten constraints on their ages (Ibrahim et al. 2024; Laha et al. 2020; Krimm et al. 2020; Sathyaprakash et al. 2024). SGR 0755-2933 and SGR 1808-20, contrarily have only one burst detection, each (Lamb et al. 2003; Barthelmy et al. 2016). Future tests may benefit from partitioning the sample based on their distance, proper motion, extinction properties, or outburst phase to characterize its effect on the search.

### 6.3 Alternate Magnetar Formation Channels

In this section, we consider the implications of the ‘SNR complete’ and ‘SNR/unbound complete’ cases which require large contributions  $f_{nc} \sim 45 - 55\%$  from non-CCSN formation channels. First, consider how this alters the birth rate assumptions for the neutron star population. Keane & Kramer (2008) predicted that the Galactic CCSN rate ( $1.9 \pm 1.1 \text{ century}^{-1}$ ) is too low to source the ob-

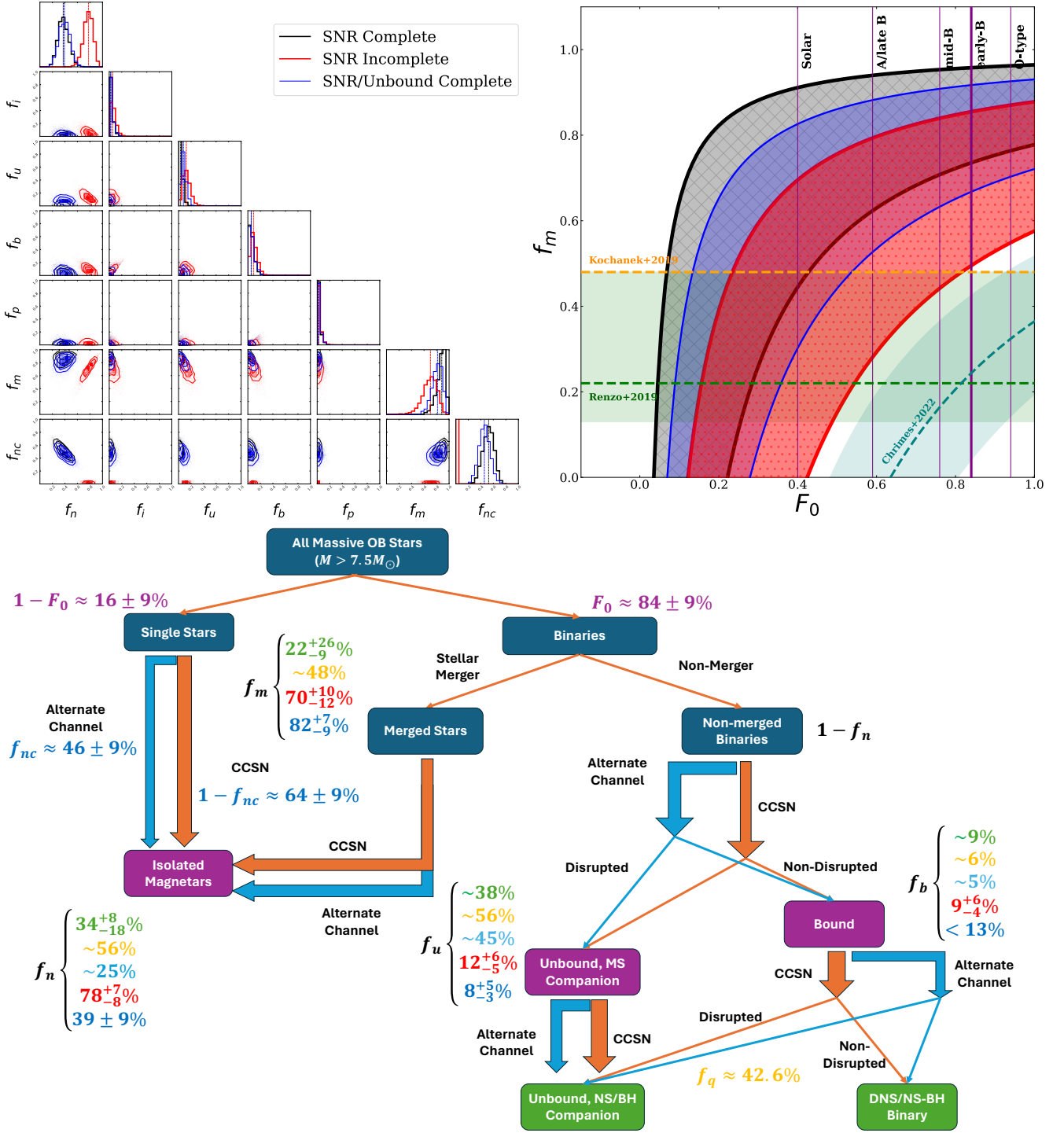


**Figure 7.** (Upper Left:) Corner Plots from the Magnetar Binary Fraction Simulation in Section 6.2. The ‘SNR complete’, ‘SNR incomplete’, and ‘SNR/unbound complete’ cases as defined in Section 6 and Table 4 are shown in black, red, and blue, respectively. Vertical lines indicate the median values from Table 4 in each case. The ‘SNR complete’ and ‘SNR/unbound complete’ cases would suggest that  $f_{nc} \approx 45 - 55\%$  of magnetars to descend from non-CCSN channels, whereas the ‘SNR incomplete’ case suggests a higher stellar merger rate  $f_m \approx 70\%$  among OB stars is sufficient to produce the observed sample. The merger rates displayed assume a massive star binary fraction  $F_0 = 84 \pm 9\%$  (Moe & Di Stefano 2017). (Upper Right:) 90% Confidence Regions for the merger fraction  $f_m$  and OB star binary fraction  $F_0$ . The colors for each region correspond to the cases in the contour plot, and vertical purple lines show  $F_0$  predicted for different stellar types through population synthesis (Moe & Di Stefano 2017). The green and yellow dashed lines indicate the median merger fractions from Renzo et al. (2019) and Kochanek et al. (2019); the teal dashed line indicates the  $f_m$  vs.  $F_0$  curve inferred from  $f_b$  and  $f_u$  in Chrimes et al. (2022b). The green and teal shaded regions indicate the  $1\sigma$  errors for the Renzo et al. (2019) and Chrimes et al. (2022b) cases. Each of these appear to underestimate the true fraction for early B-type stars. (Bottom:) Flowchart showing the progression of massive stars into magnetars with constraints from population synthesis and observations in this work. CCSNe are indicated by orange arrows while alternate formation channels are indicated by blue arrows. Constraints on  $f_m, f_n, f_u, f_b$ , and  $F_0$  (see Section 3.3) are shown from simulations by Moe & Di Stefano (2017, purple), Renzo et al. (2019, green), Kochanek et al. (2019, yellow), and Chrimes et al. (2022b, teal). Observational constraints from this work are shown in red for the ‘SNR incomplete’ case and blue for the ‘SNR/unbound complete’ case. A lower binary fraction would allow for a lower merger fraction for magnetar progenitors, but would require lower mass progenitors.

served population of magnetars, pulsars, XDINS, and RRATs (total  $10.8^{+7.0}_{-5.0}$  century $^{-1}$ ). If we incorporate the results of the ‘SNR complete’ and ‘SNR/unbound complete’ cases, which predict  $f_{nc} \approx 55\%$  and  $f_{nc} \approx 45\%$  of magnetars are formed by alternate channels, respectively, then the total neutron star birth rate from CCSNe is decreased to  $\sim 5$  century $^{-1}$  and  $\sim 6$  century $^{-1}$ . This is still inconsistent with the CCSN rate, and suggests that alternate channels are unlikely to wholly explain the observed binary fractions.

It is possible that alternate formation channels are partially responsible for our observations. One such channel is Accretion Induced Collapse (AIC), in which ONe White Dwarfs accrete from Helium burning giant companions before collapsing (e.g., [Ruiter et al. 2019](#); [Fryer et al. 1999](#)). Following AIC, either a bound neutron star-white dwarf binary is formed, or the donor star is ejected as a runaway. While the ejected mass from AIC is expected to be lower than that of a CCSN ( $\sim 10^{-3} - 0.05M_{\odot}$ ), low mass white dwarf companions would require less energy to become unbound than massive stars ([Ruiter et al. 2019](#); [El-Badry et al. 2023](#); [Shen et al. 2018](#)).

Direct evidence for AIC has not yet been observed, making them unlikely to make up the required  $f_{nc} \sim 45 - 55\%$ ; however, [Sharma et al. \(2023\)](#) observed that long delay times and high-mass host galaxies for two Fast Radio Bursts (FRBs) support origins from neutron stars or magnetars formed through AIC (see also [Woodland et al. 2023](#); [Gordon et al. 2023b](#), for comparisons off FRB offset and host galaxy flux distributions to CCSNe). More unique formation processes such as neutron star mergers require gravitational wave detection and followup, but are unlikely to supercede CCSNe in magnetar production (e.g. [Giacomazzo & Perna 2013](#); [Giacomazzo et al. 2015](#)). Therefore, the results of this search continue to support CCSNe as the most common magnetar formation channel, and we expect future improvements on radio survey sensitivity to recover the remaining SNRs.

## 7 CONCLUSION

In this work, we have searched optical, IR, and radio image and point source catalogs for evidence of CCSNe and massive OB stars associated with magnetars. Out of the 31 known magnetars and candidates, we identify two candidates for unbound magnetar binaries at  $> 95\%$  confidence: a massive OB star in association with SGR 1822.3-1606, and an X-ray pulsar in association with 3XMM J185246.6+003317. We also recover the proposed Be star companion of SGR 0755-2933 and marginally detect the proposed unbound companion of CXOU J164710.2-455216. Through the radio search we recover nine out of ten confirmed SNR associations and four of five unconfirmed associations; additional SNR candidates for SGR 1808-20 are identified but require a distance and proper motion measurement for the magnetar to confirm. Through an MCMC analysis, we find only  $5 - 24\%$  of magnetars have unbound massive star companions with  $90\%$  confidence. This is much lower than is predicted by population synthesis simulations from [Chrimes et al. \(2022b\)](#), [Kochanek et al. \(2019\)](#), and [Renzo et al. \(2019\)](#).

Our results support a high merger rate for massive OB star progenitors between  $48 - 86\%$ . It is unclear if only magnetars or neutron stars as a whole preferentially form from mergers. While alternate formation channels such as AIC and neutron star mergers may account for a small fraction of magnetars, it is unlikely that they are solely responsible for the lack of observed unbound binaries, as this would require  $\sim 45 - 55\%$  of magnetars to follow such channels and would not entirely solve the neutron star birth rate problem. Incorporating data

from next generation telescopes will significantly improve our search sensitivity to CCSN remnants and unbound stellar companions.

## 8 DATA AVAILABILITY

The data underlying this article, including the magnetar parameters in Tables 1 and Tables 2 as well as derived values and p-values for each optical, IR, and radio source included in the search, are available in machine-readable format in the *CaltechDATA* repository, at <https://doi.org/10.22002/cfj2d-zbc71>.

## 9 ACKNOWLEDGEMENTS

The authors would like to thank the members of the Deep Synoptic Array (DSA-110) team for their support and insight with regards to this search effort. The authors thank staff members of the Owens Valley Radio Observatory and the Caltech radio group, including Kristen Bernasconi, Stephanie Cha-Ramos, Sarah Harnach, Tom Klinefelter, Lori McGraw, Corey Posner, Andres Rizo, Michael Virgin, Scott White, and Thomas Zentmyer. Their tireless efforts were instrumental to the success of the DSA-110. The DSA-110 is supported by the National Science Foundation Mid-Scale Innovations Program in Astronomical Sciences (MSIP) under grant AST-1836018. This material is based upon work supported by the National Science Foundation Graduate Research Fellowship under Grant No. DGE-1745301.

The Pan-STARRS1 Surveys (PS1) and the PS1 public science archive have been made possible through contributions by the Institute for Astronomy, the University of Hawaii, the Pan-STARRS Project Office, the Max-Planck Society and its participating institutes, the Max Planck Institute for Astronomy, Heidelberg and the Max Planck Institute for Extraterrestrial Physics, Garching, The Johns Hopkins University, Durham University, the University of Edinburgh, the Queen’s University Belfast, the Harvard-Smithsonian Center for Astrophysics, the Las Cumbres Observatory Global Telescope Network Incorporated, the National Central University of Taiwan, the Space Telescope Science Institute, the National Aeronautics and Space Administration under Grant No. NNX08AR22G issued through the Planetary Science Division of the NASA Science Mission Directorate, the National Science Foundation Grant No. AST-1238877, the University of Maryland, Eotvos Lorand University (ELTE), the Los Alamos National Laboratory, and the Gordon and Betty Moore Foundation. The UKIDSS project is defined in [Lawrence et al. \(2007b\)](#). The national facility capability for SkyMapper has been funded through ARC LIEF grant LE130100104 from the Australian Research Council, awarded to the University of Sydney, the Australian National University, Swinburne University of Technology, the University of Queensland, the University of Western Australia, the University of Melbourne, Curtin University of Technology, Monash University and the Australian Astronomical Observatory. SkyMapper is owned and operated by The Australian National University’s Research School of Astronomy and Astrophysics. The survey data were processed and provided by the SkyMapper Team at ANU. The SkyMapper node of the All-Sky Virtual Observatory (ASVO) is hosted at the National Computational Infrastructure (NCI). Development and support of the SkyMapper node of the ASVO has been funded in part by Astronomy Australia Limited (AAL) and the Australian Government through the Commonwealth’s Education Investment Fund (EIF) and National Collaborative Research Infrastructure Strategy (NCRIS), particularly the National

eResearch Collaboration Tools and Resources (NeCTAR) and the Australian National Data Service Projects (ANDS).

UKIDSS uses the UKIRT Wide Field Camera (WFCAM; Casali et al. (2007)). The photometric system is described in Hewett et al. (2006), and the calibration is described in Hodgkin et al. (2009). The pipeline processing and science archive are described in Irwin et al. (2004) and Hambly et al. (2008). The VISTA Data Flow System pipeline processing and science archive are described in Irwin et al. (2004), Hambly et al. (2008) and Cross et al. (2012). We have used data from the 5th data release of the Vista Variables in the Via Lactea (VVV) Survey, which is described in detail in Nikzat et al. (2022), and the VVV Infrared Astrometric Catalogue, described in detail in Smith et al. (2018). This publication makes use of data products from the Two Micron All Sky Survey, which is a joint project of the University of Massachusetts and the Infrared Processing and Analysis Center/California Institute of Technology, funded by the National Aeronautics and Space Administration and the National Science Foundation.

This work also uses data obtained from Inyarrimanha Ilgari Bundara / the Murchison Radio-astronomy Observatory. We acknowledge the Wajarri Yamaji People as the Traditional Owners and native title holders of the Observatory site. CSIRO's ASKAP radio telescope is part of the Australia Telescope National Facility (<https://ror.org/05qajvd42>). Operation of ASKAP is funded by the Australian Government with support from the National Collaborative Research Infrastructure Strategy. ASKAP uses the resources of the Pawsey Supercomputing Research Centre. Establishment of ASKAP, Inyarrimanha Ilgari Bundara, the CSIRO Murchison Radio-astronomy Observatory and the Pawsey Supercomputing Research Centre are initiatives of the Australian Government, with support from the Government of Western Australia and the Science and Industry Endowment Fund. This paper includes archived data obtained through the CSIRO ASKAP Science Data Archive, CASDA (<https://data.csiro.au>). This work has utilized data from the LoTSS survey and image archive, which is described in detail in Shimwell et al. (2022). This work has made use of data from the European Space Agency (ESA) mission *Gaia* (<https://www.cosmos.esa.int/gaia>), processed by the *Gaia* Data Processing and Analysis Consortium (DPAC, <https://www.cosmos.esa.int/web/gaia/dpac/consortium>). Funding for the DPAC has been provided by national institutions, in particular the institutions participating in the *Gaia* Multilateral Agreement. This research has made use of the CIRADA cutout service at [cutouts.cirada.ca](http://cutouts.cirada.ca), operated by the Canadian Initiative for Radio Astronomy Data Analysis (CIRADA). CIRADA is funded by a grant from the Canada Foundation for Innovation 2017 Innovation Fund (Project 35999), as well as by the Provinces of Ontario, British Columbia, Alberta, Manitoba and Quebec, in collaboration with the National Research Council of Canada, the US National Radio Astronomy Observatory and Australia's Commonwealth Scientific and Industrial Research Organisation.

## REFERENCES

Acerro F., et al., 2016, *ApJS*, 224, 8  
 Andersen B. C., et al., 2023, *The Astrophysical Journal*, 943, 57  
 Anderson G. E., et al., 2012b, *The Astrophysical Journal*, 751, 53  
 Anderson G. E., et al., 2012a, *ApJ*, 751, 53  
 Anderson L., et al., 2017, *Astronomy & Astrophysics*, 605, A58  
 Andrae R., et al., 2022, arXiv preprint arXiv:2206.06138  
 Archibald R. F., et al., 2013, *Nature*, 497, 591

Arras P., Cumming A., Thompson C., 2004, *The Astrophysical Journal*, 608, L49  
 Avakyan A., Neumann M., Zainab A., Doroshenko V., Wilms J., Santangelo A., 2023, *Astronomy & Astrophysics*, 675, A199  
 Baade W., Zwicky F., 1934, *Proceedings of the National Academy of Sciences*, 20, 254  
 Bailer-Jones C., 2023, *The Astronomical Journal*, 166, 269  
 Bailer-Jones C. A. L., Rybizki J., Fouesneau M., Demleitner M., Andrae R., 2021, *AJ*, 161, 147  
 Barker B. L., Harris C. E., Warren M. L., O'Connor E. P., Couch S. M., 2022, *The Astrophysical Journal*, 934, 67  
 Barker B. L., O'Connor E. P., Couch S. M., 2023, *The Astrophysical Journal Letters*, 944, L2  
 Barthelmy S. D., et al., 2016, *The Astronomer's Telegram*, 8831, 1  
 Bibby J. L., Crowther P. A., Furness J. P., Clark J. S., 2008, *MNRAS*, 386, L23  
 Bihl S., et al., 2016, *A&A*, 588, A97  
 Blaauw A., 1961, *Bulletin of the Astronomical Institutes of the Netherlands*, Vol. 15, p. 265, 15, 265  
 Blumer H., Safi-Harb S., Kothes R., Rogers A., Gotthelf E. V., 2019, *Monthly Notices of the Royal Astronomical Society*, 487, 5019  
 Bogdanov S., 2014, *ApJ*, 790, 94  
 Borkowski K. J., Reynolds S. P., 2017, *The Astrophysical Journal*, 846, 13  
 Bower G. C., et al., 2014, *ApJ*, 780, L2  
 Bower G. C., et al., 2015, *The Astrophysical Journal*, 798, 120  
 Brown A. G., et al., 2021, *Astronomy & Astrophysics*, 649, A1  
 Burns E., et al., 2021, *The Astrophysical Journal Letters*, 907, L28  
 Carretero-Castrillo M., Ribó M., Paredes J., 2023, *Astronomy & Astrophysics*, 679, A109  
 Casali M., et al., 2007, *A&A*, 467, 777  
 Chabrier G., 2001, *The Astrophysical Journal*, 554, 1274  
 Chambers K. C., et al., 2019, *The Pan-STARRS1 Surveys* ([arXiv:1612.05560](https://arxiv.org/abs/1612.05560))  
 Chaty S., Rahoui F., 2012, *The Astrophysical Journal*, 751, 150  
 Chrimes A., Levan A. J., Fruchter A., Groot P., Kouveliotou C., Lyman J., Tanvir N., Wiersema K., 2022a, *Monthly Notices of the Royal Astronomical Society*, 512, 6093  
 Chrimes A., et al., 2022b, *Monthly Notices of the Royal Astronomical Society*, 513, 3550  
 Chrimes A., et al., 2023, *Monthly Notices of the Royal Astronomical Society*, 522, 2029  
 Clark J. S., Ritchie B. W., Najarro F., Langer N., Negueruela I., 2014, *Astronomy & Astrophysics*, 565, A90  
 Cline T. L., et al., 1982, *ApJ*, 255, L45  
 Cline T., Frederiks D. D., Golenetskii S., Hurley K., Kouveliotou C., Mazets E., van Paradijs J., 2000, *ApJ*, 531, 407  
 Collaboration G., et al., 2022, *Gaia Data Release 3: Summary of the content and survey properties* ([arXiv:2208.00211](https://arxiv.org/abs/2208.00211))  
 Condon J., Griffith M. R., Wright A. E., 1993, *Astronomical Journal* (ISSN 0004-6256), vol. 106, no. 3, p. 1095-1100., 106, 1095  
 Condon J. J., Cotton W., Greisen E., Yin Q., Perley R. A., Taylor G., Broderick J., 1998, *The Astronomical Journal*, 115, 1693  
 Corbel S., Eikenberry S. S., 2004, *Astronomy & Astrophysics*, 419, 191  
 Corbel S., Chapuis C., Dame T. M., Durouchoux P., 1999, *ApJ*, 526, L29  
 Cross N. J., et al., 2012, *Astronomy & Astrophysics*, 548, A119  
 Cutri R. M., et al., 2003, *VizieR Online Data Catalog: 2MASS All-Sky Catalog of Point Sources (Cutri+ 2003)*, *VizieR On-line Data Catalog: II/246*. Originally published in: 2003yCat.2246....0C  
 Davies B., Figier D. F., Kudritzki R.-P., Trombley C., Kouveliotou C., Wachter S., 2009, *ApJ*, 707, 844  
 Deller A. T., Camilo F., Reynolds J. E., Halpern J. P., 2012, *ApJ*, 748, L1  
 Dinçel B., Neuhäuser R., Yerli S. K., Anay A., Tetzlaff N., Torres G., Murgauer M., 2015, *Monthly Notices of the Royal Astronomical Society*, 448, 3196  
 Ding H., Deller A., Lower M., Shannon R., 2020, *Proceedings of the International Astronomical Union*, 16, 271  
 Dohm-Palmer R. C., Jones T. W., 1996, *The Astrophysical Journal*, 471, 279

- Doroshenko V., Santangelo A., Tsygankov S., Ji L., 2021, arXiv preprint arXiv:2101.10834
- Duarte-Cabral A., et al., 2021, The SEDIGISM survey: molecular clouds in the inner Galaxy (arXiv:2012.01502), doi:10.1093/mnras/staa2480
- Dubner G., Giacani E., 2015, *The Astronomy and Astrophysics Review*, 23, 3
- Duncan A., Stewart R., Haynes R., Jones K., 1997, *Monthly Notices of the Royal Astronomical Society*, 287, 722
- Durant M., van Kerkwijk M. H., 2006, *ApJ*, 650, 1070
- Dye S., et al., 2006, *MNRAS*, 372, 1227
- Eden D. J., et al., 2017, *MNRAS*, 469, 2163
- Egret D., Wenger M., Dubois P., 1991, in , *Databases & On-line Data in Astronomy*. Springer, pp 79–88
- El-Badry K., et al., 2023, arXiv preprint arXiv:2306.03914
- Esposito P., et al., 2011, *MNRAS*, 416, 205
- Esposito P., et al., 2020, *The Astrophysical Journal Letters*, 896, L30
- Fahlman G. G., Gregory P. C., 1981, *Nature*, 293, 202
- Farrow D. J., et al., 2014, *Monthly Notices of the Royal Astronomical Society*, 437, 748
- Feast M., Shuttleworth M., 1965, *Monthly Notices of the Royal Astronomical Society*, 130, 245
- Fernie J., 1983, *Publications of the Astronomical Society of the Pacific*, 95, 782
- Ferrario L., Wickramasinghe D., 2006, *Monthly Notices of the Royal Astronomical Society*, 367, 1323
- Ferrario L., Wickramasinghe D., 2008, *Monthly Notices of the Royal Astronomical Society: Letters*, 389, L66
- Flewelling H. A., et al., 2020, *The Astrophysical Journal Supplement Series*, 251, 7
- Fortin F., García F., Bunzel A. S., Chaty S., 2023, *Astronomy & Astrophysics*, 671, A149
- Fouesneau M., et al., 2022, arXiv preprint arXiv:2206.05992
- Frail D., Clifton T., 1989, *The Astrophysical Journal*, 336, 854
- Frail D., Goss W., Whiteoak J., 1994, arXiv preprint astro-ph/9407031
- Frail D. A., Kulkarni S. R., Bloom J. S., 1999, *Nature*, 398, 127
- Frederiks D., Palshin V., Aptekar R. L., Golenetskii S., Cline T., Mazets E., 2007, *Astronomy Letters*, 33, 19
- Fryer C., Benz W., Herant M., Colgate S. A., 1999, *The Astrophysical Journal*, 516, 892
- Fuller J., Lu W., 2022, *Monthly Notices of the Royal Astronomical Society*, 511, 3951
- Gaensler B., 2014, *GRB Coordinates Network*, 16533, 1
- Gaensler B., Chatterjee S., 2008, *GRB Coordinates Network*, 8149, 1
- Gaensler B. M., Gotthelf E. V., Vasisht G., 1999b, *ApJ*, 526, L37
- Gaensler B., Gotthelf E., Vasisht G., 1999a, *The Astrophysical Journal*, 526, L37
- Gaensler B. M., McClure-Griffiths N. M., Oey M. S., Haverkorn M., Dickey J. M., Green A. J., 2005, *ApJ*, 620, L95
- Gaia Collaboration et al., 2016, *A&A*, 595, A1
- Gavriil F. P., Kaspi V., Woods P., 2002, *Nature*, 419, 142
- Gelfand J. D., Gaensler B. M., 2007, *ApJ*, 667, 1111
- Gerbrandt S., Foster T. J., Kothes R., Geisbüsch J., Tung A., 2014, *Astronomy & Astrophysics*, 566, A76
- Giacani E., Smith M. J. S., Dubner G., Loiseau N., Castelletti G., Paron S., 2009, *A&A*, 507, 841
- Giacomazzo B., Perna R., 2013, *The Astrophysical Journal Letters*, 771, L26
- Giacomazzo B., Zrake J., Duffell P. C., MacFadyen A. I., Perna R., 2015, *The Astrophysical Journal*, 809, 39
- Gogus E., Gorosabel J., 2011, *GRB Coordinates Network*, 12170, 1
- Gordon Y. A., et al., 2020, *Research Notes of the American Astronomical Society*, 4, 175
- Gordon Y. A., et al., 2021, *ApJS*, 255, 30
- Gordon Y. A., et al., 2023a, *ApJS*, 267, 37
- Gordon A. C., et al., 2023b, *The Astrophysical Journal*, 954, 80
- Gorosabel J., et al., 2011, *The Astronomer's Telegram*, 3496, 1
- Gotthelf E. V., Halpern J. P., 2008, in Bassa C., Wang Z., Cumming A., Kaspi V. M., eds, *American Institute of Physics Conference Series Vol. 983*, 40
- Years of Pulsars: Millisecond Pulsars, Magnetars and More. pp 320–324 (arXiv:0711.1554), doi:10.1063/1.2900174
- Gotthelf E. V., Vasisht G., Boylan-Kolchin M., Torii K., 2000, *ApJ*, 542, L37
- Gotthelf E. V., Halpern J. P., Seward F. D., 2005, *ApJ*, 627, 390
- Gotthelf E. V., Halpern J. P., Alford J., 2013, *ApJ*, 765, 58
- Göğüş E., et al., 2010a, *ApJ*, 718, 331
- Göğüş E., Woods P. M., Kouveliotou C., Kaneko Y., Gaensler B. M., Chatterjee S., 2010b, *ApJ*, 722, 899
- Green D. A., 1987, *A catalogue of galactic supernova remnants*. Mullard radio astronomy observatory
- Green D., 2019, *Journal of Astrophysics and Astronomy*, 40, 36
- Green G. M., et al., 2015, *The Astrophysical Journal*, 810, 25
- Green G. M., et al., 2018, *Monthly Notices of the Royal Astronomical Society*, 478, 651
- Green G. M., Schlafly E., Zucker C., Speagle J. S., Finkbeiner D., 2019, *ApJ*, 887, 93
- Greisen E. W., Calabretta M. R., 2002, *Astronomy & Astrophysics*, 395, 1061
- Güver T., Özel F., 2009, *Monthly Notices of the Royal Astronomical Society*, 400, 2050
- H. E. S. S. Collaboration et al., 2018, *A&A*, 612, A11
- Haberl F., 2007, *Astrophysics and Space Science*, 308, 181
- Hale C. L., et al., 2021, arXiv preprint arXiv:2109.00956
- Halpern J., 2011, *GRB Coordinates Network*, 12260, 1
- Halpern J. P., Gotthelf E. V., 2010a, *ApJ*, 710, 941
- Halpern J. P., Gotthelf E. V., 2010b, *ApJ*, 725, 1384
- Halpern J. P., Gotthelf E. V., Camilo F., Seward F. D., 2007, *ApJ*, 665, 1304
- Hambly N. C., et al., 2008, *MNRAS*, 384, 637
- Hamuy M., 2003, *The Astrophysical Journal*, 582, 905
- Haschke R., Grebel E. K., Duffau S., 2012, *AJ*, 144, 107
- Heinze A. N., et al., 2018, *AJ*, 156, 241
- Helfand D. J., Collins B. F., Gotthelf E. V., 2003, *ApJ*, 582, 783
- Helfand D. J., Becker R. H., White R. L., Fallon A., Tuttle S., 2006, *The Astronomical Journal*, 131, 2525
- Helfand D. J., Chatterjee S., Brisken W. F., Camilo F., Reynolds J., van Kerkwijk M. H., Halpern J. P., Ransom S. M., 2007, *ApJ*, 662, 1198
- Hewett P. C., Warren S. J., Leggett S. K., Hodgkin S. T., 2006, *MNRAS*, 367, 454
- Hewitt J. W., Yusef-Zadeh F., 2009, *The Astrophysical Journal*, 694, L16
- Hobbs G., et al., 2004, *Monthly Notices of the Royal Astronomical Society*, 352, 1439
- Hobbs G., Lorimer D. R., Lyne A. G., Kramer M., 2005, *MNRAS*, 360, 974
- Hodgkin S. T., Irwin M. J., Hewett P. C., Warren S. J., 2009, *MNRAS*, 394, 675
- Høg E., et al., 2000a, *A&A*, 355, L27
- Høg E., et al., 2000b, *Astronomy and Astrophysics*, v. 357, p. 367-386 (2000), 357, 367
- Hulleman F., Tennant A. F., van Kerkwijk M. H., Kulkarni S. R., Kouveliotou C., Patel S. K., 2001, *ApJ*, 563, L49
- Hulleman F., Van Kerkwijk M., Kulkarni S., 2004, *Astronomy & Astrophysics*, 416, 1037
- Hurley K., Kouveliotou C., Cline T., Mazets E., Golenetskii S., Frederiks D. D., van Paradijs J., 1999, *ApJ*, 523, L37
- Ibrahim A. Y., et al., 2024, *An X-ray and radio view of the 2022 reactivation of the magnetar SGRJ1935+2154* (arXiv:2402.08596)
- Irwin M. J., et al., 2004, in *Optimizing scientific return for astronomy through information technologies*. pp 411–422
- Israel G. L., et al., 2003, *ApJ*, 589, L93
- Israel G., et al., 2005, arXiv preprint astro-ph/0506095
- Israel G. L., et al., 2016, *MNRAS*, 457, 3448
- Jiao W., Wang K., Pillai T. G., Baug T., Zhang S., Xu F., 2023, *The Astrophysical Journal*, 945, 81
- Jing W. C., et al., 2023, *MNRAS*, 523, 4949
- Kaiser N., 2004, in *Oschmann Jacobus M. J., ed., Society of Photo-Optical Instrumentation Engineers (SPIE) Conference Series Vol. 5489, Ground-based Telescopes*. pp 11–22, doi:10.1117/12.552472
- Kaiser N., et al., 2002, in *Survey and Other Telescope Technologies and Discoveries*. pp 154–164
- Kargaltsev O., et al., 2012, *ApJ*, 748, 26



- Karuppusamy R., et al., 2020, *The Astronomer's Telegram*, 13553, 1
- Kaspi V. M., 1996, in Johnston S., Walker M. A., Bailes M., eds, *Astronomical Society of the Pacific Conference Series Vol. 105, IAU Colloq. 160: Pulsars: Problems and Progress*. p. 375
- Kaspi V. M., Beloborodov A. M., 2017, *Annual Review of Astronomy and Astrophysics*, 55, 261
- Keane E. F., Kramer M., 2008, *Monthly Notices of the Royal Astronomical Society*, 391, 2009
- Kirsten F., et al., 2022, *Nature*, 602, 585
- Klose S., et al., 2004, *ApJ*, 609, L13
- Kobulnicky H. A., Fryer C. L., 2007, *The Astrophysical Journal*, 670, 747
- Kochanek C. S., 2009, *The Astrophysical Journal*, 707, 1578
- Kochanek C., 2018, *Monthly Notices of the Royal Astronomical Society*, 473, 1633
- Kochanek C., 2021, *Monthly Notices of the Royal Astronomical Society*, 507, 5832
- Kochanek C., 2023, *Monthly Notices of the Royal Astronomical Society*, 519, 3865
- Kochanek C., Auchettl K., Belczynski K., 2019, *Monthly Notices of the Royal Astronomical Society*, 485, 5394
- Kothes R., Dougherty S., 2008, *Revista Mexicana de Astronomía y Astrofísica*, 33, 163
- Kothes R., Foster T., 2012, *ApJ*, 746, L4
- Kothes R., Fedotov K., Foster T., Uyaniker B., 2006, *Astronomy & Astrophysics*, 457, 1081
- Kothes R., Sun X., Gaensler B., Reich W., 2018, *The Astrophysical Journal*, 852, 54
- Kouwenhoven M. B. N., Brown A. G. A., Zinnecker H., Kaper L., Portegies Zwart S. F., 2005, *A&A*, 430, 137
- Kramer M., Wex N., Wielebinski R., 2000, in *IAU Colloq. 177: Pulsar Astronomy-2000 and Beyond*.
- Kremer K., Fuller J., Piro A. L., Ransom S. M., 2023, *MNRAS*, 525, L22
- Krimm H. A., Lien A. Y., Page K. L., Palmer D. M., Tohuvavohu A., 2020, *The Astronomer's Telegram*, 13913, 1
- Kron R. G., 1980, *The Astrophysical Journal Supplement Series*, 43, 305
- Kroupa P., 2002, *Science*, 295, 82
- Kroupa P., Weidner C., 2003, *The Astrophysical Journal*, 598, 1076
- Kroupa P., Tout C. A., Gilmore G., 1993, *Monthly Notices of the Royal Astronomical Society*, 262, 545
- Kulkarni S. R., Clifton T. C., Backer D. C., Foster R. S., Fruchter A. S., Taylor J. H., 1988, *Nature*, 331, 50
- Kulkarni S. R., Kaplan D. L., Marshall H. L., Frail D. A., Murakami T., Yonetoku D., 2003, *ApJ*, 585, 948
- Laha S., et al., 2020, *GRB Coordinates Network*, 28193, 1
- Lamb R. C., Fox D. W., Macomb D. J., Prince T. A., 2002, *ApJ*, 574, L29
- Lamb D., Graziani C., Shirasaki Y., Atteia J., et al., 2003, *GCN Circ.*, 2351
- Lawrence A., et al., 2007b, *MNRAS*, 379, 1599
- Lawrence A., et al., 2007a, *Monthly Notices of the Royal Astronomical Society*, 379, 1599
- Lawrence A., et al., 2012, *VizieR Online Data Catalog: UKIDSS-DR8 LAS, GCS and DXS Surveys (Lawrence+ 2012)*, *VizieR On-line Data Catalog: II/314*. Originally published in: 2007MNRAS.379.1599L; 2012yCat.2314....0U
- Lawrence A., et al., 2013, *VizieR Online Data Catalog: UKIDSS-DR9 LAS, GCS and DXS Surveys (Lawrence+ 2012)*, *VizieR On-line Data Catalog: II/319*. Originally published in: 2007MNRAS.379.1599L
- Leahy D. A., Tian W., 2007, *arXiv preprint arXiv:0711.4107*
- Leahy D. A., Tian W. W., 2008a, *AJ*, 135, 167
- Leahy D. A., Tian W., 2008b, *Astronomy & Astrophysics*, 480, L25
- Levin L., et al., 2010, *ApJ*, 721, L33
- Lin L., et al., 2011, *ApJ*, 739, 87
- Lin D., Webb N. A., Barret D., 2012, *ApJ*, 756, 27
- Lindgren L., et al., 2021, *Astronomy & Astrophysics*, 649, A2
- Livingstone M. A., Ng C. Y., Kaspi V. M., Gavriil F. P., Gotthelf E. V., 2011, *ApJ*, 730, 66
- Lorimer D., Lyne A., Camilo F., 1998, *arXiv preprint astro-ph/9801096*
- Lu W., Beniamini P., Kumar P., 2022, *Monthly Notices of the Royal Astronomical Society*, 510, 1867
- Lucas P., et al., 2008, *Monthly Notices of the Royal Astronomical Society*, 391, 136
- Lyman J., Levan A., Wiersema K., Kouveliotou C., Chrimas A., Fruchter A., 2022, *The Astrophysical Journal*, 926, 121
- Lyne A., Stappers B., Keith M., Ray P., Kerr M., Camilo F., Johnson T., 2015, *Monthly Notices of the Royal Astronomical Society*, 451, 581
- Malofeev V. M., Malov O. I., Teplykh D. A., Glushak A. P., 2005, *The Astronomer's Telegram*, 501, 1
- Manchester R. N., Hobbs G. B., Teoh A., Hobbs M., 2005, *AJ*, 129, 1993
- Maund J., Pastorello A., Mattila S., Itagaki K., Boles T., 2016, *The Astrophysical Journal*, 833, 128
- Mazets E., et al., 2008, *The Astrophysical Journal*, 680, 545
- McConnell D., et al., 2020, *Publications of the Astronomical Society of Australia*, 37, e048
- Mereghetti S., Esposito P., Tiengo A., Gotz D., Israel G., De Luca A., 2012, *arXiv preprint arXiv:1208.0249*
- Mereghetti S., et al., 2024, *A magnetar giant flare in the nearby starburst galaxy M82 (arXiv:2312.14645)*
- Migliazzo J., Gaensler B., Backer D., Stappers B., Van Der Swaluw E., Strom R., 2002, *The Astrophysical Journal*, 567, L141
- Miller G. E., Scalo J. M., 1979, and JM Scalo. *Astrophysical Journal Supplement Series*, vol. 41, Nov. 1979, p. 513-547., 41, 513
- Minaev P. Y., Pozanenko A. S., Grebenev S. A., Chelovekov I. V., Pankov N. S., Khabibullin A. A., Inasaridze R. Y., Novichonok A. O., 2024, *GRB 231115A – a magnetar giant flare in the M82 galaxy (arXiv:2402.08623)*
- Minter A. H., Camilo F., Ransom S. M., Halpern J. P., Zimmerman N., 2008, *ApJ*, 676, 1189
- Moe M., Di Stefano R., 2017, *The Astrophysical Journal Supplement Series*, 230, 15
- Moisés A., Damineli A., Figuerêdo E., Blum R., Conti P., Barbosa C., 2011, *Monthly Notices of the Royal Astronomical Society*, 411, 705
- Mondal T., 2021, *The Astrophysical Journal Letters*, 913, L12
- Mori K., et al., 2013a, *ApJ*, 770, L23
- Mori K., Gotthelf E. V., Barriere N. M., Hailey C. J., Harrison F. A., Kaspi V. M., Tomsick J. A., Zhang S., 2013b, *The Astronomer's Telegram*, 5020, 1
- Morozova V., Piro A. L., Valenti S., 2017, *The Astrophysical Journal*, 838, 28
- Muno M. P., et al., 2006, *ApJ*, 636, L41
- Nakano T., Murakami H., Makishima K., Hiraga J. S., Uchiyama H., Kaneda H., Enoto T., 2015, *Publications of the Astronomical Society of Japan*, 67, 9
- Nakano T., Murakami H., Furuta Y., Enoto T., Masuyama M., Shigeyama T., Makishima K., 2017, *Publications of the Astronomical Society of Japan*, 69, 40
- Neumann M., Avakyan A., Doroshenko V., Santangelo A., 2023, *A&A*, 677, A134
- Nguyen H., et al., 2015, *ApJ*, 812, 7
- Nikzat F., et al., 2022, *Astronomy & Astrophysics*, 660, A35
- Nomoto K., Iwamoto K., Suzuki T., 1995, *Physics Reports*, 256, 173
- Obergaulinger M., Janka H.-T., Aloy M. Á., 2014, *Monthly Notices of the Royal Astronomical Society*, 445, 3169
- Olausen S., Kaspi V., 2014, *The Astrophysical Journal Supplement Series*, 212, 6
- Onken C. A., Wolf C., Bessell M. S., Chang S.-W., Luvaul L. C., Tonry J. L., White M. C., Costa G. S. D., 2024, *SkyMapper Southern Survey: Data Release 4 (arXiv:2402.02015)*
- Pagani C., Beardmore A., Kennea J., 2011, *The Astronomer's Telegram*, 3493, 1
- Park S., Hughes J. P., Slane P. O., Burrows D. N., Lee J.-J., Mori K., 2012, *The Astrophysical Journal*, 748, 117
- Park S., Bhalerao J., Kargaltsev O., Slane P. O., 2020, *The Astrophysical Journal*, 894, 17
- Petroff E., Hessels J., Lorimer D., 2022, *The Astronomy and Astrophysics Review*, 30, 2
- Pires A., Motch C., Turolla R., Treves A., Popov S., 2009, *Astronomy & Astrophysics*, 498, 233

- Pons J. A., Geppert U., 2007, *Astronomy & Astrophysics*, 470, 303
- Ponti G., et al., 2015, *Monthly Notices of the Royal Astronomical Society*, 453, 172
- Popov S. B., 2020, *Proceedings of the International Astronomical Union*, 16, 61
- Poveda A., Ruiz J., Allen C., 1967, *Boletín de los Observatorios Tonantzintla y Tacubaya*, 4, 86
- Predehl P., Schmitt J. H., 1995, *Astronomy and Astrophysics*, Vol. 293, p. 889-905 (1995), 293, 889
- Rea N., Viganò D., Israel G. L., Pons J. A., Torres D. F., 2014, *ApJ*, 781, L17
- Reich W., Fuerst E., Reich P., Reif K., 1990, *Astronomy and Astrophysics Supplement Series* (ISSN 0365-0138), vol. 85, no. 1, Oct. 1990, p. 633-690., 85, 633
- Renzo M., et al., 2019, *Astronomy & Astrophysics*, 624, A66
- Revnivtsev M., Mereghetti S., 2016, *The Strongest Magnetic Fields in the Universe*, pp 299–320
- Richardson N. D., et al., 2023, *Nature*, 614, 45
- Roming P., et al., 2008, *The Astrophysical Journal*, 690, 163
- Ruiter A., Ferrario L., Belczynski K., Seitenzahl I., Crocker R., Karakas A., 2019, *Monthly Notices of the Royal Astronomical Society*, 484, 698
- Sakamoto T., et al., 2011a, *Advances in space research*, 47, 1346
- Sakamoto T., et al., 2011b, *Advances in Space Research*, 47, 1346
- Salpeter E. E., 1955, *Astrophysical Journal*, vol. 121, p. 161, 121, 161
- Sano H., et al., 2023, *The Astrophysical Journal*, 958, 53
- Sathyaprakash R., et al., 2024, Long-term study of the 2020 magnetar-like outburst of the young pulsar PSRJ1846-0258 in Kes 75 ([arXiv:2401.08010](https://arxiv.org/abs/2401.08010))
- Sato T., Koyama K., Lee S.-H., Takahashi T., 2016, *PASJ*, 68, S8
- Savage B. D., Mathis J. S., 1979, *Annual review of astronomy and astrophysics*, 17, 73
- Sayers S. L., Curran P. J., Mueser K. T., 1996, *Psychological Assessment*, 8, 269
- Schlafly E. F., Finkbeiner D. P., 2011, *The Astrophysical Journal*, 737, 103
- Schlafly E., et al., 2015, *The Astrophysical Journal*, 799, 116
- Schneider F. R., Ohlmann S. T., Podsiadlowski P., Röpke F. K., Balbus S. A., Pakmor R., Springel V., 2019, *Nature*, 574, 211
- Scholz P., Ng C. Y., Livingstone M. A., Kaspi V. M., Cumming A., Archibald R. F., 2012, *ApJ*, 761, 66
- Scholz P., Kaspi V., Cumming A., 2014, *The Astrophysical Journal*, 786, 62
- Schwope A., Hasinger G., Schwarz R., Haberl F., Schmidt M., 1998, *arXiv preprint astro-ph/98111326*
- Seaton M. J., 1979, *MNRAS*, 187, 73
- Sedov L. I., 1946, *Journal of Applied Mathematics and Mechanics*, 10, 241
- Sedov L. I., 2018, *Similarity and dimensional methods in mechanics*. CRC press
- Seward F., Slane P., Smith R., Sun M., 2003, *The Astrophysical Journal*, 584, 414
- Shannon R. M., Johnston S., 2013, *MNRAS*, 435, L29
- Sharma K., et al., 2023, *The Astrophysical Journal*, 950, 175
- Shen K. J., et al., 2018, *ApJ*, 865, 15
- Shenar T., et al., 2023, *Science*, 381, 761–765
- Shimwell T., 2016, LoTSS-PDR Image Archive, VO resource provided by the The VO @ ASTRON, [https://vo.astron.nl/lofartier1/q\\_img/imgs/info](https://vo.astron.nl/lofartier1/q_img/imgs/info)
- Shimwell T., et al., 2022, *Astronomy & Astrophysics*, 659, A1
- Simpson R. J., et al., 2012, *MNRAS*, 424, 2442
- Skrutskie M. F., et al., 2006, *AJ*, 131, 1163
- Smith L., et al., 2018, *Monthly Notices of the Royal Astronomical Society*, 474, 1826
- Spangler S. R., Owen F. N., Hulse R., 1977, *Astronomical Journal*, vol. 82, Dec. 1977, p. 989-997., 82, 989
- Sramek R. A., Cowan J. J., Roberts D. A., Goss W. M., Ekers R. D., 1992, *AJ*, 104, 704
- Stairs I. H., et al., 2001, *Monthly Notices of the Royal Astronomical Society*, 325, 979
- Stamatikos M., et al., 2020, *GRB Coordinates Network*, 27384, 1
- Stetson P. B., 2000, *PASP*, 112, 925
- Straal S. M., Gelfand J. D., Eagle J. L., 2023, *ApJ*, 942, 103
- Stupar M., Filipović M., Parker Q. A., White G. L., Pannuti T. G., Jones P. A., 2007, *Astrophysics and Space Science*, 307, 423
- Sun M., Seward F. D., Smith R. K., Slane P. O., 2004, *ApJ*, 605, 742
- Surnis M. P., Maan Y., Joshi B. C., Manoharan P. K., 2016, *The Astronomer's Telegram*, 8943, 1
- Suzuki H., Bamba A., Shibata S., 2021, *The Astrophysical Journal*, 914, 103
- Svinkin D., et al., 2021, *Nature*, 589, 211
- Tam C. R., Kaspi V. M., Gaensler B. M., Gotthelf E. V., 2006, *ApJ*, 652, 548
- Tan C. M., et al., 2020, *MNRAS*, 492, 5878
- Taylor G. I., 1950, *Proceedings of the Royal Society of London. Series A. Mathematical and Physical Sciences*, 201, 159
- Tendulkar S. P., Cameron P. B., Kulkarni S. R., 2012, *The Astrophysical Journal*, 761, 76
- Tendulkar S. P., Cameron P. B., Kulkarni S. R., 2013, *The Astrophysical Journal*, 772, 31
- Tetzlaff N., Neuhäuser R., Hohle M., 2010, *Monthly Notices of the Royal Astronomical Society*, 410, 190
- Tetzlaff N., Eisenbeiss T., Neuhäuser R., Hohle M. M., 2011, *Monthly Notices of the Royal Astronomical Society*, 417, 617
- Thielemann F.-K., Nomoto K., Hashimoto M., 1996, *Core-collapse supernovae and their ejecta*
- Tian W. W., Leahy D. A., 2008, *ApJ*, 677, 292
- Tian W. W., Leahy D. A., 2012, *MNRAS*, 421, 2593
- Tiengo A., et al., 2010, *ApJ*, 710, 227
- Tong H., Huang L., 2020, *Monthly Notices of the Royal Astronomical Society*, 497, 2680
- Tonry J., et al., 2012, *The Astrophysical Journal*, 750, 99
- Torii K., Kinugasa K., Katayama K., Tsunemi H., Yamauchi S., 1998a, *The Astrophysical Journal*, 503, 843
- Torii K., Kinugasa K., Katayama K., Tsunemi H., Yamauchi S., 1998b, *ApJ*, 503, 843
- Trigg A. C., et al., 2023, *arXiv preprint arXiv:2311.09362*
- Truelove J. K., McKee C. F., 1999, *The Astrophysical Journal Supplement Series*, 120, 299
- Turolla R., 2009, in *Neutron stars and pulsars*. Springer, pp 141–163
- Vallenari A., et al., 2022, *arXiv preprint arXiv:2208.00211*
- Vasisht G., Gotthelf E. V., 1997, *ApJ*, 486, L129
- Velusamy T., Becker R. H., Seward F. D., 1991, *AJ*, 102, 676
- Vincenty T., 1975, *Survey Review*, 23, 88
- Irba F. J., Henden A. A., Luginbuhl C. B., Guetter H. H., Hartmann D. H., Klose S., 2000, *ApJ*, 533, L17
- Wachter S., et al., 2004, *ApJ*, 615, 887
- Wang Z., Chakrabarty D., 2002, *ApJ*, 579, L33
- Weidner C., Kroupa P., 2005, *The Astrophysical Journal*, 625, 754
- Wheeler J. A., 1966, *Annual Review of Astronomy and Astrophysics*, 4, 393
- White C. J., Burrows A., Coleman M. S., Vartanyan D., 2022, *The Astrophysical Journal*, 926, 111
- Whiteoak J., Green A., 1996, *Astronomy and Astrophysics Supplement Series*, 118, 329
- Wolf C., et al., 2018, *Publications of the Astronomical Society of Australia*, 35, e010
- Woodland M. N., et al., 2023, *arXiv preprint arXiv:2312.01578*
- Yalinewich A., Piran T., Sari R., 2017, *The Astrophysical Journal*, 838, 12
- Yao J., Manchester R., Wang N., 2017, *The Astrophysical Journal*, 835, 29
- Yeung P. K. H., Kong A. K. H., Tam P. H. T., Lin L. C. C., Hui C. Y., Hu C.-P., Cheng K. S., 2016, *ApJ*, 827, 41
- Younes G., et al., 2023, *Nature Astronomy*, 7, 339
- Zacharias N., Urban S. E., Zacharias M. I., Wycoff G. L., Hall D. M., Monet D. G., Rafferty T. J., 2004, *The Astronomical Journal*, 127, 3043
- Zacharias N., Monet D., Levine S., Urban S., Gaume R., Wycoff G., 2005, *VizieR Online Data Catalog*, pp I–297
- Zapartas E., et al., 2017, *Astronomy & Astrophysics*, 601, A29
- Zhong S.-Q., Dai Z.-G., Zhang H.-M., Deng C.-M., 2020, *The Astrophysical Journal Letters*, 898, L5
- Zhou P., Chen Y., Li X.-D., Safi-Harb S., Mendez M., Terada Y., Sun W., Ge M.-Y., 2014, *ApJ*, 781, L16
- Zhou P., Chen Y., Safi-Harb S., Zhou X., Sun M., Zhang Z.-Y., Zhang G.-Y., 2016, *ApJ*, 831, 192

- Zhou P., Vink J., Safi-Harb S., Miceli M., 2019, *Astronomy & Astrophysics*, 629, A51
- Zhou P., Zhou X., Chen Y., Wang J.-S., Vink J., Wang Y., 2020, *The Astrophysical Journal*, 905, 99
- de Lima R. C. R., et al., 2024, Evidence for 3XMM J185246.6+003317 as a massive magnetar with a low magnetic field ([arXiv:2210.06648](https://arxiv.org/abs/2210.06648))
- van der Horst A. J., et al., 2010, *ApJ*, 711, L1
- van der Wateren E., Bassa C. G., Janssen G. H., Yanes-Rizo I. V., Casares J., Nelemans G., Stappers B. W., Tan C. M., 2023, PSR J0210+5845; An ultra wide binary pulsar with a B6V main-sequence star companion ([arXiv:2312.01892](https://arxiv.org/abs/2312.01892))

## APPENDIX A: GAIA ADQL QUERY AND PHOTOMETRIC CONVERSIONS

Below is the ADQL query used to compile the initial sample of *Gaia* sources:

---

```

select * from (
  select *,phot_g_mean_mag_absolute - (-0.02704 +
    0.1424*bp_rp_absolute -
    0.2156*POWER(bp_rp_absolute,2) +
    0.01426*POWER(bp_rp_absolute,3))
    AS phot_v_mean_mag_absolute from (
  select source_id,
  ra,
  ra_error,
  dec,
  dec_error,
  parallax,
  parallax_error,
  parallax_over_error,
  pm,
  pmra,
  pmra_error,
  pmdec,
  pmdec_error,
  ruwe,
  phot_g_n_obs,
  phot_g_mean_flux,
  phot_g_mean_flux_error,
  phot_g_mean_flux_over_error,
  phot_g_mean_mag,
  phot_bp_n_obs,
  phot_bp_mean_flux,
  phot_bp_mean_flux_error,
  phot_bp_mean_flux_over_error,
  phot_bp_mean_mag,
  phot_rp_n_obs,
  phot_rp_mean_flux,
  phot_rp_mean_flux_error,
  phot_rp_mean_flux_over_error,
  phot_rp_mean_mag,
  phot_bp_rp_excess_factor,
  bp_rp,
  bp_g,
  g_rp,
  radial_velocity,
  radial_velocity_error,
  teff_gspphot,

```

```

  teff_gspphot_lower,
  teff_gspphot_upper,
  logg_gspphot,
  logg_gspphot_lower,
  logg_gspphot_upper,
  mh_gspphot,
  distance_gspphot,
  distance_gspphot_lower,
  distance_gspphot_upper,
  azero_gspphot,
  azero_gspphot_upper,
  ag_gspphot,
  ag_gspphot_lower,
  ag_gspphot_upper,
  ebpmnrp_gspphot,
  ebpmnrp_gspphot_lower,
  ebpmnrp_gspphot_upper,
  l,
  b,
  phot_g_mean_mag-ag_gspphot-(
    5*LOG10(1000*ABS(parallax))-5)
  AS phot_g_mean_mag_absolute,
  bp_rp - ebpmnrp_gspphot
  AS bp_rp_absolute
  from gaiadr3.gaia_source
  AS m)
  AS mm)
  AS mmm
WHERE parallax+parallax_error>0.008
  and parallax-parallax_error<1
  and phot_v_mean_mag_absolute<1.18
  and b>-80
  and b<20

```

---

The magnitude limit was re-applied, along with the color limit, after the initial query to incorporate the *Bayestar19* extinction estimates. From *Bayestar19* we obtain the  $E_{B-V}$  color excess and convert it to  $E_{G-V}$  using the Johnson-Cousins Relations<sup>45</sup>:

$$E_{G-V} = -0.04749 - 0.0124E_{B-V} - 0.2901E_{B-V}^2 + 0.02008E_{B-V}^3 + 0.04772E_{B-V}^4 \quad (\text{A1})$$

and similarly the  $G_{BP} - G_{RP}$  excess:

$$E_{G_{BP}-G_{RP}} = 0.06483 + 1.575E_{B-V} - 0.7815E_{B-V}^2 + 0.5707E_{B-V}^3 - 0.176E_{B-V}^4 + 0.01916E_{B-V}^5 \quad (\text{A2})$$

(e.g. [Fernie 1983](#); [Stetson 2000](#)). The  $V$ - and  $G$ - band extinction are then computed using:

$$A_V \approx 3.2E_{B-V} \quad (\text{A3})$$

$$A_G \approx A_V + E_{G-V} \quad (\text{A4})$$

(e.g. [Savage & Mathis 1979](#); [Seaton 1979](#)). The  $G$ -band absolute magnitude is then:

<sup>45</sup> See the *Gaia* DR3 Documentation at <https://gea.esac.esa.int/archive/documentation/GDR3/> Section 5.5.1 Table 5.9 for details.

$$M_G = m_G - A_G - (5 \log_{10}(d) - 5) \quad (\text{A5})$$

while the absolute color is:

$$G_{BP} - G_{RP} = m_{G_{BP}} - m_{G_{RP}} - E_{G_{BP}-G_{RP}} \quad (\text{A6})$$

Finally, we derive the absolute  $G-V$  color from the Johnson-Cousins relations:

$$G - V = -0.027 + 0.01424(G_{BP} - G_{RP}) - 0.2156(G_{BP} - G_{RP})^2 + 0.07426(G_{BP} - G_{RP})^3 \quad (\text{A7})$$

which is used to get the absolute  $V$ -band magnitude:

$$M_V = M_G - (G - V) \quad (\text{A8})$$

For source with  $\delta \leq -30^\circ$ , the extinction and color excess from *Gaia* GSP-Aeneas photometry are used as described in Section 3.

## APPENDIX B: DEFINITION OF ASSOCIATION P-VALUES

In this appendix, we explicitly define p-values for association of magnetars with SNRs, bound companions, and unbound companions from the radio, optical, IR, and *Gaia* searches. The p-values are based on the criteria defined in Sections 4.1-3, and are estimated through Monte Carlo simulations.

### B1 Optical Search for Bound Companions

Recall for the bound companion search, the null hypothesis ( $H_0$ ) is that the magnetar and source are not bound in a binary system, and we use the position, distance, and difference between PSF and Kron magnitudes ('grizy' for PS1, 'uvgriz' for SkyMapper) as association criteria. For each source, we draw 1000 samples of the RA and declination of the source and magnetar ( $\alpha_{\text{PS1}}, \delta_{\text{PS1}}, \alpha_{\text{mag}}, \delta_{\text{mag}}$ ), and the distance of the magnetar ( $d_{\text{mag}}$ ), assuming each are normally distributed. Using  $\Delta\alpha = |\alpha_{\text{PS1}} - \alpha_{\text{mag}}|$ ,  $\Delta\delta = |\delta_{\text{PS1}} - \delta_{\text{mag}}|$ , we compute the search statistic  $\hat{g}_1$  as the fraction of samples that fall below the 95<sup>th</sup> percentiles of folded zero-mean normal distributions with  $\sigma_\alpha = (\sigma_{\alpha, \text{PS1}}^2 + \sigma_{\alpha, \text{mag}}^2)^{1/2}$  and  $\sigma_\delta = (\sigma_{\delta, \text{PS1}}^2 + \sigma_{\delta, \text{mag}}^2)^{1/2}$ , respectively. The  $H_0$  distribution of  $\hat{g}_1$  is estimated by repeating the simulation 100 times with mean  $\Delta\alpha, \Delta\delta$  selected uniformly between  $1 - 5\sigma_{\alpha/\delta}$ , and the p-value  $p_1$  is taken as the percentile of  $\hat{g}_1$  given the resulting  $\hat{g}_1$  distribution.

$p_2$  is computed by a similar process; since the errors on apparent magnitudes are small, we assume they are negligible, and use  $g$ - and  $r$ -band magnitudes to derive the apparent  $V$ -band magnitude:

$$m_V = m_r + 0.005 + 0.462(m_g - m_r) + 0.013(m_g - m_r)^2 \quad (\text{B1})$$

(Tonry et al. 2012). From *Bayestar19* we obtain the  $B-V$  color excess<sup>46</sup> along the source's sightline,  $E_{B-V}$ , for distances between 60 pc–60 kpc, converting to the  $V$ -band extinction with  $A_V \approx 3.2E_{B-V}$ . If *Bayestar19* extinction estimates are not available, we use the  $N_H - A_V$  relation from Predehl & Schmitt (1995)

<sup>46</sup> Note that *Bayestar19* reports reddening in arbitrary units and is converted to  $E_{B-V}$  by multiplying by 0.995 as described at <http://argonaut.skymaps.info/usage> (Schlafly & Finkbeiner 2011). We proceed assuming this factor is approximately 1, which is accurate to the first decimal place.

from Table 1. Then, after samples of the absolute magnitude are drawn from a uniform distribution between  $-10 \lesssim M_V \lesssim 3$ , linear interpolation is used to obtain a sample of the PS1 source distance,  $d_{\text{PS1}}$ , from the difference  $m_V - M_V$ . Finally, we use the magnetar distance samples to get samples of  $\Delta d = |d_{\text{PS1}} - d_{\text{mag}}|$ , which is again compared to the 95<sup>th</sup> percentile of a folded zero-mean distribution and  $H_0$  samples between  $1 - 10\sigma_{\Delta d}$  to get the statistic  $\hat{g}_2$  and p-value  $p_2$ .

Finally, the Kron magnitude describes the flux of extended sources within a characteristic Kron radius (Kron 1980). As described by Farrow et al. (2014), the difference  $m_{x, \text{Kron}} - m_{x, \text{PSF}}$  can be used to distinguish between point sources and extended sources by imposing a cutoff  $m_{x, \text{cutoff}}(m_{x, \text{Kron}})$ . Point sources are expected to exceed this limit, and we adopt the Farrow et al. (2014) fit equation for the cutoff:

$$m_{x, \text{cutoff}}(m_{x, \text{Kron}}) = -0.319 + 0.129(m_{x, \text{Kron}} - 21) + 0.007(m_{x, \text{Kron}} - 21)^2 \quad (\text{B2})$$

Since the apparent magnitude error is negligible, we set the p-value  $p_{3,x} = 0$  if  $m_{x, \text{Kron}} - m_{x, \text{PSF}} > m_{x, \text{cutoff}}(m_{x, \text{Kron}})$  and  $p_{3,x} = 1$  if  $m_{x, \text{Kron}} - m_{x, \text{PSF}} \leq m_{x, \text{cutoff}}(m_{x, \text{Kron}})$ , combining results in all available passbands to get  $p_3$ :

$$p_3 = 1 - \prod_x^{\text{'uvgrizy'}} (1 - p_{3,x}) \quad (\text{B3})$$

For SkyMapper sources, multiple measurements for the Kron and PSF magnitudes are available in each band, each of which is used to compute  $p_3$ . We additionally exclude SkyMapper sources with stellar classification probability (*class\_star*) < 90% to avoid extended objects (Wolf et al. 2018; Onken et al. 2024).

### B2 Infrared Search for Bound Companions

Like the optical search, the IR search uses the position, distance, and PSF  $J$ - and  $H$ -band magnitudes as criteria for association, with  $H_0$  that the magnetar and source are not bound in a binary system.  $p_1$  is computed in a similar way to the optical data for UKIDSS and VVV using their respective PSF FWHMs,  $1''$  and  $0.75''$ , as errors in RA and declination. For 2MASS sources, the RA and declination are sampled as a bi-normal distribution using the reported major axis ( $a_{\text{IR}}$ ), minor axis ( $b_{\text{IR}}$ ), and position angle ( $\phi_{\text{IR}}$ ) of the error ellipse. The covariance matrix of the bi-normal distribution is given by:

$$\sigma_{\text{pos}} = \begin{bmatrix} (a_{\text{IR}} \sin(\phi_{\text{IR}}))^2 + (b_{\text{IR}} \cos(\phi_{\text{IR}}))^2 & (a_{\text{IR}}^2 - b_{\text{IR}}^2) \cos(\phi_{\text{IR}}) \sin(\phi_{\text{IR}}) \\ (a_{\text{IR}}^2 - b_{\text{IR}}^2) \cos(\phi_{\text{IR}}) \sin(\phi_{\text{IR}}) & (a_{\text{IR}} \cos(\phi_{\text{IR}}))^2 + (b_{\text{IR}} \sin(\phi_{\text{IR}}))^2 \end{bmatrix} \quad (\text{B4})$$

We proceed as in the PS1 search to compute the search statistic  $\hat{g}_1$  and its p-value  $p_1$ , utilizing the 95<sup>th</sup> percentile contour as a threshold and simulating the  $H_0$  distribution of angular separation,  $\Delta\theta$ , using mean separations between  $1 - 5\sigma_{\text{pos}}\{1, 1\}$  for RA and  $1 - 5\sigma_{\text{pos}}\{0, 0\}$  for declination.

For the second condition we follow the same method as for PS1 sources using instead the  $J$ -band and  $H$ -band magnitudes,  $m_J$  and  $m_H$ . Following Chrimes et al. (2022b), we expect OB stars to have  $H$ -band magnitudes in the range  $-2.76 \lesssim M_H \lesssim 3.34$  and  $J-H$  colors between  $-0.14 \lesssim J-H \lesssim 0.31$ . After drawing samples of  $M_H$  and  $J-H$  from uniform distributions in these ranges, we compute  $M_J = (J-H) + M_H$ . The *Bayestar19* extinction library is again queried, using  $A_H \approx 0.4690E_{B-V}$  and  $A_J \approx 0.7927E_{B-V}$ , and the inferred distance is estimated from both the  $J$ - and  $H$ -bands,  $d_{\text{IR},J}$  and  $d_{\text{IR},H}$ . The search statistic is taken as the fraction of sources for

which either  $d_{\text{IR},J}$  or  $d_{\text{IR},H}$  falls outside the 95<sup>th</sup> percentile of the  $H1$  distribution.

### B3 Radio Search for SNR Shells

The radio search uses the position, proper motion, and angular size to define association p-values, which cover two independent cases: first, that the magnetar resides within the SNR shell, and second, that the magnetar was kicked from the center of the SNR.  $H0$  in both cases is that the magnetar did not originate at the center of the SNR.  $p_1$  is derived similarly to the IR case; when the angular size of the SNR is known, we assume the semi-major ( $a_{\text{SNR}}/2$ ) and semi-minor axes ( $b_{\text{SNR}}/2$ ) are the  $3\sigma$  half-widths of the error ellipse. If not, the error ellipse is used to derive the binormal distribution. We again derive the search statistic  $\hat{g}_1$  using the 95<sup>th</sup> percentile contour, and the p-value  $p_1$  by comparing to the  $H0$  distribution of  $\hat{g}_1$ , which is derived using mean angular separations between  $1 - 5\sigma_{\alpha/\delta}$  of the origin.

The second criteria is similar to that above, but instead compares the angle of the line connecting the magnetar location and the SNR,  $\rho_{\text{SNR}} = \tan^{-1}(\Delta\delta/\Delta\alpha)$ , and the direction of the magnetar's proper motion,  $\rho_{\text{mag}} = \tan^{-1}(\mu_{\delta}/(\mu_{\alpha}\cos(\delta)))$ . The  $H0$  distribution of  $\hat{g}_2$  is computed using mean angular differences  $\Delta\rho = |\rho_{\text{SNR}} - \rho_{\text{mag}}|$  between the 95<sup>th</sup> percentile of the observed distribution and  $180^\circ$ .  $p_3$  uses the magnetar proper motion and the median magnetic field decay age  $\mathcal{T}_{\text{decay}}$  computed from the X-ray luminosity (see Appendix D1 and Ferrario & Wickramasinghe 2008) to derive samples of the expected angular separation between magnetar and SNR,  $\Delta\theta_{\text{mag}} = |\vec{\mu}|/\mathcal{T}_{\text{decay}}$ . If the magnetar has no X-ray luminosity or magnetic field estimate, the spin-down age  $\mathcal{T}_{\text{rot}}$  from the McGill magnetar catalog is used instead. Samples of the true angular separation,  $\Delta\theta_{\text{SNR}}$  are derived using samples of the RA and declination of the magnetar and SNR. The search statistic  $\hat{g}_2$  is the fraction of samples for which the difference in angular separation,  $\Delta(\Delta\theta) = |\Delta\theta_{\text{SNR}} - \Delta\theta_{\text{mag}}|$  is outside the 95<sup>th</sup> percentile from the  $H1$  case.  $p_3$  is then derived from the  $H0$  distribution of  $\hat{g}_3$ , which assumes mean angular separations between the 95<sup>th</sup> percentile and  $1'$ .

Finally, we estimate  $p_4$  based on the angular size  $\Delta\theta$  of the SNR; we impose a lower limit on the angular size required to be associated with the magnetar given the magnetar's distance and age  $\mathcal{T}_{\text{decay/rot}}$ . By sampling the magnetar distance  $d$  we compute samples of the physical radius of the SNR as  $r_{\text{SNR}} = d_{\text{mag}}\Delta\theta$  and estimate the corresponding dynamical age  $\mathcal{T}_{\text{dyn}}$  from either free-expansion or Sedov-Taylor phase expansion as described in Appendix D2 (Sedov 2018). For this we also sample the progenitor envelope mass from a uniform distribution between  $2.75 - 120M_{\odot}$ <sup>47</sup> and use an explosion energy  $10^{51}$  ergs<sup>48</sup> (Morozova et al. 2017). We then draw samples of the magnetar age  $\mathcal{T}_{\text{decay/rot}}$  and compute the statistic  $\hat{g}_3$  as the fraction of samples for which  $\mathcal{T}_{\text{decay/rot}} > \mathcal{T}_{\text{dyn}}$ . We impose only a loose lower limit since magnetar spindown and decay ages are uncertain. The p-value  $p_3$  is taken as the percentile of  $\hat{g}_3$  within the  $H0$  distribution which assumes mean ages between  $\mathcal{T}_{\text{dyn}}$  and the 95<sup>th</sup>

percentile of the  $H1$  distribution.  $p_1$ ,  $p_2$ , and  $p_3$  are combined using Equations 5 and 6.

#### B3.1 'By-Eye' Identification and Fitting of Candidates

Optical, infrared, and radio sources identified 'by eye' which do not have known counterparts in public catalogs considered here were fit with ellipses parameterized by the RA and declination of the center ( $\alpha_c, \delta_c$ ), major and minor axes ( $a, b$ ), and position angle measured North of East ( $\chi$ ). Shifting the center of the ellipse to 0, the fit equation for the radius  $r$  as a function of polar angle  $\theta$  is given by:

$$r(\theta) = ab((b^2\cos^2(\chi) + a^2\sin^2(\chi))\cos^2(\theta) + (b^2\sin^2(\chi) + a^2\cos^2(\chi))\sin^2(\theta) + 2(b^2 - a^2)\cos(\chi)\sin(\chi)\cos(\theta)\sin(\theta))^{-1/2} \quad (\text{B5})$$

For each source, the contour at one-half the maximum value within one arcminute (for radio sources; one arcsecond for optical and IR sources) of the identified center. The mean  $\alpha$  and  $\delta$  were recomputed from this contour prior to fitting with an ellipse using the equation above. The major and minor axes and position angle were then used identically to those of SNRs for the association test (see Section B3). Note that apparent magnitudes were not estimated for these sources, and p-values could not be estimated for the optical and IR searches. Any point sources of interest were queried in SIMBAD and public catalogs to determine the likelihood of association.

### B4 Gaia Search for Unbound Companions

Criteria for association of unbound *Gaia* sources with magnetars is based on their current positions, proper motion magnitudes and directions, and the consistency of the magnetar travel time with age estimates.  $H0$  is that the magnetar and source positions are not consistent with having an origin at the same location. For  $p_1$ , we assume the *Gaia* DR3 proper motion, parallaxes, and positions are Gaussian (or 2-sided Gaussian, where applicable) distributed, with standard deviation equal to the uncertainty. To account for bias in the conversion from parallax to distance ( $d \approx \omega^{-1}$ ) we adopt the photo-geometric distance from the Bailer-Jones (2023) catalog.

For each magnetar, samples of the distance  $d$ , RA ( $\alpha$ ) and declination ( $\delta$ ) are drawn from their respective distributions to get samples of the position vector,  $\vec{r}_{\text{mag},i}$  (the subscript  $i$  indicates the quantity is Monte Carlo sampled). Magnetar proper motion measurements are often unavailable due to their reliance on Very Long Baseline Interferometry (VLBI) (e.g Tendulkar et al. 2012). In such cases, we draw samples of the magnetar velocity magnitude from a Maxwellian distribution with scale parameter  $\sigma = 265 \text{ km s}^{-1}$  as described in Hobbs et al. (2005). The velocity direction is drawn from a 3D uniform distribution to obtain  $\vec{v}_{\text{mag},i}$ . If proper motions are known, the total velocity is still drawn from the truncated Hobbs et al. (2005) distribution, and the radial velocities are then computed from the velocity and proper motion samples with the sign chosen from a uniform distribution. Samples of the age  $\tau_i$ , defined here as the time since the magnetar supernova would have occurred, are drawn from a uniform distribution from  $1 - 10$  kyr. A sub-sample of *Gaia* sources within  $5^\circ$  of the magnetar-under-test are selected from the full sample to test for association. In a similar method to that above, samples of position  $\vec{r}_i$  and velocity  $\vec{v}_i$  are drawn for each *Gaia* source; here we sample the empirical walk/runaway velocity distribution from the fiducial simulation of Renzo et al. (2019) for which  $\sim 95\%$  of simulated ejected massive stars have velocities  $\lesssim 30 \text{ km s}^{-1}$  (see also Blaauw

<sup>47</sup> This range implicitly assumes that mass transfer to a binary companion or lost to stellar winds are negligible, which is not necessarily the case (Nomoto et al. 1995; Thielemann et al. 1996).

<sup>48</sup> Nomoto et al. (1995) suggest that gravitational binding energy  $\sim 10^{53}$  ergs can increase the energy of supernovae. However, we use the observational constraint of  $\sim 10^{51}$  erg from Type II CCSN lightcurves from (Morozova et al. 2017). Since Type II supernovae make up  $\sim 90\%$  of CCSNe, we find this assumption justified.

1961; Tetzlaff et al. 2010; Sayers et al. 1996; Feast & Shuttlesworth 1965).

Next, the magnetar and source trajectories are traced for each sample from their current positions  $\vec{r}_{\text{mag},i}$  and  $\vec{r}_i$  to their locations at time  $\tau_i$  in the past:

$$\vec{r}_{o,\text{mag},i} = \vec{r}_{\text{mag},i} - \tau_i \vec{v}_{\text{mag},i} \quad (\text{B6})$$

$$\vec{r}_{o,i} = \vec{r}_i - \tau_i \vec{v}_i \quad (\text{B7})$$

We have utilized the *astropy* library's *apply\_space\_coord* method to perform this propagation, and use the *astropy.SkyCoord* object for conversion between Cartesian and Spherical coordinate systems. The initial RA and declination of source and magnetar,  $\alpha_{o,i}, \delta_{o,i}$  and  $\alpha_{o,\text{mag},i}, \delta_{o,\text{mag},i}$ , are derived from  $\vec{r}_{o,i}$  and  $\vec{r}_{o,\text{mag},i}$ , and are used to compute the angular separation at the time of the supernova,  $\Theta_i$ . We compute this using *SkyCoord.angular\_separation* method, which implements the Vincenty formula for the Great-circle distance between two points on a spherical surface (Vincenty 1975). Additionally, using the G-band magnitude for each source, the  $G - V$  color derived through Johnson-Cousins relations, and the distance samples which are converted to distance moduli, we also derive samples of the V-band absolute magnitude  $M_{V,i}$ :

$$M_{V,i} = (m_G - A_G - (5 \log_{10}(d_i) - 5)) - (G - V) \quad (\text{B8})$$

$\Theta_i$  and  $M_{V,i}$  are used as the parameters of interest and compared to a threshold contour in  $\{\Theta, M_V\}$  space. The contour is computed by injecting 100 positively-associated simulated sources with an OB-star-like absolute magnitude,  $-10 \leq M_V \leq +3$ . The 90<sup>th</sup> percentile contour of the 2D histogram is used as a threshold, and we define the search statistic  $\hat{f}$  as the fraction of Monte Carlo samples falling outside the contour. A separate threshold contour is determined for each magnetar, using the position, distance, and proper motion of the magnetar as available. Critical values  $\hat{f}_c$  were derived through a Receiver Operating Characteristic (ROC) analysis for each magnetar, which is summarized in Appendix B4.1. By comparing the final  $\hat{f}$  to samples in the  $H1$  hypothesis (obtained during the ROC test), we estimate a p-value,  $p_1$ , as the percentile of  $\hat{f}$  within the  $H1$  sample.

To further narrow down the candidate *Gaia* sources with  $\hat{f} < \hat{f}_c$ , we iteratively compute the true intersection points  $\vec{r}_{\otimes,i}$  of the sampled trajectories with those of the magnetars, eliminating any samples with non-physical solutions. We then use the Monte Carlo sampled proper motions and positions to estimate the 2-dimensional travel times for each magnetar-candidate pair:

$$\tau_{2D,i} \approx \frac{\Delta\Phi_{\otimes,i}}{\sqrt{\mu_{\alpha,i}^2 \cos^2(\delta_i) + \mu_{\delta,i}^2}} \quad (\text{B9})$$

$$\tau_{2D,\text{mag},i} \approx \frac{\Delta\Phi_{\otimes,\text{mag},i}}{\sqrt{\mu_{\alpha,\text{mag},i}^2 \cos^2(\delta_{\text{mag},i}) + \mu_{\delta,\text{mag},i}^2}} \quad (\text{B10})$$

where  $\Delta\Phi_{\otimes}$  is the angular separation between the intersection point and the current coordinate. Since we expect  $\tau_{2D,\text{mag},i} = \tau_{2D,i}$ , we estimate a  $\chi^2$  statistic comparing the  $\tau_{2D,\text{mag},i}$  vs.  $\tau_{2D,i}$  curve to a line with slope 1, taking the p-value  $p_2$  as another measure of association. Similarly, we compute the physical travel time for the magnetar assuming it is at the *Gaia* source distance:

$$\mathcal{T}_{3D,\text{mag},i} \approx \frac{|\vec{r}_{\text{mag},i} - \vec{r}_{\otimes,i}|}{|\vec{v}_{\text{mag},i}|} \quad (\text{B11})$$

We expect each magnetar's travel time to be less than its age; if an SNR candidate with an age measurement is confidently associated with the magnetar, we use the SNR age,  $\mathcal{T}_{\text{SNR}}$ . Five magnetars in our sample have  $\mathcal{T}_{\text{SNR}}$  estimates, four of which are measured assuming Sedov-Taylor plasma dynamics and the other which is computed kinematically using the magnetar proper motion (Sedov 2018; Dohm-Palmer & Jones 1996; Anderson et al. 2012b; Blumer et al. 2019; Borkowski & Reynolds 2017; Lyman et al. 2022; Gaensler et al. 1999a). If no SNR association is known or its age is unconstrained, we estimate the age  $\mathcal{T}_{\text{decay}}$  from continuum X-ray luminosity measurements using the crustal field decay model (see Ferrario & Wickramasinghe 2008, and Appendix D1). This applies to 18 magnetars in our sample. If no SNR association is known and the X-ray luminosity or surface magnetic field strength are unknown, the spin-down age  $\mathcal{T}_{\text{rot}}$  reported in the McGill magnetar catalog is used in its place (Olausen & Kaspi 2014). 5 magnetars in the sample require spin-down ages to be used, decreasing confidence in their p-values since  $\mathcal{T}_{\text{rot}}$  is predicted to over-estimate magnetar ages (e.g. Kaspi & Beloborodov 2017). For 5 magnetars, none of the three age estimates are known, and the final p-value is computed from  $p_1$  and  $p_2$  alone.

For  $p_4$ , we use samples of the magnetar and source distances from the initial Monte Carlo search to estimate the distribution of the difference,  $\Delta d_i = d_i - d_{\text{mag},i}$ . The width of this distribution is dominated by the magnetar's distance error. We estimate the  $H1$  distribution, for which the magnetar and source are at the same distance, by shifting the  $\Delta d$  samples to have median 0. We then compute the search statistic as the fraction of  $\Delta d$  samples within the  $3\sigma$  width (0.15 – 99.85<sup>th</sup> percentiles) of the  $H1$  distribution. We compare this to 100 realizations of the  $H0$  distribution which are shifted to have medians between  $1 - 6\sigma_d$ , where  $\sigma_d$  is the width of the  $H1$  distribution, and compute the search statistic for each trial. The p-value  $p_4$  is computed as the percentile of the observed  $\Delta d$  statistic among the  $H0$  distribution of statistics.

#### B4.1 Receiver Operating Characteristic Analysis

The optimal critical threshold for the *Gaia* Monte Carlo search,  $\hat{f}_c$ , was derived through an ROC analysis. To compute the true positive rate (TPR) for trial thresholds from 0.1 to 1, 10000 injection sources were simulated with randomly chosen ages between 1-10 kyr and velocity drawn from the fiducial simulation described in Renzo et al. (2019). A test magnetar was simulated with velocity drawn from the Hobbs et al. (2005), and both magnetar and source were propagated to present-day positions, starting from the same start position ( $P_0 = P_{0,\text{mag}}$ ). Each simulated source was given an OB-star-like absolute magnitude  $M_V = -1.5$ . The Monte Carlo search was conducted with 1000 trials for each simulated source and the simulated magnetar. Search statistics  $\hat{f}$  were computed for each source. The TPR for each trial  $\hat{f}_c$  was computed as the fraction of sources with  $\hat{f} < \hat{f}_c$ . The false negative rate (FNR) is computed as  $\text{FNR} = 1 - \text{TPR}$ .

To compute the false positive rate (FPR) for a given magnetar location, we tile the region nearby with  $10'$  pointings, starting at  $10'$  from the magnetar. For each tile, we pass all sources through the Monte Carlo association test, using the tile's center as the coordinates of the 'fake' magnetar. Since no magnetar is in the query region, these test samples are used as true negative injections. The FPR for each trial  $\hat{f}_c$  was computed as the fraction of total sources (from all tiles) with  $\hat{f} < \hat{f}_c$ .

**Table B1.** Critical Thresholds for Magnetar Association Tests

Magnetar	$\hat{f}_c$
CXOU J010	72.4%
4U 0142	5.7%
SGR 0418	87.2%
SGR 0501	91.2%
SGR 0526	80.4%
1E 1048	94.4%
1E 1547	3.4%
PSR J1622	98.5%
SGR 1627	11.4%
CXOU J1647	93.4%
IRXS J1708	99.2%
CXOU J1714	96.4%
SGR J1745	20.4%
SGR 1806	2.8%
XTEJ1810	74.5%
Swift 1818	36.3%
SGR J1822	83.3%
SGR 1833	90.0%
Swift J1834	54.4%
1E 1841	14.3%
3XMMJ1852	89.3%
SGR 1900	40.3%
SGR 1935	12.4%
1E 2259	54.5%
<hr/>	
SGR 0755	63.7%
SGR 1801	11.2%
SGR 1808	64.4%
AX J1818	92.3%
AX J1845	91.0%
SGR 2013	84.3%
PSR J1846	7.4%

We expect differences in each magnetar’s local environment, both in source density and, potentially, stellar types. Therefore, the ROC analysis is carried out for each magnetar individually. Note that in most cases, the FPR is very low; the FPR is higher for SGR 1801-23 because of its lack of distance measure and large position error. We choose the threshold for each magnetar where the TPR is maximized and the FPR is minimized; in cases where the FPR is consistently 0%, the threshold is  $\hat{f}_c = 100\%$ . In these cases, a *Gaia* source is a candidate for association if any Monte Carlo sample falls within the 90<sup>th</sup> percentile contour in  $\{\Theta, M_V\}$  space. Similarly, in cases where the FNR is consistently 0% (which occurs when the proper motion, position, and distance are well-constrained), the threshold is  $\hat{f}_c = 0\%$ . In these cases, a *Gaia* source is a candidate for association only if all Monte Carlo samples fall within the 90<sup>th</sup> percentile contour in  $\{\Theta, M_V\}$  space. Overall, we find this has little effect on the results, as most *Gaia* sources have either all or none of their samples within the contour region. We list  $\hat{f}_c$  for each magnetar in Table B1.

## APPENDIX C: FALSE POSITIVE ANALYSES

### C1 *Gaia* Search False Positives

In this section we discuss in detail the reasons that the candidates for unbound stellar companions of 3XMM J185246.6+003317 were rejected as false positives.

#### C1.1 3XMM J185246.6+003317

For 3XMM J185246.6+003317, four candidates, *Gaia* DR3 4266311617807818624 (Source 1), *Gaia* DR3 4266313683745630080 (Source 2), *Gaia* DR3 42663155048110807488 (Source 3), and *Gaia* DR3 4258978601120897664 (Source 4), are identified with  $p < 5\%$ , all requiring the magnetar to have proper motion  $\mu_\alpha \cos(\delta) \sim -5$  and  $\mu_\delta \sim -3.5 \text{ mas yr}^{-1}$ . For Sources 1 and 2, the stellar velocities are consistent with walkaway stars with  $|\vec{v}| \approx 28_{-5}^{+8} \text{ km s}^{-1}$  for Source 1 and  $|\vec{v}| \approx 30_{-5}^{+8} \text{ km s}^{-1}$  for Source 2; the travel times are consistent with the magnetar’s at the  $1\sigma$  and  $2\sigma$  levels, respectively. Higher velocities more consistent with runaway stars are required for Sources 3 and 4:  $|\vec{v}| \approx 68_{-15}^{+10} \text{ km s}^{-1}$  and  $|\vec{v}| \approx 143_{-10}^{+6} \text{ km s}^{-1}$ , respectively. Without uncertainties on the distance of 3XMM J185246.6+003317, it is difficult to evaluate if each source is consistent with the magnetar’s distance. However, the magnetar’s estimated distance  $\sim 7.1 \text{ kpc}$  far exceeds the four Sources’ parallax distances, which are between 1 – 3 kpc. 3XMM J185246.6+003317’s distance was estimated from the nearby SNR Kes 79 based on their similar hydrogen column densities  $N_H \approx 1.5 \times 10^{22} \text{ cm}^{-2}$  (Zhou et al. 2014). This is questionable given that Kes 79 is confirmed in association with a separate X-ray pulsar, CXOU 185238.6+004020 (Seward et al. 2003), although we explore a scenario in which both the pulsar and magnetar may be associated with the SNR in Section 3. It is also known that some X-ray sources have significant local extinction that can bias the foreground  $N_H$  estimate (e.g. Chaty & Rahoui 2012; Predehl & Schmitt 1995). However, the lack of notable IR emission from 3XMM J185246.6+003317 distinguish it from sources with significant local  $N_H$  such as HMXBs. Therefore, it is likely that  $N_H$  is indeed from the foreground and its similarity to that of Kes 79 suggest they are at the same distance  $\sim 7.1 \text{ kpc}$ . If this is the case, then all five sources are in the foreground and cannot be associated with 3XMM J185246.6+003317. A precise proper motion measurement and independent distance measurement would allow more confident conclusions to be drawn.

### C2 Radio SNR Search False Positives

In this section we justify why candidates for SNR association with SGR 0755-2933 were rejected as false positives.

#### C2.1 SGR 0755-2933

Eight radio sources were identified with  $p < 5\%$  as potential SNRs associated with SGR 0755-2933 Richardson et al. (2023) and Doroshenko et al. (2021) (see also Surnis et al. 2016; Archibald et al. 2013; Barthelmy et al. 2016). VLASS image cutouts with  $1''$  pixels were obtained for each candidate, and four are ruled out as point sources. Two other sources are found to be coincident with known stellar objects within  $1'$  (an eclipsing binary and a Carbon star). The remaining two sources are each  $\sim 14''$  across, or  $\sim 0.22 \text{ pc}$  at SGR 0755-2933’s distance of  $3.5 \pm 2 \text{ kpc}$ . Assuming the free-expansion phase, this corresponds to an SNR age range of 80 – 300 years, which is marginally consistent with magnetar ages in general. If we accept the Doroshenko et al. (2021) association of SGR 0755-2933 with the X-ray source 2SXPS J075542.5-293353, we can use the X-ray luminosity  $L_X \approx 10^{34} \text{ erg s}^{-1}$  to estimate  $\mathcal{T}_{\text{decay}}$  for a typical magnetic field strength  $B \sim 10^{14} \text{ G}$  (see Appendix D1). From this method we estimate  $\mathcal{T}_{\text{decay}} \approx 60 \text{ kyr}$  which

is much larger than the free-expansion ages for the two SNR candidates. The detection of a subsequent burst resulting in more precise localization could confidently rule out one source which lies outside the  $3\sigma$  error region of SGR 0755-2933. With the information at hand, we conclude that both sources are likely to be false positives based on the large position uncertainty and decay age estimate.

### C3 Bound Companion Search False Positives

In this section we justify why the bound companion candidates for PSR J1622-4950 and SGR J1822.3-1606 were rejected as false positives.

#### C3.1 PSR J1622-4950

Through the optical search, the SkyMapper source SMSS J162244.99-495055.7 was recovered with p-value  $p = 1\%$  as a potential bound companion of PSR J1622-4950. This magnetar lies along a highly extinguished sightline, with  $A_V \approx 30.17^{+8.94}_{-7.82}$  from the [Predehl & Schmitt \(1995\)](#)  $N_H - A_V$  relation. From the  $g$ - and  $r$ -band apparent magnitudes, we therefore estimate an absolute magnitude  $M_V \sim -23.4$ , which would be extremely bright for an OB star. From the mass-luminosity relation, this would correspond to a  $\sim 10^{13} M_\odot$  star, which is unphysical. We also note that the candidate has a large angular separation  $\sim 3.31''$ , corresponding to 0.14 pc at the magnetar's  $9 \pm 1.35$  kpc distance. This is impractical for the orbit of a neutron star ( $\sim 1.4 M_\odot$ ) and massive star ( $\lesssim 120 M_\odot$ ), suggesting an orbital period of  $\sim 10^{18}$  years. Therefore, we conclude that this source is most likely a false positive. [Chrimes et al. \(2022a\)](#) identify a potential infrared counterpart for PSR J1622-4950 using HST data, but this is not recovered in either the optical or IR search in this work. This is consistent with their claim in [Chrimes et al. \(2022b\)](#) that this is more likely to be surface emission from the neutron star than a companion star.

#### C3.2 SGR J1822.3-1606

Two IR sources nearby SGR J1822.3-1606 are found to have  $p < 0.1\%$ : 2MASS 18221839-1604241 and 2MASS 18221794-1604259, though the optical counterparts from the PS1 catalog are not recovered (see Figure 3). The former is unlikely based on its angular separation  $\sim 6.7'' \pm 0.7''$ ; at the magnetar's distance  $1.6 \pm 0.3$  kpc, this corresponds to  $\sim 0.05$  pc which is too large for a bound orbit. While this could be an unbound companion, it was not recovered in the *Gaia* search, and the absolute  $J - H$  color is inconsistent with OB stars at the  $5\sigma$  level when placed at the magnetar distance, with  $J - H \approx 0.85 \pm 0.10$  ([Chrimes et al. 2022b](#)). We conclude this is a false positive for a bound companion.

The second source, 2MASS 18221794-1604259, is much closer to the magnetar at  $\sim 0.01'' \pm 0.7''$ , or  $\sim 20$  au at the magnetar's distance  $\sim 1.6 \pm 0.3$  kpc, though this is still too distant for a bound system. This source was similarly identified as evidence that SGR J1822.3-1606 may be a Be star X-ray binary, like SGR 0755-2933, when initially discovered by e.g. [Halpern \(2011\)](#), [Gogus & Gorosabel \(2011\)](#), [Gorosabel et al. \(2011\)](#). The source's *Gaia* counterpart, *Gaia* DR3 4097826476059022848, has a negative parallax  $\omega = -1.2 \pm 0.6$  mas which excluded it from the *Gaia* search (see Section 3 and Appendix A). Its parallax distance is  $d \approx 7.0^{+3.1}_{-2.8}$  kpc, which agrees with the magnetar's distance within  $1\sigma$ . At the magnetar's distance, the intrinsic magnitude and color are  $M_H \approx 2.5 \pm 0.1$  and  $J - H \approx 1.5 \pm 0.1$ , which are stellar in nature. However, the

color is redder than expected for OB stars, and is more characteristic of an evolved supergiant star ([Chrimes et al. 2022b](#)). Notably, the star's proper motion from *Gaia* is  $\mu_\alpha \cos(\delta) = -5.6 \pm 0.7$  mas yr $^{-1}$ ,  $\mu_\delta = -8.2 \pm 0.6$  mas yr. Applying the *Gaia* Monte Carlo test results in a p-value  $p = 79\%$  due to the significant travel time difference  $\Delta\tau_{2D} \approx 0.3^{+0.7}_{-0.2}$  kyr required to trace trajectories to a common origin. While a magnetar proper motion measurement would motivate re-analysis, we conclude that the close proximity and companion's significant proper motion make it unlikely that the candidate is associated with SGR 1822.3-1606.

## APPENDIX D: MAGNETAR AGE ESTIMATION

Magnetars' magnetic field decay and irregular outbursting and 'glitching' behavior make their characteristic spindown ages  $\mathcal{T}_{\text{rot}} = P(2\dot{P})^{-1}$  overestimates of their true age ([Nakano et al. 2015](#); [Kaspi & Beloborodov 2017](#); [Olausen & Kaspi 2014](#); [Ferrario & Wickramasinghe 2008](#)). In this section we provide a brief overview of two alternative estimates based on the X-ray luminosity and the dynamical plasma age of an associated SNR.

### D1 Derivation of Magnetar Age X-ray Luminosity Decay

We define  $\mathcal{T}_{\text{decay}}$  as the age of the magnetar estimated from the decaying crustal X-ray luminosity,  $L_X$ . This model is described in detail in [Ferrario & Wickramasinghe \(2008\)](#) and [Ferrario & Wickramasinghe \(2006\)](#) based on [Pons & Geppert \(2007\)](#). In this model, the dipole magnetic field component is responsible for spindown energy loss, but does not decay on timescales below  $\sim 100$  Myr. The toroidal component decay on timescales  $\sim 1 - 10$  kyr drives energy loss through quiescent crustal X-ray emission  $L_X$ . We assume the luminosity is modelled by an exponential decay following the initial cooling phase:

$$L_X(t) = L_0 \left( \frac{B_d}{10^{13} \text{ G}} \right) e^{-t/\tau_d} \quad (\text{D1})$$

where  $B_d$  is the dipole field strength,  $L_0 = 10^{33}$  erg s $^{-1}$ , and  $\tau_d$  is the decay timescale. The decay timescale is inversely proportional to the magnetic field, and is modelled as a power law dependence with  $\delta = 1.3$ :

$$\tau_d = \tau_{d0} \left( \frac{B_d}{10^{13} \text{ G}} \right)^{-\delta} \quad (\text{D2})$$

where  $\tau_{d0} = 500$  kyr. Plugging this into Equation D2 and solving for  $t = \mathcal{T}_{\text{decay}}$ , which we take to be the present-day:

$$\mathcal{T}_{\text{decay}} = \tau_{d0} \left( \frac{B_d}{10^{13} \text{ G}} \right)^{-\delta} \ln \left( \frac{L_X(t = \mathcal{T}_{\text{decay}}) 10^{13} \text{ G}}{L_0 B_d} \right) \quad (\text{D3})$$

where  $L_X(\mathcal{T}_{\text{decay}})$  is the X-ray luminosity at present-day. The constants  $L_0$ ,  $\tau_{d0}$ , and  $\delta$  were determined through simulations by [Ferrario & Wickramasinghe \(2008\)](#). Figure D1 shows each magnetar's  $\mathcal{T}_{\text{decay}}$  as a function of  $L_X$  and  $B_d$ .



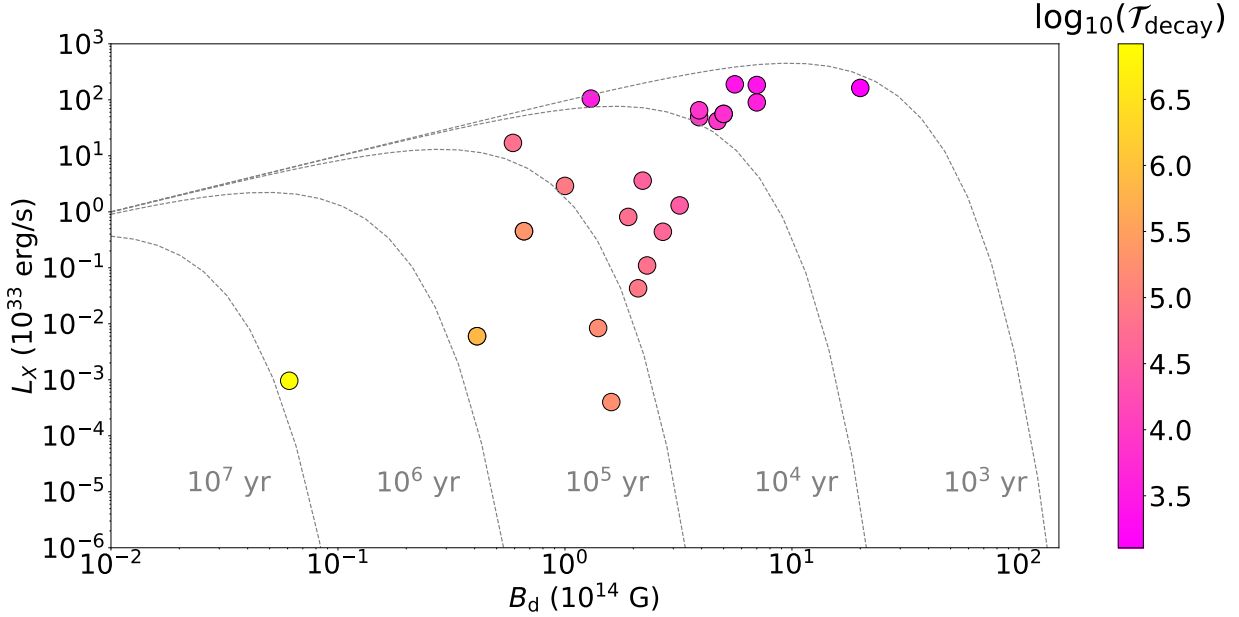


**Figure D1.** X-ray Luminosity ( $L_X$ ) vs. Dipole Magnetic Field Strength ( $B_d$ ) for Known Magnetars using the Decay Model of Ferrario & Wickramasinghe (2006, 2008). The magnetic field estimate is derived from the pulse period  $P$  and spindown rate  $\dot{P}$  using  $B_d \approx (3.2 \times 10^{19} G) \sqrt{P \dot{P}/1 \text{ s}}$  as reported in the McGill catalog (Olausen & Kaspi 2014). The X-ray luminosity is derived from the 2 – 10 keV flux and reported distance, also from the McGill catalog. The colorbar corresponds to the decay age  $\mathcal{T}_{\text{decay}}$  derived from Equation D3, and lines of constant age are shown in grey. This estimate is preferred to the spindown age,  $\mathcal{T}_{\text{tot}}$ , which likely overestimates magnetar ages through neglect of field decay and glitching (e.g. Nakano et al. 2015; Kaspi & Beloborodov 2017).

## D2 Derivation of Free-Expansion and Sedov-Taylor Expansion SNR Ages

In this section, we provide a brief description of the free-expansion and Sedov-Taylor expansion phases for SNRs as are relevant to this paper. We do not offer a detailed derivation, but refer the reader to Sedov (2018, Chapters IV. and V.), Truelove & McKee (1999), and Suzuki et al. (2021) from which this section is summarized. See also Taylor (1950) and Sedov (1946) for additional details. In this work, we are concerned with the age-radius relations for SNRs, and focus the discussion on this.

The earliest stage of a supernova explosion, which we refer to as ‘free expansion’, is dominated by the momentum of the ejecta mass,  $M_{\text{ej}}$ , rather than mass swept up from the surrounding medium (Truelove & McKee 1999). This, coupled with the negligible radiative energy losses during this phase, allow the ejecta from the supernova to expand freely into the surrounding medium. During this phase, the radius of the expanding ejecta front is approximately linear with time:

$$\frac{R_{\text{FE}}}{1 \text{ km}} \approx (7090 \text{ km/s}) \sqrt{\frac{E}{10^{51} \text{ ergs}} \frac{M_{\odot}}{M} \frac{\mathcal{T}}{1 \text{ s}}} \quad (\text{D4})$$

where  $E$  is the energy of the supernova and  $\mathcal{T}$  is the age of the remnant. The expansion velocity is lower than the sound speed in the surrounding medium, causing a ‘blast wave’ shock to precede the ejecta shell and inducing a reverse shock to oppose the ejecta. This marks the start of the transition to the Sedov-Taylor expansion phase, and occurs roughly on the characteristic timescale:

$$\mathcal{T}_{\text{ch}} = \frac{M^{5/6}}{E^{1/2} (\mu n_{e,0})^{1/3}} \quad (\text{D5})$$

where  $\mu \approx 1.4 m_p$  is the reduced mass of the ejecta and  $n_{e,0}$  is the initial electron density, which increases with time through interaction with the ambient medium. The corresponding characteristic radius is

$$R_{\text{ch}} = \left( \frac{M}{\mu n_{e,0}} \right)^{1/3} \quad (\text{D6})$$

(Truelove & McKee 1999; Sedov 2018).

Beyond this timescale and radius, the system enters the Sedov-Taylor expansion phase, in which the expansion is damped by the ambient medium. On late timescales, the ejecta expands as a power law with  $R \propto \mathcal{T}^{2/5}$ . To first order, we can form a piecewise model of  $R(\mathcal{T})$  by joining the free expansion and Sedov-Taylor solutions at  $R_{\text{ch}}(\mathcal{T}_{\text{ch}})$ . Imposing this condition, we can derive the coefficient for the Sedov-Taylor solution:

$$\begin{aligned} \frac{R_{\text{ST}}}{1 \text{ km}} &\approx \left( \frac{R_{\text{ch}}}{1 \text{ km}} \right) \left( \frac{\mathcal{T}}{1 \text{ s}} \right)^{-2/5} \\ &= (7090 \text{ km/s}) \sqrt{\frac{E}{10^{51} \text{ ergs}} \frac{M_{\odot}}{M}} \left( \frac{\mathcal{T}_{\text{ch}}}{1 \text{ s}} \right)^{-3/5} \left( \frac{\mathcal{T}}{1 \text{ s}} \right)^{-2/5} \end{aligned} \quad (\text{D7})$$

which we note is independent of mass (Truelove & McKee 1999; Sedov 2018). We use this age estimate as an upper limit on the required age of a candidate SNR when deriving  $p_3$  in the radio SNR

search (see Section B3) and when considering the associations of SNRs in Section 5.3. We do not use this approximation for the SNR age estimates in Table 2, and opt only to use  $T_{\text{SNR}}$  for those with age estimates in the literature.

#### APPENDIX E: PAST SNR AND NEUTRON STAR COMPANION SEARCH THRESHOLDS

Here we list references for the previous surveys used for comparison in Figure 6. For past radio SNR searches (see Green 2019), we include the Canadian Galactic Plane Survey (CGPS; Gerbrandt et al. 2014; Reich et al. 1990; Kothes et al. 2006, *bottom*), the Parkes Galactic Plane Survey (PGPS; Duncan et al. 1997, *bottom left*), the Parkes-MIT-National Radio Astronomy Observatory (PMN; Stupar et al. 2007; Condon et al. 1993, *bottom left*), the 20 cm VLA supernova remnant search (VLA92; Sramek et al. 1992, *bottom middle*), the Multi-Array Galactic Plane Imaging Survey (MAGPIS; Helfand et al. 2006, *bottom middle*), The HI, OH, Recombination line (THOR) and VLA Galactic Plane Survey (VGPS) combined survey (THOR+VGPS; Bihr et al. 2016; Anderson et al. 2017, *bottom middle*), and the Molonglo Observatory Synthesis Telescope (MOST) Galactic Plane survey (MGPS; Whiteoak & Green 1996, *bottom right*). We include limits from the Naval Observatory Merged Astrometric Dataset (NOMAD; Zacharias et al. 2004, 2005) and Tycho-2 (Høg et al. 2000b) point source and proper motion catalogs (*middle*), the former of which Kochanek (2018) use to search for stellar companions of the Crab and Cas A pulsars. We also include limits from the Asteroid Terrestrial-impact Last Alert System (ATLAS) Photometric All-Sky Survey (APASS; ) and the HST used by Kochanek (2021) (in conjunction with 2MASS, UKIDSS, PS1, and *Gaia*) and Chrimes et al. (2022b), respectively, to search for pulsar and magnetar companions.

This paper has been typeset from a  $\text{\TeX}/\text{\LaTeX}$  file prepared by the author.